Piezoelectric Energy Harvesting for Public Roadways

by

Haocheng Xiong

Dissertation submitted to the faculty of the

Virginia Polytechnic Institute and State University

in partial fulfillment of the requirements for the degree of

Doctor of Philosophy

in

Civil Engineering

Wang, Linbing, Chair

Abbas, Montasir

Druta, Cristian

Priya, Shashank

December 3rd, 2014

Blacksburg, VA

Keywords: Piezoelectricity, Energy Harvesting, Smart Transportation Infrastructure, Pavement, PZT

Abstract

Energy harvesting technologies have drawn much attention as an alternative power source of roadway accessories in different scales. Piezoelectric energy harvesting consisting of PZT piezoceramic disks sealed in a protective package is developed in this work to harness the deformation energy of pavement induced by traveling vehicles and generate electrical energy. Six energy harvesters are fabricated and installed at the weigh station on I-81 at Troutville, VA to perform on-site evaluation. The electrical performance of the installed harvesters is evaluated by measuring the output voltage and current generated under real traffic. Instant and average power outputs are calculated from the measured waveforms of output voltage and current. The analysis of the testing results shows that the electrical productivity of the energy harvesters are highly relevant to the axle configuration and magnitude of passing vehicles. The energy transmission efficiency of the energy harvester is also assessed.

Acknowledgements

First and foremost, I would like to express my sincere appreciation to Prof. Wang, Linbing. Prof. Wang has been a great academic advisor during the days of mine pursuing my Ph.D. degree. He was always ready to discuss with me and share his spectacular view to the question. He would not directly show me the answer but enlighten me to find the right way to solve the problem. He has also provided a great environment of research with a well-organized research group and laboratory with sufficient equipment. Throughout my entire PH. D study, Prof. Wang has been more than an advisor. He has been a great mentor who was willing to give me advises on the problems from my daily life as well. He taught me how to be a great person as much as to be a great researcher. Prof. Wang has also offered me many opportunities to work on research problems different than the goal of my dissertation. These opportunities helped me on developing my own academic style. It includes many on-site engineering experiments, communications with university and government department staffs. I believe the postmasters' research of last four years under the guidance of Prof. Wang is grateful and it will be one of my most cherishing memory.

I also want to express my appreciations for funding provided by the Exploratory Advanced Research Program of FHWA, and the very many helps by engineers at Troutville weigh station and Virginia Department of Transportation (VDOT). I also gratefully acknowledge the support from Virginia Department of Motor Vehicles (VDMV) for providing the traffic data.

Table of Contents

List of Figures

List of Tables

1 Introduction

1.1 Energy Harvesting Technologies

Many researchers show great interest in the energy harvesting technology as a new source of clean energy and power supply of electronics in enclosed environment. They have proposed different energy harvesters converting ambient energy into useable electrical energy. [1, 2] Thermoelectric, electromagnetic, photovoltaic, and piezoelectric are the four energy harvesting technologies which draw most attention among the energy converting technologies. In DuToit et al.'s work, the energy productivity of these four technologies is compared in terms of power density. [11] Figure 1 illustrates a summary of the comparison. The peak productivity of photovoltaic technology is much greater than others. However, its energy productivity can be maximized only under direct sunlight during a certain time period of a day. The productivity is limited under low illumination conditions, like during a cloudy day or in a tunnel. Other than the photovoltaic technology under certain condition, piezoelectric energy harvesting is the most productive one.

When a car traveling on the pavement, part of its power supplied by burning gasoline will be transformed into deformation and vibration of the pavement. A portion of these energy will be lost in the form of heat. There are approximately 250 million vehicles registered in the United States. Piezoelectric material is able to capture the excess deformation and vibration induced by these vehicles and convert them into electrical energy. The converted electrical energy could be a power source of many transportation-related

electronic devices. The purpose of this project is to develop a piezoelectric energy harvesting system as an innovative clean power source available on public roadways.

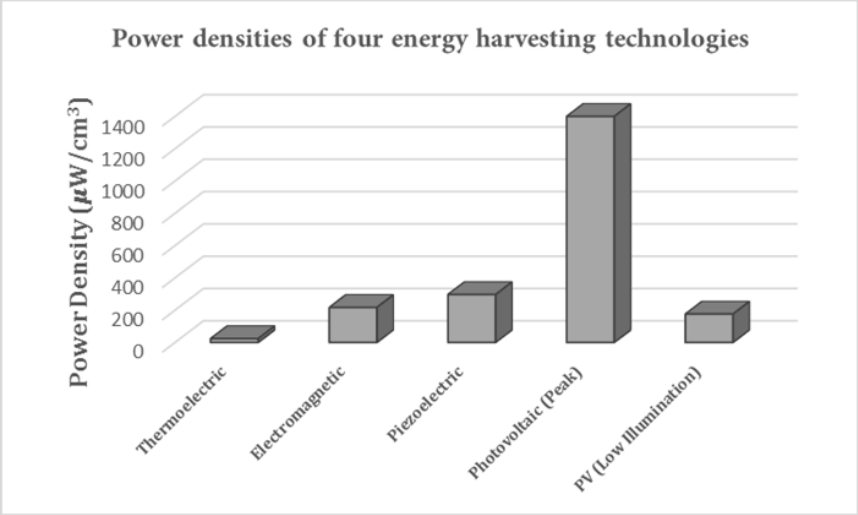

Figure 1. Chart. The comparison of the output power of four energy harvesting technologies (Voigt et al).[4]

1.2 Piezoelectric Energy Harvesting

In regular crystalline piezoelectric materials, there are many electric dipoles in it. When an electric field is applied on the piezoelectric material, the electric dipoles are aligned to a certain direction. This process is called polarization and the directions that dipoles aligned to is called poling direction. When a stress is applied to the poling direction of the piezoelectric material, the displacement of inner electric dipoles will create an electric potential on the two poles of the material. When the two poles are connected to an electric loading, the electric potential energy stored in the material is released. This phenomenon is called piezoelectricity.

Piezoelectric materials with different properties are used in different applications.[2] Piezoceramic lead zirconate titanate, or known as PZT is widely used in many designs of energy harvesters.[5] As a brittle material, PZT has low strain endurance and its application is limited. C.S. Lee et al. have developed a Poly Vinylidene Fluoride (PVDF) film in their work which is coated with poly (3, 4-ethylenedioxy-thiophene)/poly (4-styrenesulfonate) [PEDOT/PSS] electrodes.[6] With great flexibility, PVDF is capable of enduring large strains.

A number of energy harvesters utilizing piezoelectric technology have been proposed with various mechanisms of energy conversion. In the study by S. Roundy et al., the authors purposed a piezoelectric energy harvester to harvest energy from vibration.[7] Afterward, Y.B. Jeon et al. have designed an energy harvester with piezoceramic thin films mounted on a cantilever beam. 1 μW of average power has been generated from this 170 μm × 260 μm beam-shaped energy harvester. [8] The cantilever beam transfers the vertical force to the mounted thin films. The thin films are deformed transversely and the electric potential is created. Such method of energy conversion was named as 31-mode. Another method in which the piezoceramic generates electrical energy from the force applied along its direction of polarization. This method was introduced by N. E. duToit et al. in their study and it is named as 33-mode. [9] In Twiefel et al.'s study, the authors find that the productivity of a 31-mode energy harvester is maximized when the cantilever beam vibrates with its resonant frequency. However, the output drops dramatically when the vibrating frequency deviates from the resonant frequency of the system. [10]

2 Designs of Piezoelectric Energy Harvester for Public Roadways

2.1 Selection of Coupling Modes

2.1.1 Introduction of 33- and 31- Mode.

In piezoelectric energy harvesting technologies, there are typically two coupling modes which are 33- and 31- mode. The concepts of 31-mode and 33-mode introduced by Anton, S. and Sodano, H. [19] are illustrated in Figure 2.

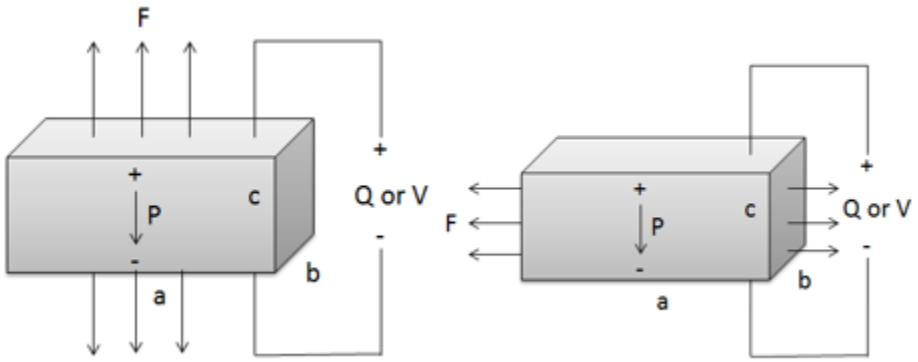

Figure 2. Chart. The illustration of 33- (left) and 31- (right) coupling mode of piezoelectric energy harvesting.

Under 31-mode, piezoelectric material generates electric energy from transverse displacement. For harvester generating energy under 33-mode, the piezoelectric material is usually deformed along its poling direction. The number of exited electric charges, Q, on its pole planes can be calculated as:

$$Q = Fd_{33}$$

Figure 3. Equation. Excited charges of 33-mode.

where F is the force applied on the material's surface and d_{33} is piezoelectric charge constant in 33-mode. The voltage generated can be calculated as:

$$V = \frac{c \times F \times g_{33}}{ab}$$

Figure 4. Equation. 33-mode voltage generation.

where g_{33} is the piezoelectric voltage constant in 33-mode. d_{33} and g_{33} are interchangeable with relative dielectric constant, $\varepsilon_{ij,}$ and vacuum dielectric constant, $\varepsilon_{0:}$

$$g_{33} = \frac{d_{33}}{\varepsilon_{33}\varepsilon_0}$$

Figure 5. Equation. Interchanging equation of g_{33} and d_{33}.

Under 31 mode, piezoelectric materials are usually deformed perpendicular to its polarization direction. The number of excited charges, *Q*, on both polarization planes can be calculated as:

$$\frac{Q}{ab} = \frac{Fd_{31}}{bc}$$

Figure 6. Equation. Excited charges of 31-mode.

The voltage generated can be calculated as:

$$\mathrm{V} = \frac{Fg_{31}}{b}$$

Figure 7. Equation. 31-mode voltage generation.

In the application considered here the ambient mechanical vibration is derived from vehicles of various sizes and speeds traveling over the roadway. This provides a periodic motion to the pavement that in turn causes deflection in the surface of the road.

2.1.2 Simple Output Prediction

To select the right coupling mode as a basic concept of build an energy harvesting system, a simple prediction of the electric output of energy harvester under these two modes are performed.

The plot of real-measured strain is shown as following. Figure 8. Shows a set of strain data collected from real pavement by WF12 sensor. The measurements were taken at three inches below the surface.

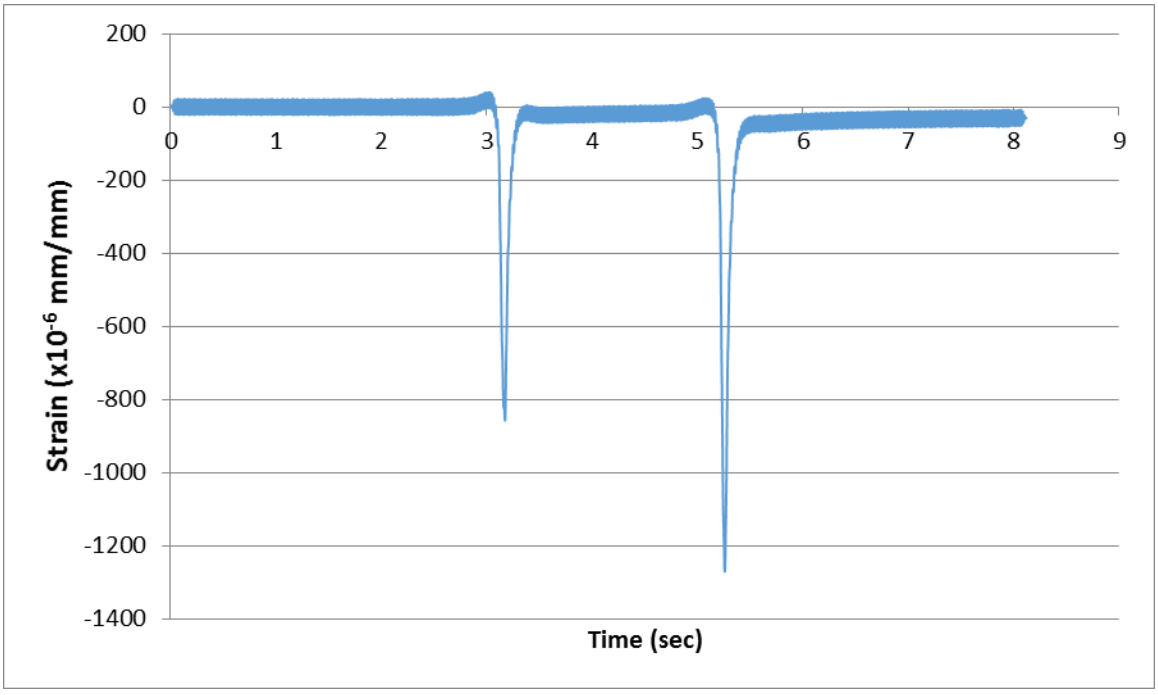

Figure 8. Chart. Strain plots measured by WF12 sensor.

The power output energy is obtained from multiplying the power by time and substituting the force element by stress and cross-section area. The total energy generated can be calculated as:

$$W_{33} = \int_0^t \frac{1}{2}(d_{33}g_{33}Y_{33}^2\varepsilon_{33}^2 abc)dt$$

Figure 9. Equation. Energy generated of 33-mode using strain data.

Only the strain is time-dependent, and then the energy generated can be expressed as:

$$W_{33} = \frac{1}{2}(d_{33}g_{33}Y_{33}^2 abc)\int_0^t \varepsilon_{33}^2 dt$$

Figure 10. Equation. Energy generated of 33-mode.

To obtain the integration of the squared strain in 8 seconds, the measured strain will be squared first. The plot of squared strain is shown in Figure 11.

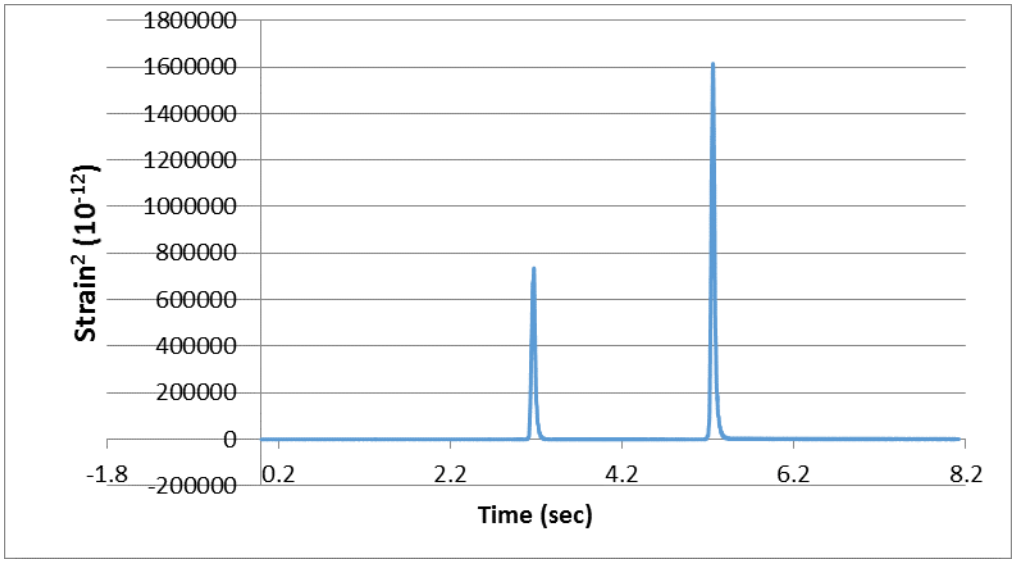

Figure 11. Chart. The squared strain using to calculate the power output

The approximated integration of the product of strain and time from origin to 8.121 seconds is 2.74×10^{-7} (mm/mm) ^{2}x sec. The generated energy computed from this equation is 0.017 joules. Since the modulus of a pavement is a constant, the strain is only related to the stress applied. Therefore, in 33- mode, the energy production of a piezoelectric energy harvester is proportional to the stress applied on it.

Under 31-mode, piezoelectric material generates electric energy from transverse displacement. The productivity is maximized when the carrier vibrates with its resonant frequency. From D. Inman's work, the vibration amplitude of a cantilever-beam excited by the passenger cars can be simply expressed as: [11]

$$y(t) = (0.01) sin \omega_b t$$

Figure 12. Equation. Vibration amplitude of a simple cantilever beam

where

$$\omega_b = \mathrm{v}\left(\frac{km}{hour}\right)\left(\frac{1}{0.006km}\right)\left(\frac{hour}{3600s}\right)\left(\frac{2\pi\, rad}{cycle}\right) = 0.2909\mathrm{v}\ \mathrm{rad/s}$$

Figure 13. Equation. Empirical equation of excitation frequency of vehicle travelling on pavement

In Figure 13, v represents the vehicle's velocity in km/hr and y represents the excitation amplitude, which varies with excitation frequency, ω_b. Since it's concluded that the productivity of an energy harvester under 31-mode is proportional to the excitation amplitude, the power output of the harvester is depending on vehicle's speed. Under

random traffic, the power output will change sinusoidally. To have a more stable power output, this study purposed to design a piezoelectric energy harvester which converts energy under 33-mode.

2.2 Piezoelectric Material

2.2.1 Material Classification

Piezoelectric materials can be classified into the following categories: 1) single crystalline material (as quartz); 2) piezoceramics (as PZTs); 3) piezoelectric semiconductor (as ZnO_2); 4) polymer (as PVDF); 5) piezoelectric composites; and 6) glass ceramics (as $Li_2Si_2O_5$, Ba_2TiSiO_6). These different types of piezoelectric materials have different piezoelectric and mechanical properties.

As a result of its high cost effectiveness, lead-zirconate-titanate (PZT) has been a competitive candidate in many applications among the commercial products. And it also can be built into any shape conveniently.

2.2.2 Material Properties

There is a wide variety of commercial piezoceramics in the market. Understanding the significance of their parameters is necessary for selecting the energy harvesting material. Material with appropriate parameters can convert the energy more efficient.

Material properties of the piezoelectric materials are important factors to energy conversion efficiency. Many studies have explained that the piezoelectric charge constant (effective piezoelectric strain constant), d, and the piezoelectric voltage constant, g, are governing the magnitude of the energy conversion process. [12, 13] They are expressed as d33 and g33 in 33-mode. According to the testing results of Erturk's work under the same condition, the productivity of an energy harvester is greater with higher piezoelectric coefficients (d and g).[14] The author has also concluded that, a smaller elastic compliance contributes to a greater energy productivity under the same load. In Richards et al.'s study, quality factor, Q, is proved as another important factor to the energy productivity. [15] The piezoelectric material with greater quality factor endures less damping during the energy conversion. Such damping causes the generation of heat during the energy conversion process. As a conclusion, energy harvesters with higher quality factor are more efficient on energy conversion. Therefore, to build an efficient energy harvesting system, piezoelectric material with higher piezoelectric coefficients, lower elastic compliance and higher quality factor should be selected.

2.2.3 Piezoelectric Material Selection

Obviously, from the equation listed in Figure. 3, 4, 6 and 7, the electrical productivity of a piezoelectric material is highly depending on d_{31}, d_{33}, g_{31}, and g_{33}.

There are tremendous numbers of piezoceramic products which are suitable for different applications. Commercial product of piezoelectric material from seven piezoceramic companies including APC International Ltd., PCB Piezotronics Inc., Piezo Systems Inc., MIDE, Piezo Technologies, Ceracomp and Morgan Electro Ceramics were investigated

based on the information provided on their web pages. Their PZT products and the piezoelectric properties of candidate products are listed in Table 1. All the information listed has been filtered and some products with inappropriate parameter are not considered as the candidate energy harvesting material in this study. The permittivity has not been compared because there are only few companies have provided it. The product from APC is selected because of their fast shipping and lower price.

Table 1. The candidate piezoceramics for energy harvesting.

Company	Product ID	Piezoelectric Charge Constant(d_{33}, 10^{-12} C/N)	Electromechanical Coupling Factor (k_{33})	Piezoelectric Voltage Constant (g_{33}, 10^{-3} Vm/N)	Q_m
APC	841	300	0.68	25.5	1400
	850	400	0.72	24.8	80
Ceracomp	HPSC 200-145 (Single Crystalline)	1100	0.9		>1000
Morgan	PZT 407-1	325	0.74	30	1200
	PIC 181	265	0.66	25	2000

2.3 Finite Element Analysis

This work focuses on harvesting energy from the deformation induced by traveling vehicles. To work properly under a high-level stress and in a real pavement, the energy harvesting system should be sealed in a protective package. This package contains all piezoelectric materials and redistributes the applied load on the material uniformly. It should be made from tough electric insulated material since the electrodes are integrated into the package. Waterproof is another important feature of this package because leaking water into the package will result in short circuit connection and zero output. Besides the

protective package, it is critical to minimize the stress concentration on the brittle piezoelectric material. Finite Element Method (FEM) analysis is conducted using ABAQUS/Standard to find the optimal spacing and shape of piezoelectric material. In the simulation, same load is applied on the cover of the protective package. The simulation is conducted with different shapes of piezoelectric material. From the simulation results shown in Figure 14, it is obvious that using cubic columns will cause more stress concentration than using cylinders under the same load. Expanding the spacing of cylinders will reduce the stress on the edge of the material.

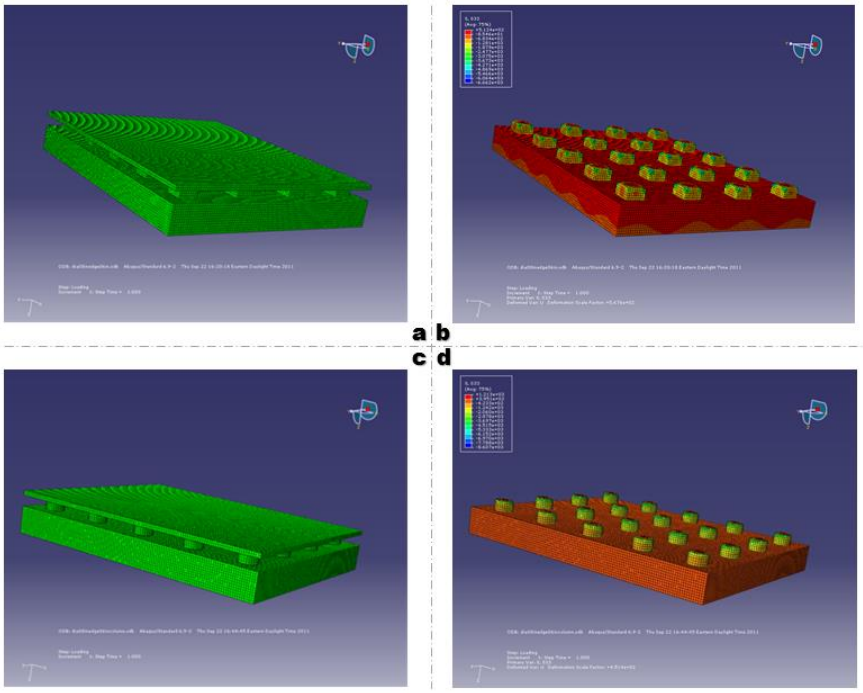

Figure 14. Chart. FEM simulation of load distribution of energy harvester using cubic columns (a. The simulation model; b. The simulation result) and cylinders (c. The simulation model; d. The simulation result).

2.4 Protective Packaging Design

To collect energy from the pavement being deformed, the piezoelectric energy harvester has to be installed in the pavement. To protect the piezoelectric materials from the impact brought by vehicles and ambient environment, they will be sealed in a protective package made from insulating material. Engineering plastic, which is insulating and able to resist the external impact from vehicles with a long lifespan, is selected to build the package. Also, the package has to block fluid or any other chemical and contaminants from the hosting material. They should not have contact with any fluid which may cause the short circuit of positive and negative poles of the material. Another function of the protective package is transferring the stress applied by vehicles uniformly onto the piezoelectric material to extend the lifespan of the material. Since a round-shaped contacting area will have less stress concentration on its edge than any other shapes, the piezoceramic disks are selected to build the harvester. All the positive and negative poles of the piezoceramic disks are connected by several copper electrode bars integrated in the protective package.

2.5 Power Managing Circuit

The extracted energy from piezoelectric energy harvesters could be utilized through various ways after being rectified, or stored in a capacitor or a battery. Then it can be connected to the electric grid and power small electronics or transportation facilities. Figure 15 is a scheme of the potential utilization of the power output from energy the harvesting device.

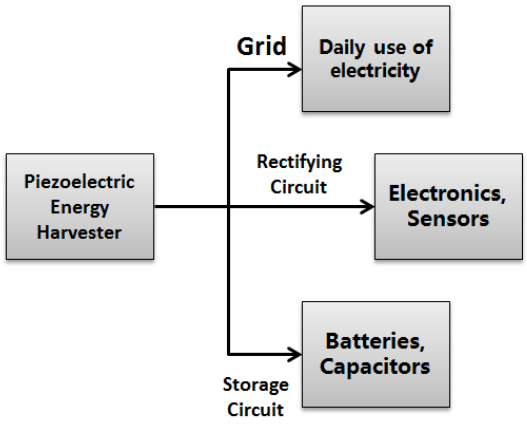

Figure 15. Chart. The potential utilization of the piezoelectric energy harvesting power output.

The ultimate purpose of energy harvesting is to offer a usable power source by converting the ambient wasted energy into electrical energy. Since the external excitation is random, the power output from energy harvesters has varying amplitudes and frequencies. [16] Such power output is not compatible with the energy demands of small- and micro-scale electronics. The varying voltage generated from the piezoelectric material requires rectification before being stored or used. The common solution to provide usable power from an energy harvester is adding an interfacial circuit to it. Recently, many researchers have their focuses on designing an optimized circuit for energy harvesting systems. In the study by Ottman, G. K. et al., a classic optimizing interfacial circuit is developed as shown in Figure 16.[17] It consists of a filter capacitor and a diode rectifier. The authors have proposed another interfacial circuit including a step-down DC-to-DC converter to help managing the electric output of energy harvesting.[18] The converter can regulate an electric energy flow to the target level, which is safe and usable for those electronics. Guyomar D., et al. have brought up the concept of an interfacial circuit in their study,

which is controlled by a switch connected to an inductor.[19] This circuit was named as "Synchronized switch harvesting on inductor (SSHI)". It can significantly improve the conversion efficiency with a programmed input signal to control the switch. Badel A. et al. have proposed two variations to the SSHI, which are Parallel SSHI (PSSHI) and Series SSHI (SSSHI).[20] The voltage regulating device is connected in parallel (Figure 17) and in series (Figure 18) with the piezoelectric harvester in PSSHI and SSSHI, respectively. The combination of the diode capacitor and loading resistor can be replaced by a rechargeable battery. Roundy et al. have proposed a simple charge-pump circuit which can also estimate the energy output per cycle.[7] In the work presented by Jeon, Y.B. et al., a rectifier consisting of four diodes and a capacitor were used to rectify the power output.[8] It has been mentioned that the forward voltage drop of the diodes should be as small as possible to develop the largest possible DC current. Selecting the rectifier with low leakage current is important. Lefeuvre, E. et al. have brought up a concept in the interfacial circuit with different modules having different functions.[21] In this concept, Module 1 rectifies the power output and transfers it into usable energy. Module 2 optimizes the power flow from the output of Module 1. Module 3 (optional) can increase the power output generated from the energy harvesting system under certain circumstances. Figure 19 is a scheme of all the three modules.

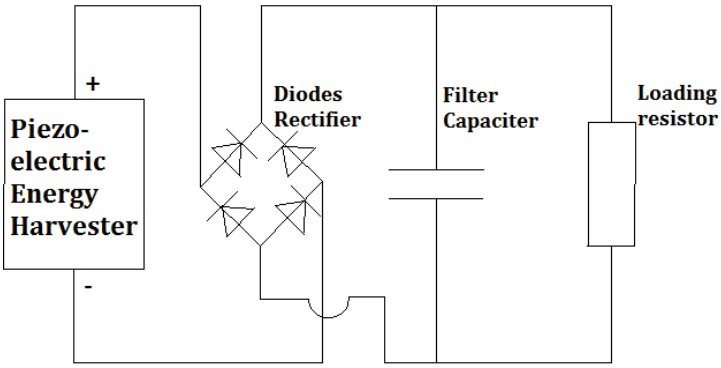

Figure 16. Chart. The layout of the classic power output optimizing interfacial circuit.

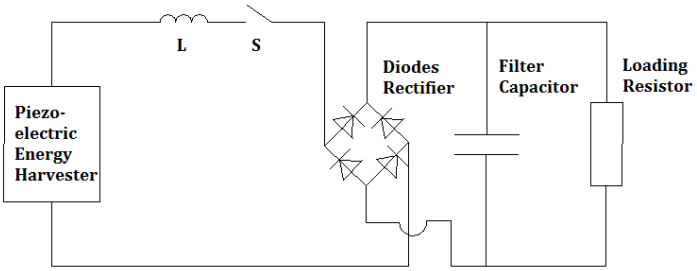

Figure 17. Chart. The layout of the SSSHI interfacial circuit..

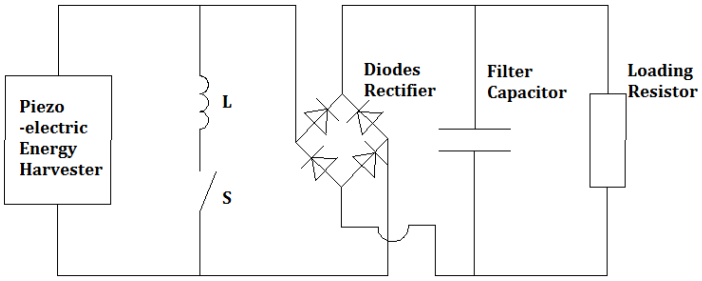

Figure 18. Chart. The layout of the PSSHI interfacial circuit.

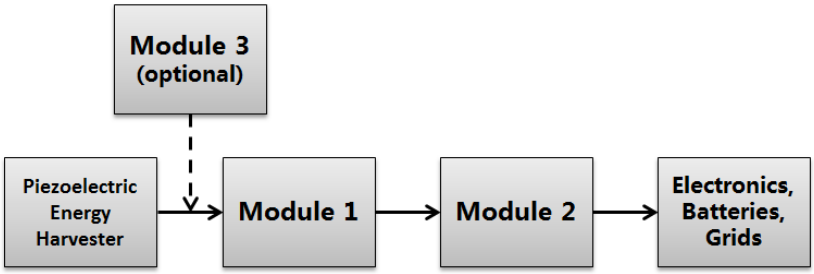

Figure 19. Chart. The scheme of the interfacial circuit for energy harvesting system.

3 Fabrication of Piezoelectric Energy Harvester

3.1 Prototype Energy Harvester

The prototype energy harvester is designed evaluate the simple tests of the purchased piezoelectric disks. It consists a metal cap, a metal base and a nylon tube as protective wall (Figure 20). The piezoceramic discs are stacked in this nylon tube.

Figure 20. Photo. Nylon protective wall.

The nylon tube can be mounted on an aluminum alloy base matching the external diameter of the tube (Figure 21).

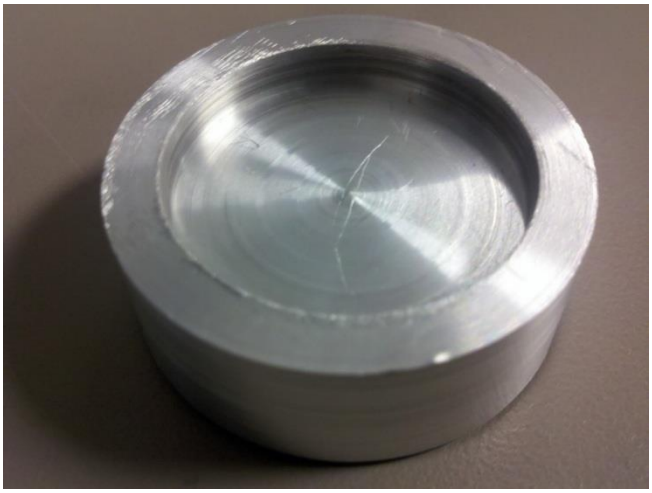

Figure 21. Photo. Aluminum alloy base with circular notch.

The piezoceramic discs are contained in the nylon protective package. The aluminum alloy cover will distribute the load onto the disk (Figrue 22). The assembled prototype energy harvester is shown in Figure 23.

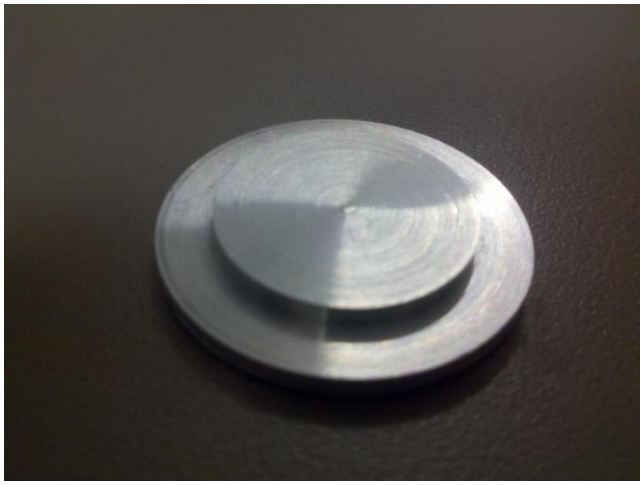

Figure 22. Photo. Aluminum alloy cap.

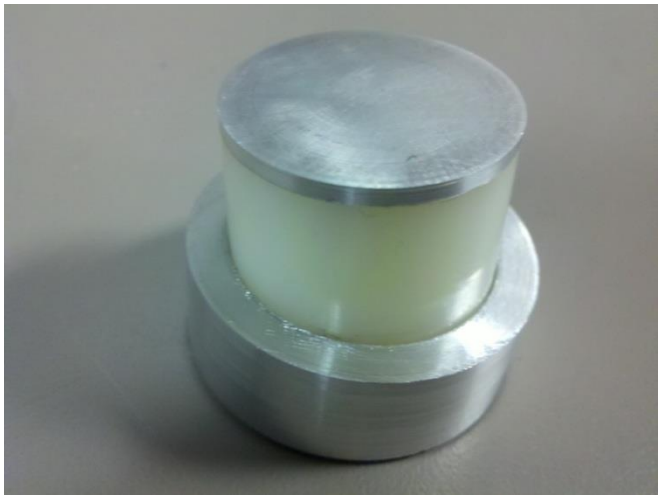

Figure 23. Photo. Assembled proto type piezoelectric energy harvester.

3.2 Assembly Design I (AD1)

AD1 protective package is able to contain six piezoceramic disks. The six disks are all made from PZT and in the same dimension. The thickness of the disks is 14.35mm and the diameter is 31.60mm. The package consists of an aluminum base, an aluminum cover and a protective wall made from nylon. The PZT disks will be hold in six circular notches milled in the aluminum base. The diameter of the notches is 0.5mm larger than piezoceramic disk. The disks thus can be fixed in the notches. Figure 24 and 25 shows the three-dimensional design of the top view of the aluminum base illustrated using AutoCAD. The orange parts in Figure 24 represent the piezoceramic disks. The eight through holes on the base will be all threaded for M6 screws. The geometric dimension of the aluminum base plate is 224.8mmx163.2mmx10mm.

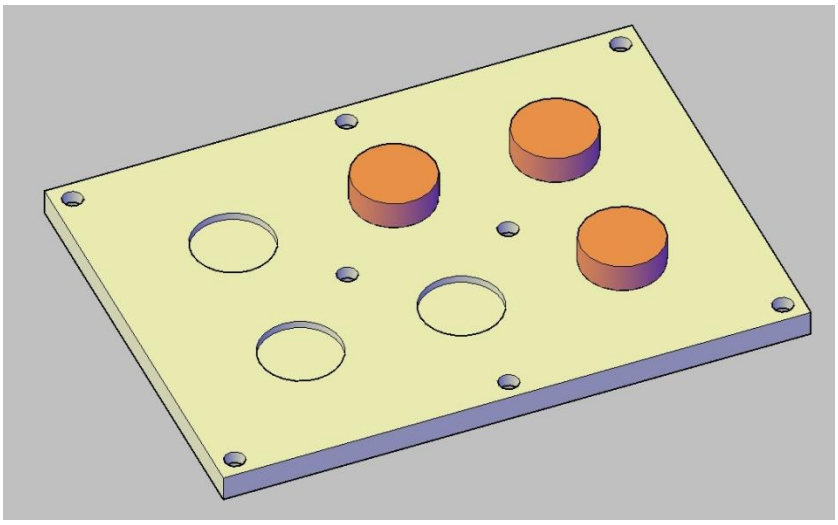

Figure 24. Chart. The 3-D AutoCAD sketch of the base of AD1.

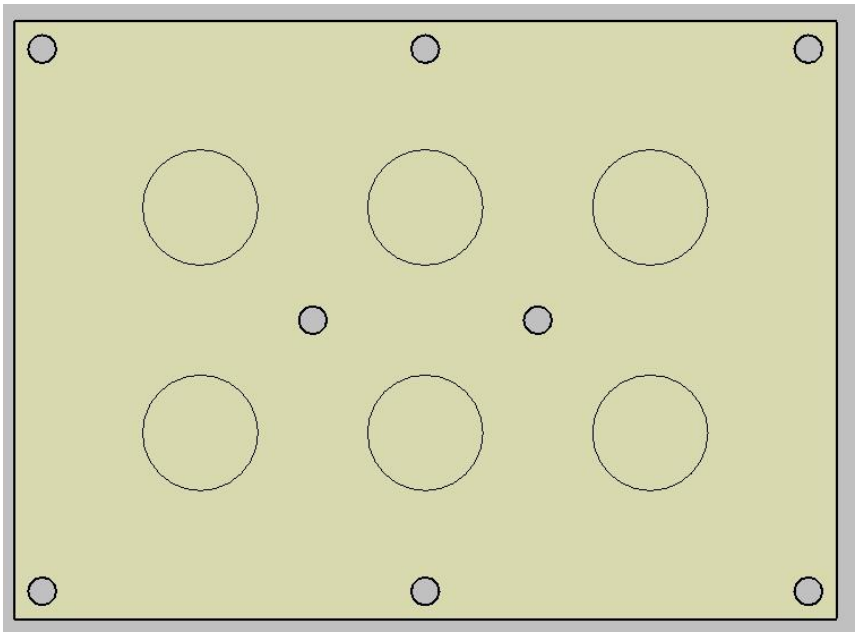

Figure 25. Chart. The top view of the base of the AD1.

Figure 26 represents the enclosing wall which will be sandwiched between the base plate and the cover plate. It should be made from nylon. There will be six holes with no thread in the same locations as the threaded holes on the edge of the base plate. The length and width of the wall are the same as the base plate. The thickness is 15.35mm and the wall thickness is 15mm.

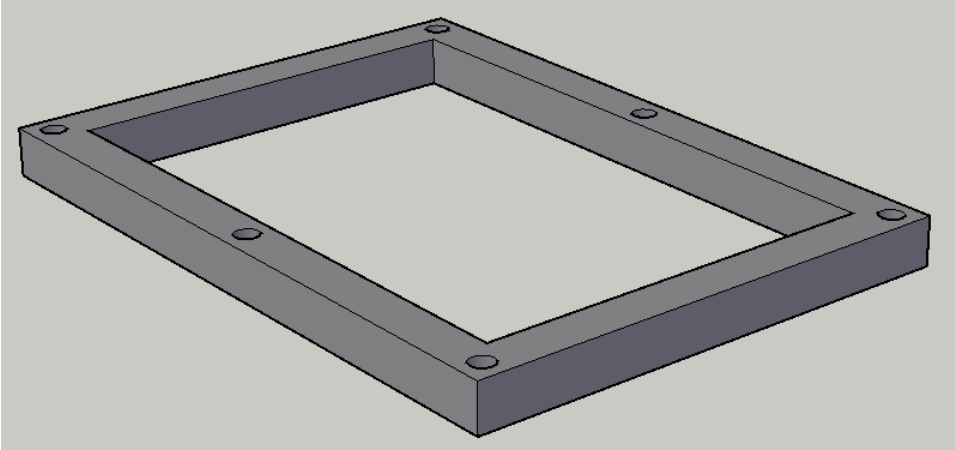

Figure 26. Chart. The 3-D AutoCAD design of the protective of the AD1.

Figure 27 schematically depicts the cover plate made from aluminum as the base plate. It also has eight threaded holes at the same locations and the screws can tight it and base plate up. The bottom part of the cover plate has contact with the piezoceramic disks and applies relative uniform load distribution when the external excitation is not uniform.

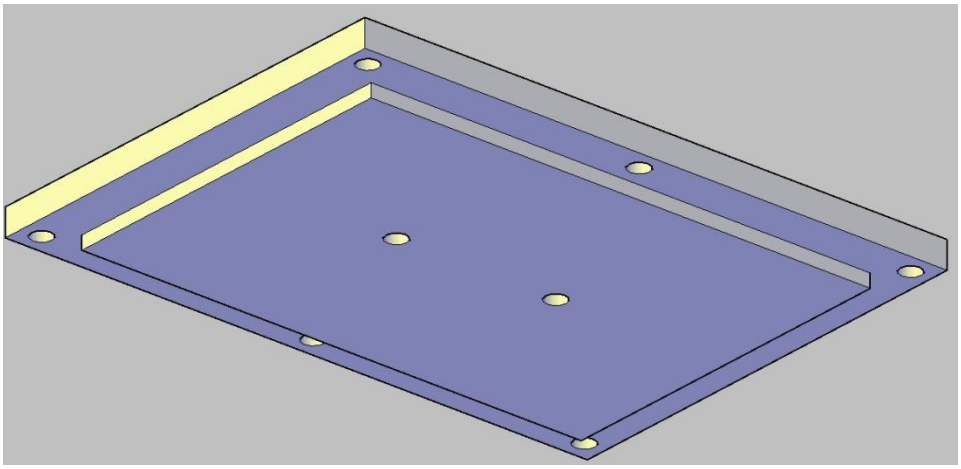

Figure 27. Chart. The 3-D AutoCAD image of the cover plate of the AD1.

Figure 28 and 29 show the three-dimensional image of the assembled energy harvester and the cross section. The aluminum cover plate and base plate are directly contacted with the positive and negative pole of the piezoceramic disks. The two pieces of metal plates therefore can be used as the electrodes. There are two additional threaded holes on

the cover plate and based plate which are using to clamp the electric wire. The wire can be put into the additional hole through a small hole on the side of the cover and base plate. Cable attaching to a short screw is driven into the two plates with the screw. Plastic screws will be used in this design to avoid the potential short-circuit connection and high-voltage penetration. In the cross-sectional view shown in Figure 29, the top part of the cover plate is not contacting with the nylon wall and therefore the bottom part of the cover will have a good contact with the disks when the external excitation is applied.

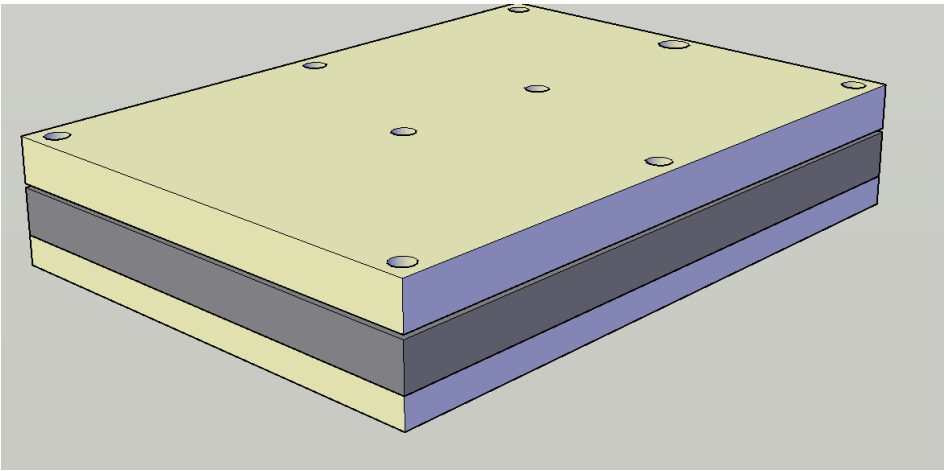

Figure 28. Chart. The 3-D AutoCAD design of the assembled harvester of the Design I

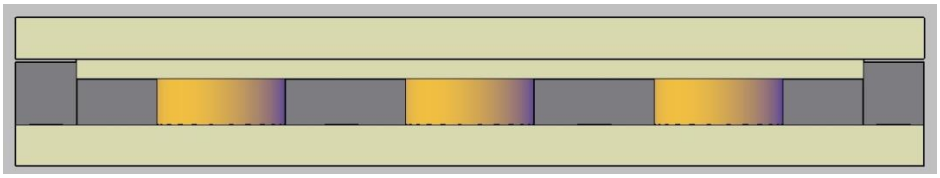

Figure 29. Chart. The cross-sectional view of AD1.

The base plate of the Design I is made from aluminum alloy. The circular notches and the treaded holes is made and flattened with special drill bits. Figure 30 shows the base plate containing three pieces of piezoceramic disks and Figure 31 show the nylon protective wall.

Figure 30. Photo. The base plate of the Design I.

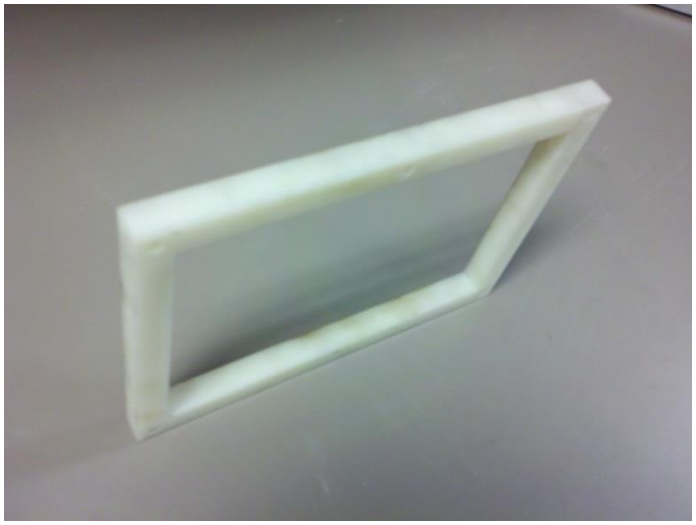

Figure 31. Photo. The enclosing wall of the Design I.

Figure 32 depicts the cover plate of the design I. The cover plate is machined from a 15mm-thick aluminum alloy board. Part of the edge of the board is cut off and eight threaded holes are drilled. The hole marked with red circle in Figure 32 is using to clamp the electric wire.

Figure 32. Photo. . The cover plate of the Design I (left) top view, (right) side view

The Figure 33 shows the assembled energy harvester, and as shown in Figure 33, there is a 1-mm space between the top part of the cover plate and the enclosing wall.

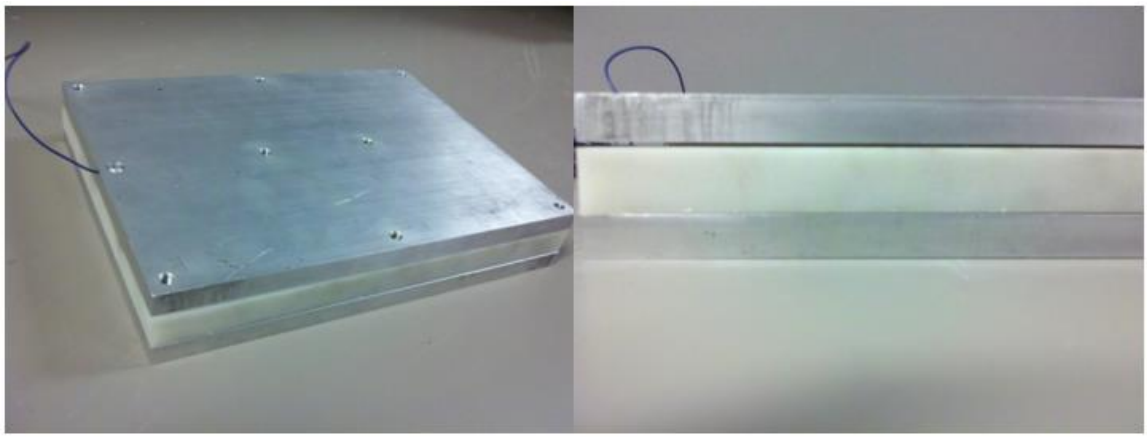

Figure 33. Photo. The assembled energy harvester of the Design I (left) top view, (right) cross section.

3.3 Assembly Design II (AD2)

The second package is able to contain 20 pieces of the piezoceramic disks. The disks are made from PZT with the thickness of10.35mm and the diameter of 24.85mm. The aluminum alloy cover and base are replaced by cement concrete ones to lower the cost.

AD2 consists of a cement concrete base slab and an aluminum cover. They will be tightened to each other by screws.

Figure 34 shows the AutoCAD three-dimensional design of the AD2. The geometric dimension of the slab is 304.25mm x 259.4mm x 39.85mm. The orange part in Figure 34 represents the piezoceramic disks and the green part represents the protecting tube. Each protecting tube holds one disk, which are connected to a metal electrode sealed in the concrete. There are four electrodes in the concrete base and each of them holds five tubes and disks. There are six through holes made in the concrete for screws and they are created by six plastic tubes when the concrete is setting.

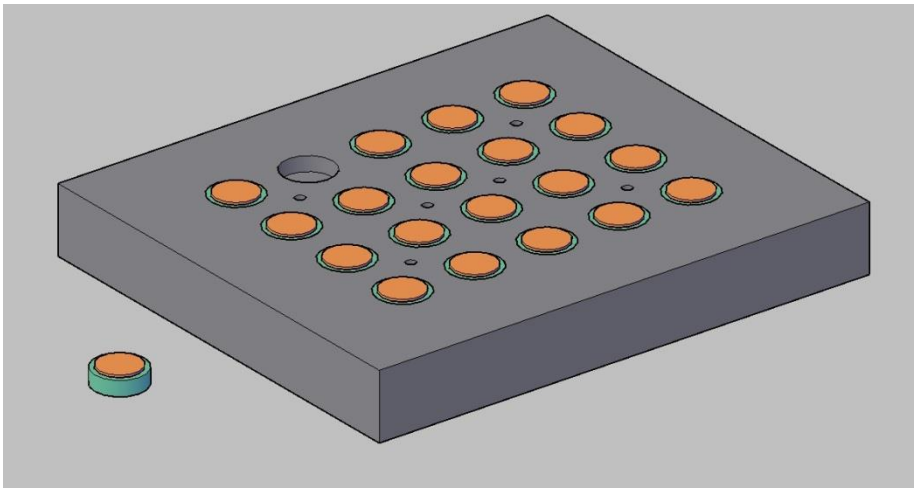

Figure 34. Chart. The 3-D AutoCAD design of the cement concrete slab of the Design II.

Figure 35 is the 3D design of the aluminum cover plate. There are six threaded holes for M6 screws on the aluminum cover for the screws went through the concrete slab. The length and the width of the cover plate are the same as the concrete slab and the thickness is 10mm. There is also an additional threaded hole at the edge of plate to clamp the

electric wire. Figure 36 shows the AutoCAD image of the assembled energy harvester with cement concrete package.

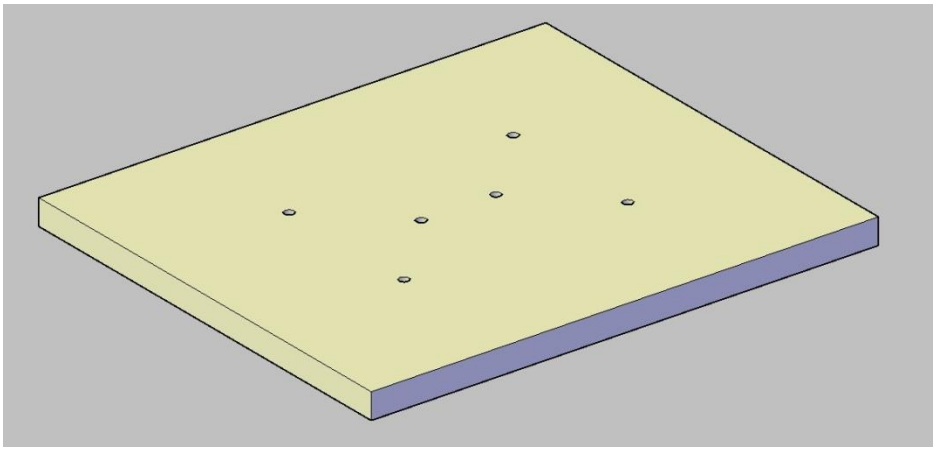

Figure 35.Chart. The 3-D AutoCAD design of the aluminum cover plate of AD2

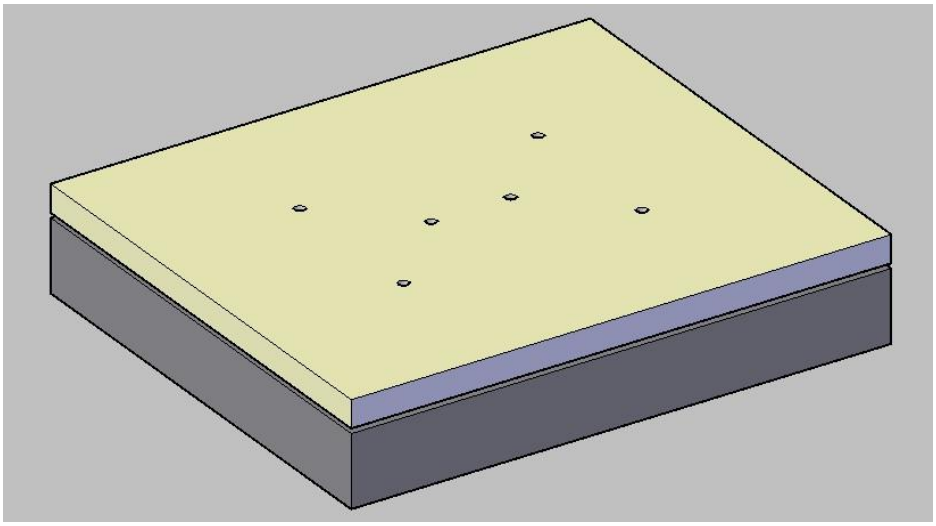

Figure 36. Chart. The 3-D AutoCAD design of the assembled energy harvester of AD II

A casting mold is assembled to make the cement concrete base. Firstly, twenty protecting tubes are glued onto four aluminum electrodes using epoxy. Figure 37 shows the aluminum strip with five protecting tubes attached on.

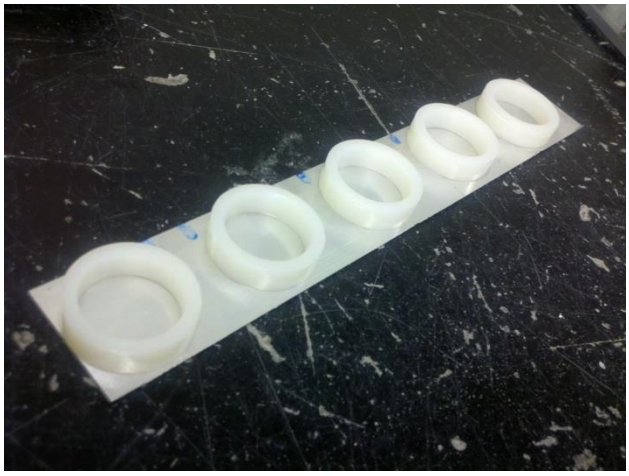

Figure 37. Photo. The aluminum strip with protecting tubes attached on.

Then six cut PVC tubes are glued on a plastic board. It takes 12 hours for the epoxy to reach 80% of its maximum strength. Four wood strips are cut into specific dimensions and assembled with screws as an enclosing wall. Then the assembled wood strips are glued on the plastic board by using silicon sealant. Figure 38 shows the fabricated mold for casting the cement concrete. Lastly, the electric wires are connected through the hole at one end of the metal strips which is marked with red circle in Figure 38. Then the wires connecting to the strips is brought out from the mold through a hole on one wood strip which is marked with blue circle in Figure 38.

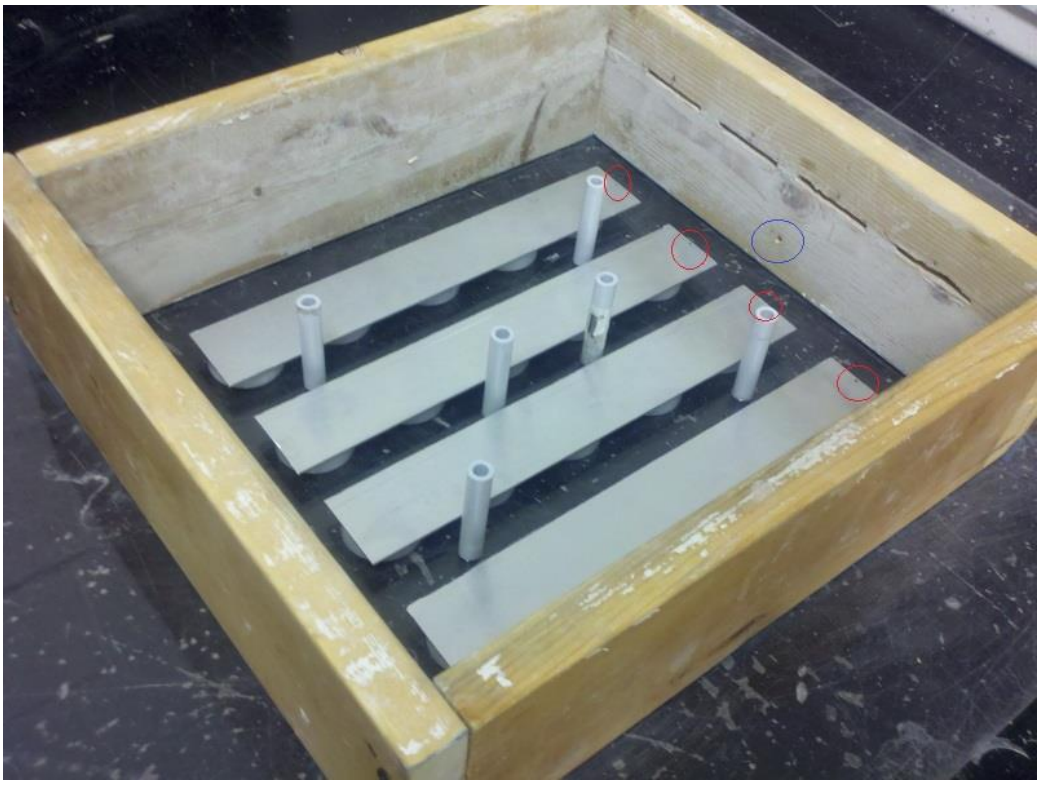

Figure 38. Photo. The assembled mold without electric wires.

The composition of modern concrete is cement, sand, gravel, water, mineral admixture and some other additives. Pre-mixed concrete is used to cast the cement concrete slab. The micro fiber, shrinkage reducing and the high-range water-reducing admixture are added to ensure small shrinkage, good workability and high strength. The Eclipse and the ADVA140M are provided by Grace Co. as the shrinkage reducing admixture and the water-reducing admixture. Multi-Mix 80 Micro Fiber is provided by PSI Fibers. The composition of the mix which will be added into the pre-mixed concrete is shown in Table 1

Table 2. The amount of the adding mix.

Premixed concrete kg	Super plasticizer g	Shrinkage reducing g	Fiber g	W g
10.00	20.0	35.0	4.0	1200.0

Firstly, the pre-mixed concrete is sieved to remove the gravels with diameter larger than 9.75mm. Then the micro fiber is added into the pre-mixed concrete mix and it is stirred for three minutes. Then the water, the shrinkage-reducing admixture and the high-range water-reducing admixture are added. After being stirred for about ten minutes, the fresh concrete mix is poured into the assembled mold until it reaches the top of the screw tunnel. At the end, the surface is flattened using a trowel. The cement concrete slab would be set after 18 hours and the wood walls are removed. Figure 39 and 40 depict the concrete slab and the assembled energy harvester of AD2.

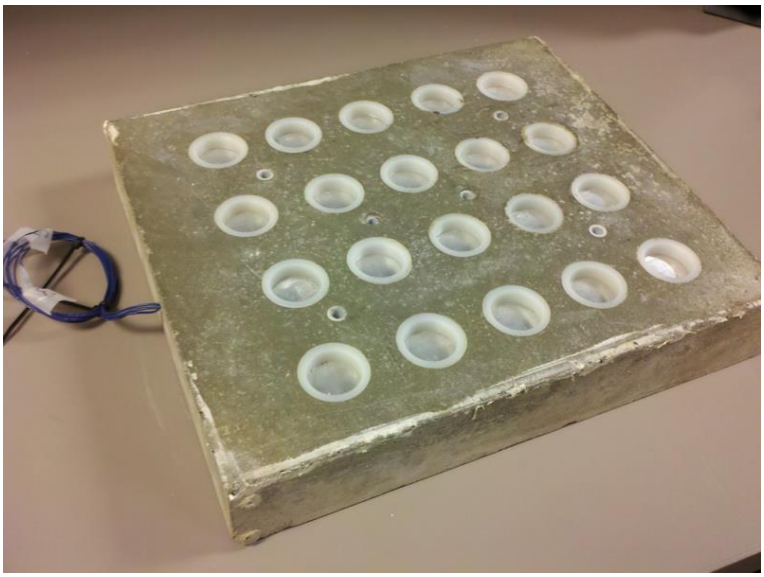

Figure 39. Photo. The fabricated AD2 energy harvester.

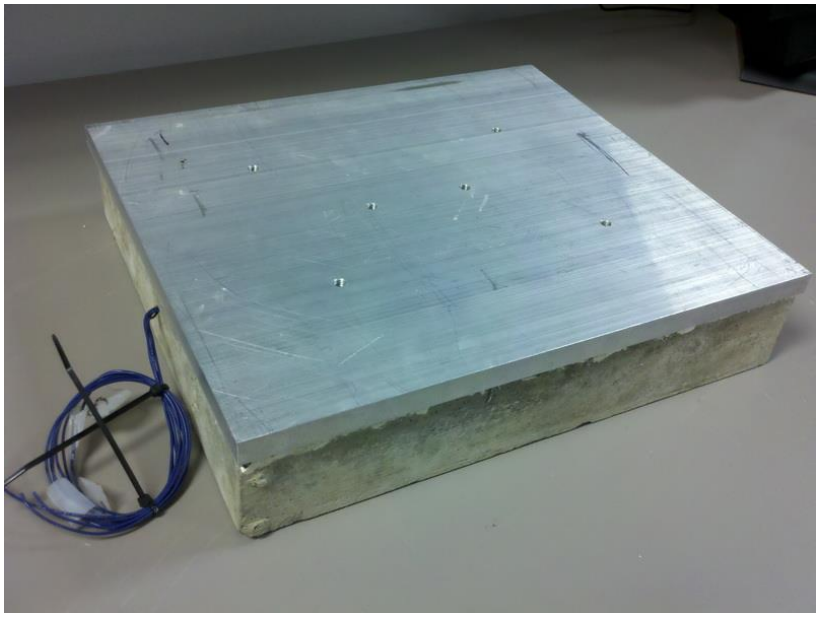

Figure 40. Photo. The assembled energy harvester of AD2

3.4 Assembly Design III (AD3)

In the Assembly Design II, the piezoceramic disks were contained in protective tubes. It was very challenging to fabricate 20 plastic tubes in the exact same thickness. Any one of the tube having thickness different to others' would result in an uneven contacting plane and will cause additional stress concentrations. Uneven contacting plane will lower the power output of the energy harvester and the durability of piezoelectric material. Thus the design with protective tubes is not an option for mass production (its fabrication cost is also high). Assembly Design III follows almost the same design concept of Assembly Design II, which has cement concrete base holder and aluminum alloy cover. Figure 41 is the 3D model of the Assembly Design III build using AutoCAD.

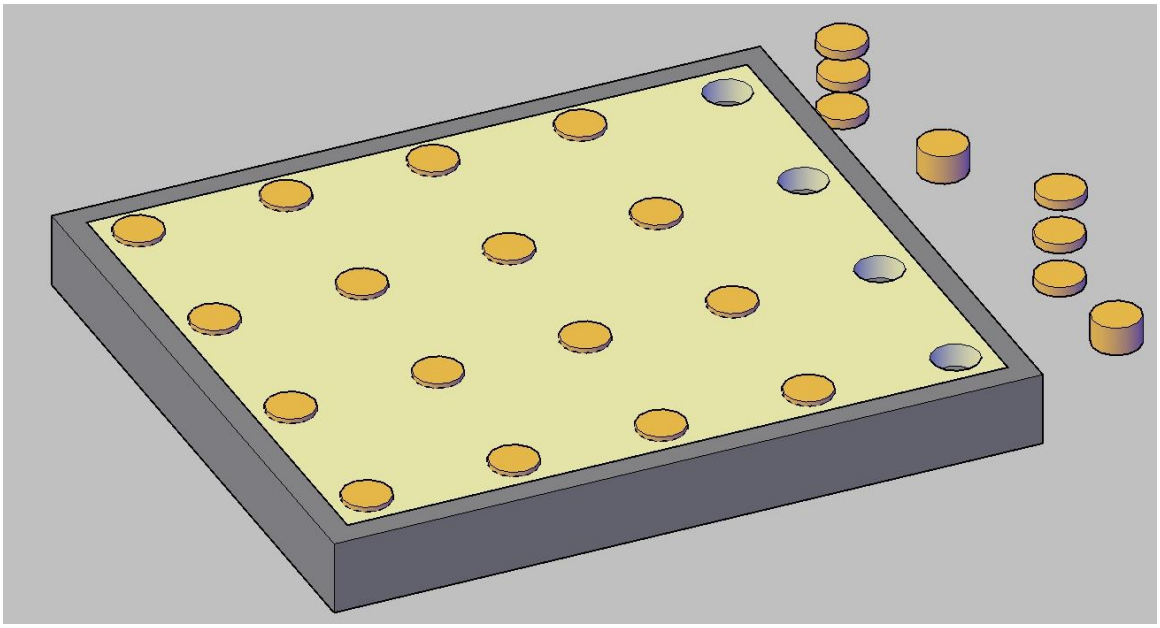

Figure 41. Chart. Three dimensional view of the Assembly Design III.

In Assembly Design III, the protective tubes are replaced by a plastic board with several holes having the same diameter of the piezoceramic disk. The contacting plane is even and the fabrication cost is lower. The electrodes will be attached under the plastic board. By validating this design, the power output of stacking mode and single-layer mode can be tested at the same time under the same conditions. The yellow part in Figure 41 is the plastic board and the grey part is the cement concrete holder. Figure 42 is the energy harvester fabricated following Assembly Design III without aluminum alloy cover.

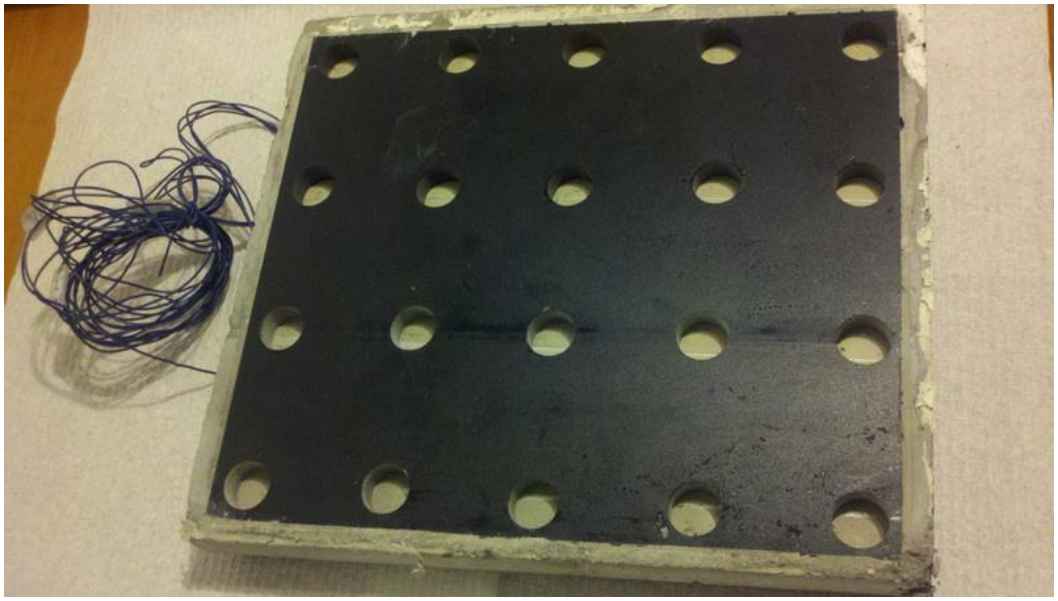

Figure 42. Photo. The fabricated energy harvester following Assembly Design III.

3.5 Assembly Design IV (AD4)

Theoretically, the stress distribution on the top of the piezoceramic disks is more uniform when a preload is applied. Adding screws on the energy harvester can also restrict the lateral movement of the cover. But in the field test, the energy harvesters delivered less electricity after the screws are tightened. This reduction of the energy output could be caused by the imperfect machining process leading to the friction between the screws and the surroundings. To increase the energy output, AD4 is developed as a screw-free packaging design. AD4 has cement base holder and aluminum alloy cover the same as in the previous designs. A protective board is embedded in the cement base holder of AD4. Figure 43 is a three-dimensional sketch of the assembled AD4. The blue part is the aluminum alloy cover and the gray part is the cement concrete holder. The lateral movement of the aluminum cover is restricted by a water-sealing rubber attached along the inner sides of the cement concrete holder. The color of the rubber in the sketch is

black. The aluminum cover is slightly elevated from cement concrete holder to ensure a better contact.

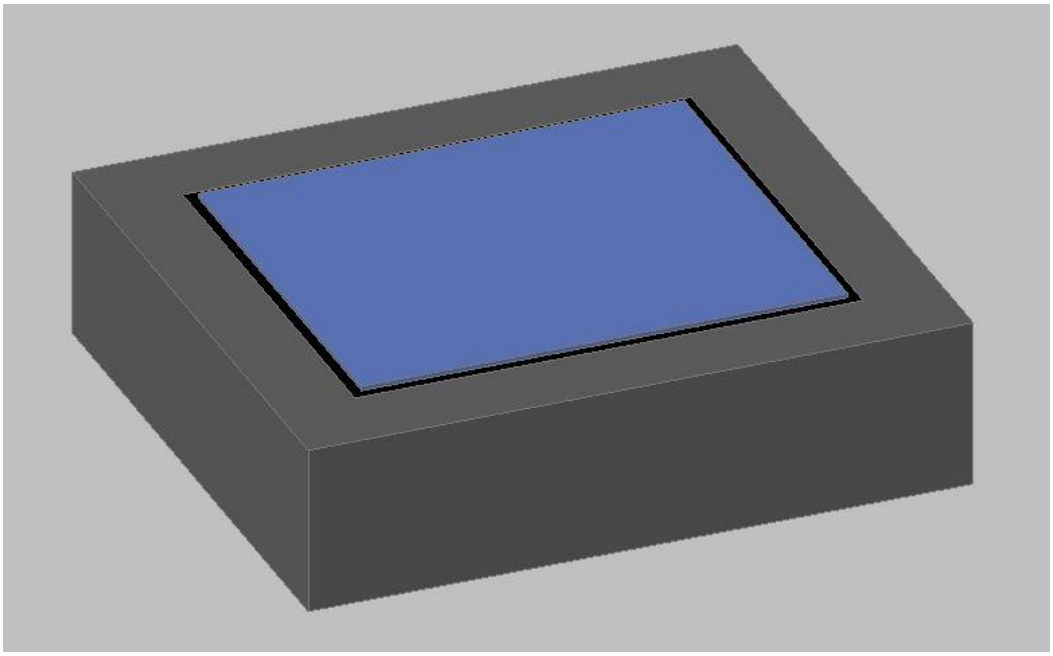

Figure 43. Chart. Three dimensional view of the Assembly Design IV

AD4 has five parts as shown in Figure 44:

1. Aluminum alloy cover;
2. Water sealing rubber;
3. Piezoceramic disks;
4. Protective board;
5. Cement concrete holder.

The positions and the dimensions of the holes on the protective board and the thickness of the board may vary with the dimensions of the piezoceramic disks. Figure 45 is a picture of the actual energy harvester fabricated following AD4.

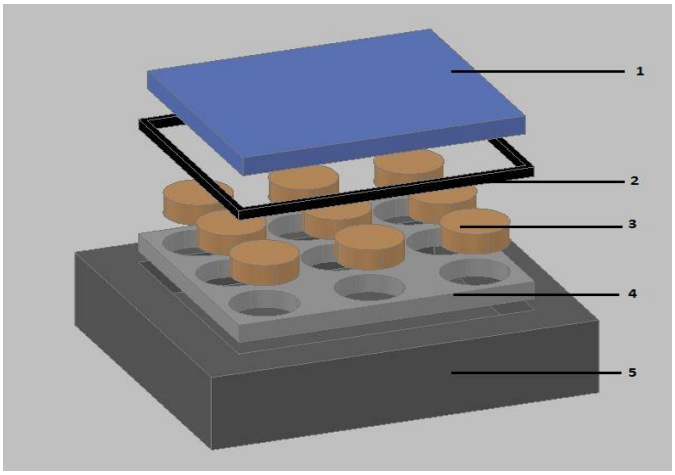

Figure 44. Chart. Three dimensional view of the Assembly Design IV (disassembled).

Figure 45 shows the energy harvester fabricated following AD4 with the aluminum cover and with the aluminum cover removed.

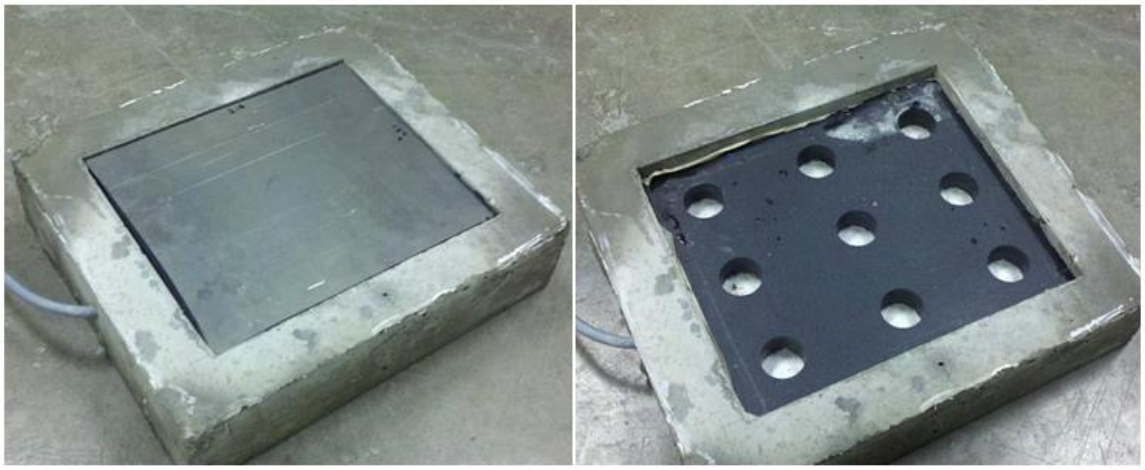

Figure 45. Photo. The energy harvester following the concept of AD4 (left) with aluminum cover, (right) with aluminum cover removed.

3.6 Assembly Design V (AD5)

Although the cement concrete is less costly with enough stiffness to hold the piezoceramic disks, it's very heavy, hard to carry and install. To reduce the weight of the harvester, MDS-filled cast nylon engineering plastic is selected to build new protective

package instead of the cement concrete in AD5. This type of nylon has very high modulus of elasticity which is strong enough to hold the piezoceramic disks. Figure 46 illustrates the three dimensional sketch of AD5. As shown in the picture, the blue part is the aluminum alloy cover; the gray part is the plastic holder wall and the black part is the sealing rubber.

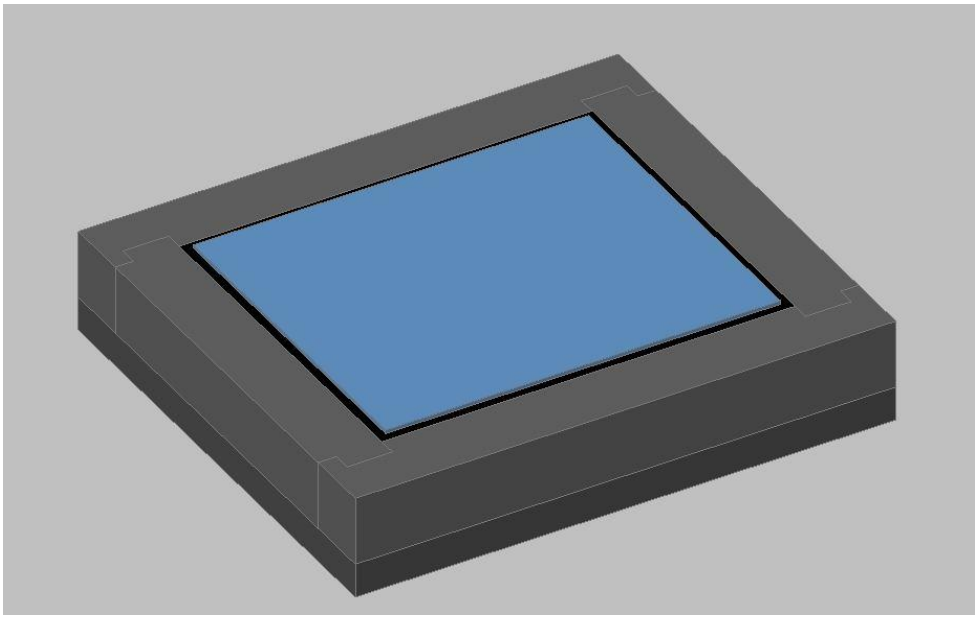

Figure 46. Chart. Three dimensional design of the Assembly Design V

Figure 47 depicts the major components of AD5, it has six major parts:

1. Aluminum alloy cover;
2. Protective walls (four pieces, MDS-filled plastic);
3. Piezoceramic disks;
4. Protective board (PVC);
5. Base holder;
6. Water sealing rubber.

Like AD4, the lateral movement of the aluminum cover is restricted by the water-sealing rubber (it allows vertical movements). Figure 48 is the actual fabricated energy harvester following AD5. It shows the harvester with the aluminum cover and with cover removed.

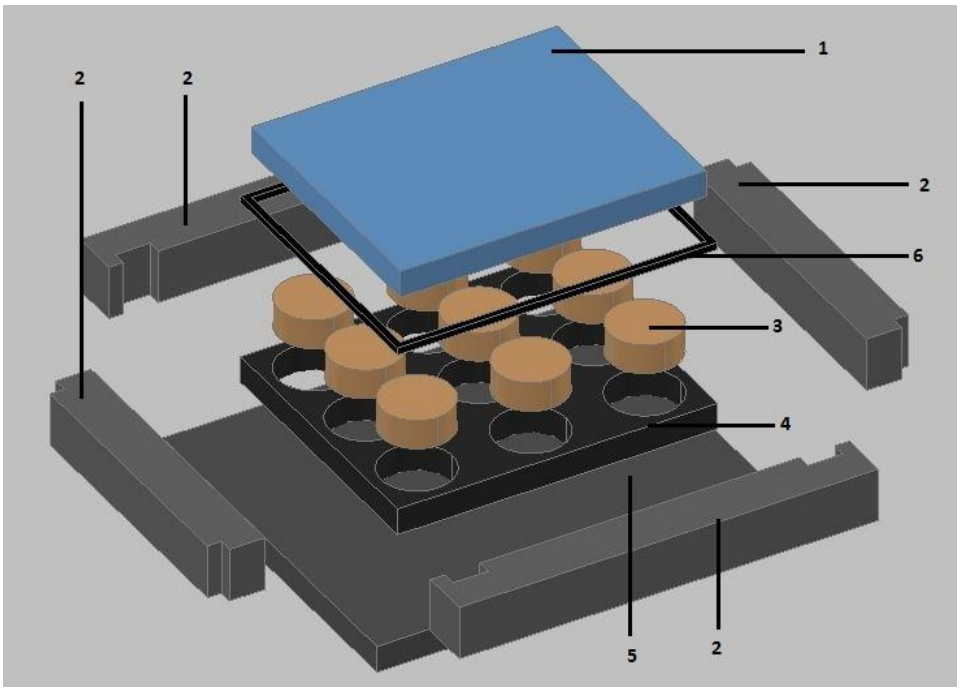

Figure 47. Chart. Three dimensional view of the Assembly Design V (disassembled).

Figure 48. Photo. The energy harvester following the concept of AD5 (left) with aluminum cover, (right) without aluminum cover.

3.7 Assembly Design VI (AD6)

In the previous assembly designs, during the assembling process, some piezoceramic disk didn't have a good contact with the aluminum cover because of the thicknesses of the piezoceramic disks are different (even it's under tolerance). In AD6, MDS-filled-cast-nylon is used to build the cover instead of the aluminum alloy. This material have very small deformation under loading which is enough to have good contact with every piezoceramic disks. Copper-alloy electrodes will be attached under the cover. The aluminum-alloy negative electrodes are also replaced by copper alloy which has a better electric conductivity.

Figure 49 is a three-dimensional sketch of the assembled AD6. The cover piece is made from MDS-filled cast nylon. As in the previous design, water-sealing rubber is attached on the inner side of the protective wall. The lateral movement of the cover piece is limited by the rubber. The dark grey part represents the PVC material, the light grey part represents the MDS-filled cast nylon and the black part represents the water-sealing rubber.

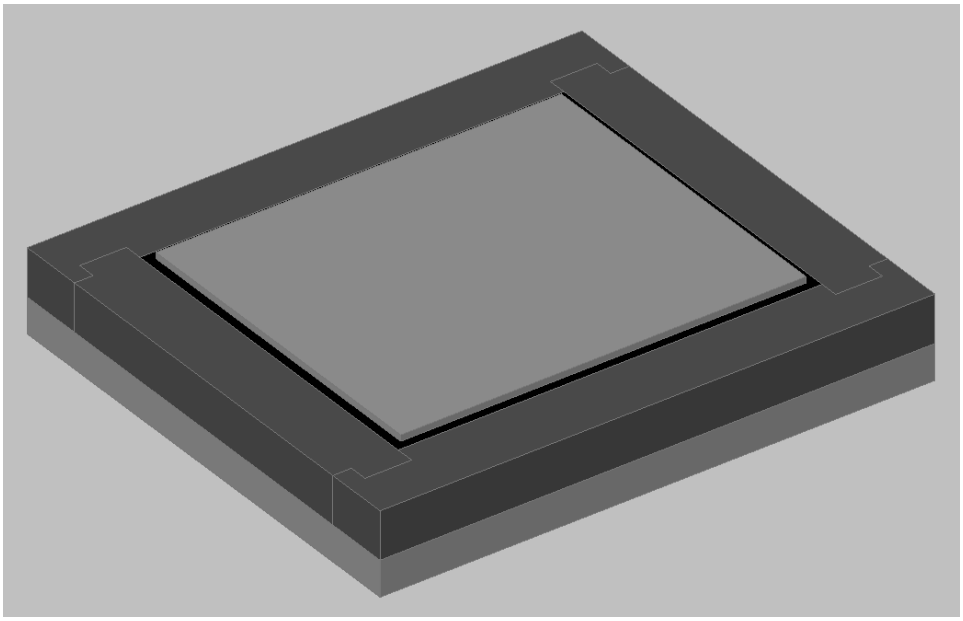

Figure 49. Chart. Three dimensional view of the Assembly Design IV.

AD6 has seven parts as shown in Figure 50:

- MDS-filled cast nylon cover;
- Water sealing rubber;
- Copper-alloy positive (upper) and negative (lower) electrodes;
- Protective walls;
- Piezoceramic disks;
- Protective board;
- MDS-filled cast nylon base board.

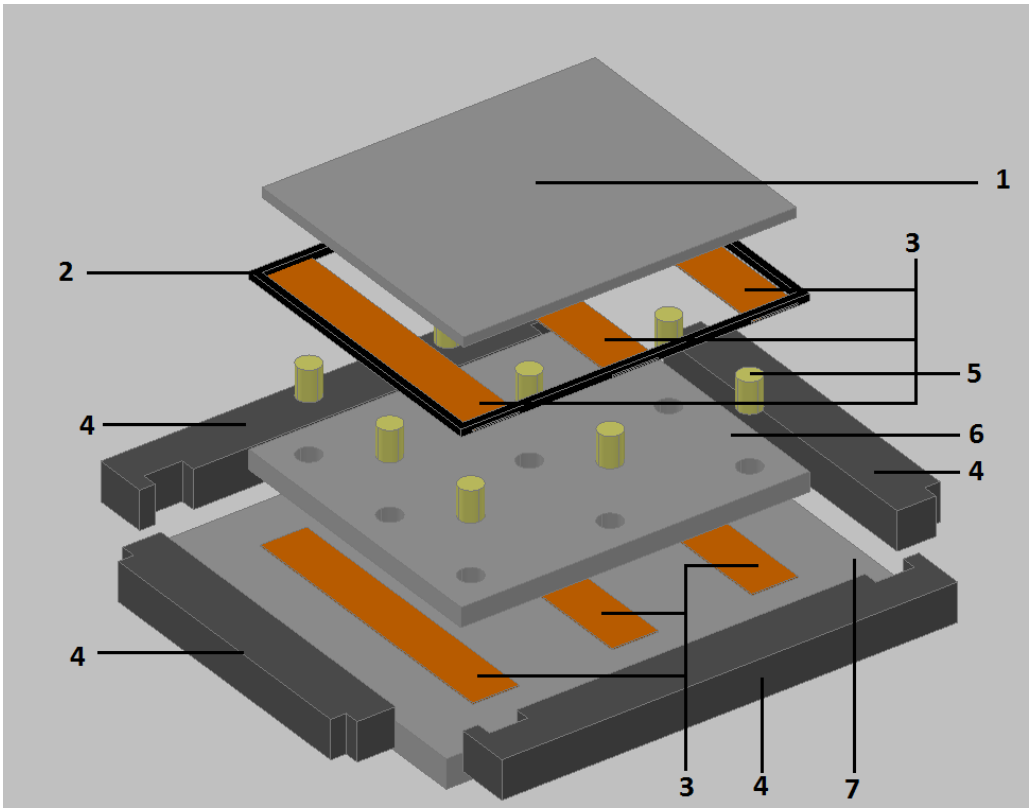

Figure 50. Chart. Three dimensional view of the Assembly Design VI (disassembled).

Figure 51 and 52 shows the disassembled PVC protective walls and the assembled one lying on the MDS-filled-cast-nylon base board.

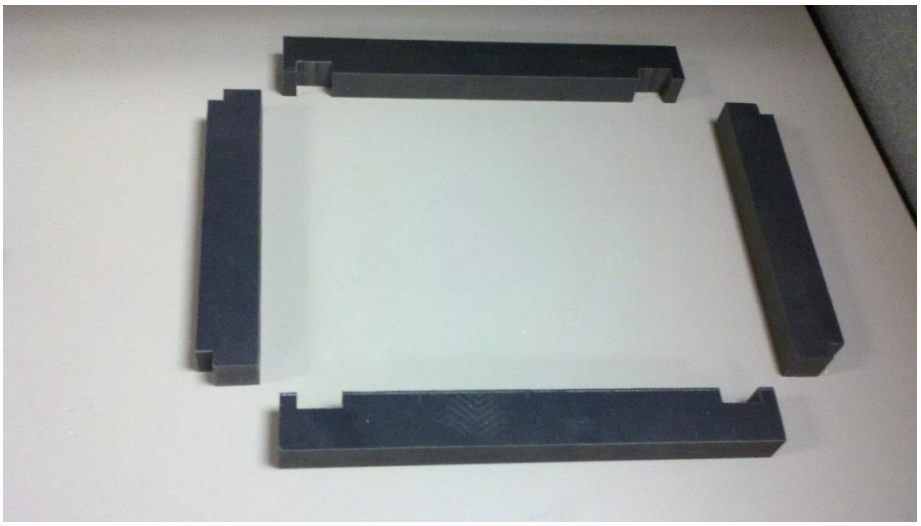

Figure 51. Photo. Disassembled PVC protective walls.

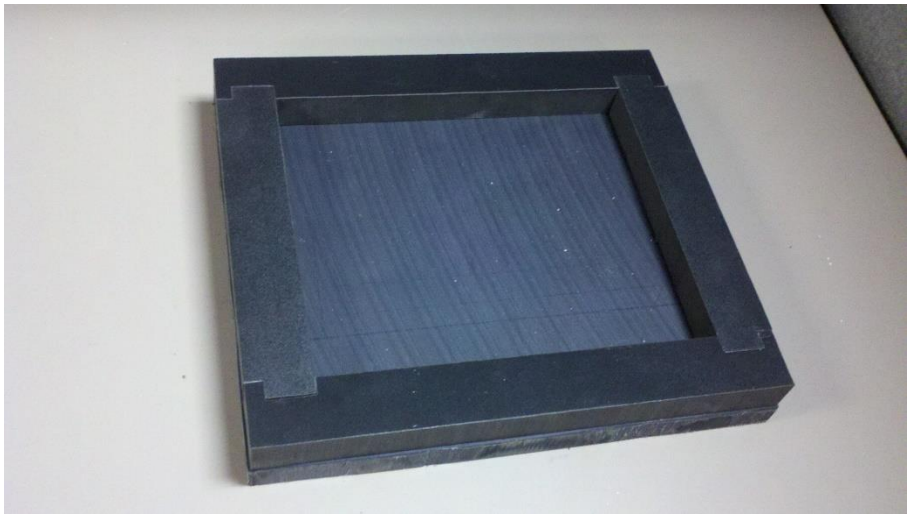

Figure 52. Photo. The assembled protective walls lying on MDS-filled-cast-nylon base board.

Figure 53 depicts the MDS-filled-cast-nylon cover piece. The copper-alloy positive electrodes are attached on the cover and connected by one cable.

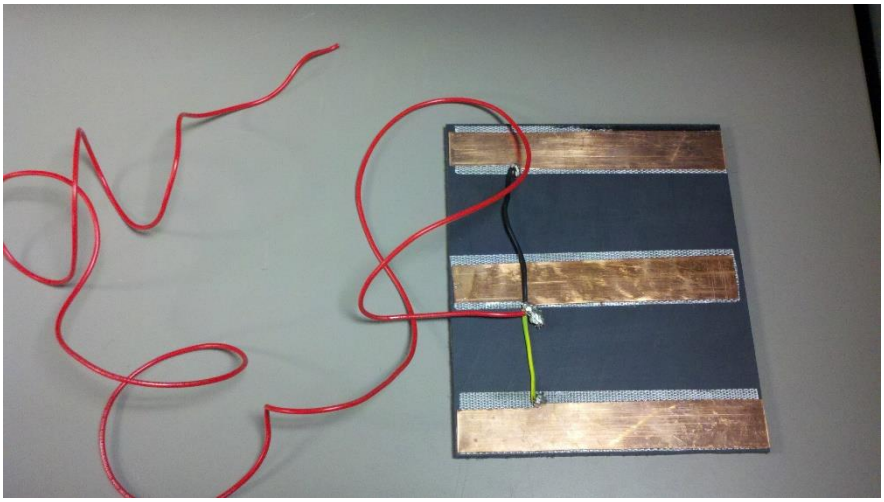

Figure 53. Photo. The MDS-filled-cast-nylon cover with copper-alloy positive electrodes attached.

Figure 54 depicts the assembled energy harvester following AD6 without the cover. The copper-alloy negative electrodes are attached under the protective board.

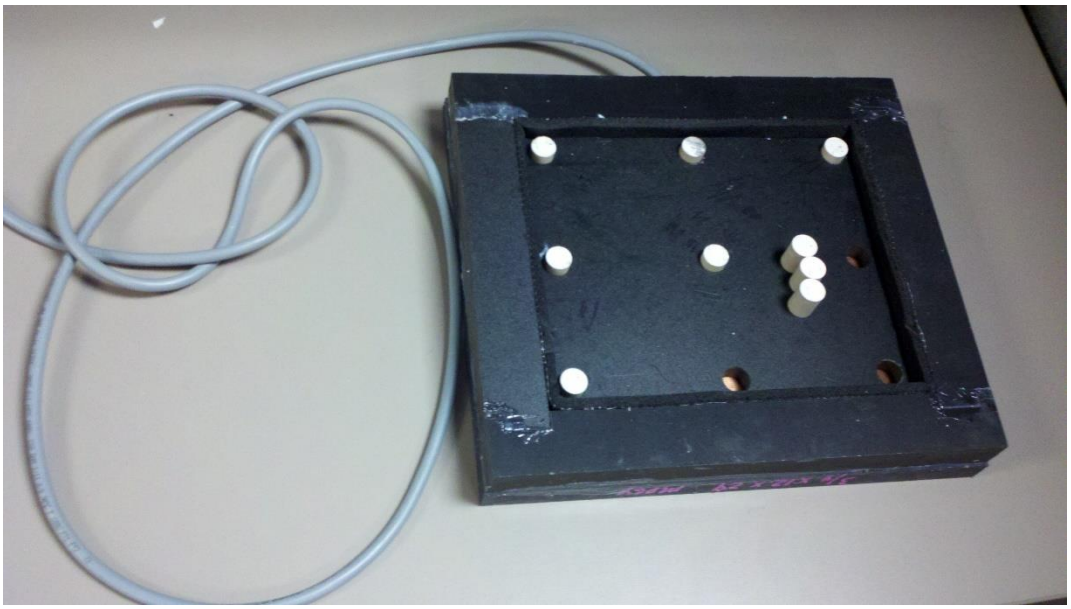

Figure 54. Photo. The assembled energy harvester following AD6 without the cover.

3.8 Assembly Design VII (AD7)

The square-shape rubber has provided very strong water-proof function to the harvester without any loading. However, a problem was encountered during the simple test that it still allows too much lateral movement of the cover. This material is able to seal the water only under enough compression. Lateral movement brings the risk that one side of this rubber material might lose the compression. In AD7, screws and washers are employed to provide lateral restriction. And the small cover in AD6 is replaced by a bigger cover to eliminate the lateral movement. Figure 55 and 56 are three-dimensional sketches of the assembled AD7. To further increase water proof function, protective wall in AD7 is going to be cut directly from a plastic board instead of assembling four strips together in AD7. Grooves were cut on the bottom of the cover to hold the positive electrodes. Figure 57 shows the bottom view of the cover.

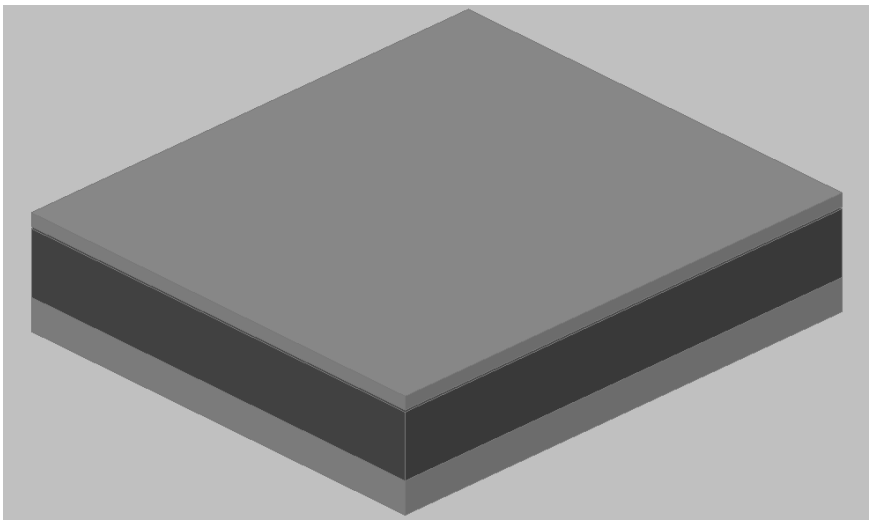

Figure 55. Chart. Three dimensional design of the Assembly Design VII.

AD7 has six parts as shown in Figure 55:

1. MDS-filled-cast-nylon cover;
2. Copper-alloy positive (upper) and negative (lower) electrodes;
3. Chemical-resisting-PVC protective walls;
4. Piezoceramic disks;
5. PVC-Foam protective board;
6. MDS-filled-cast-nylon base board.

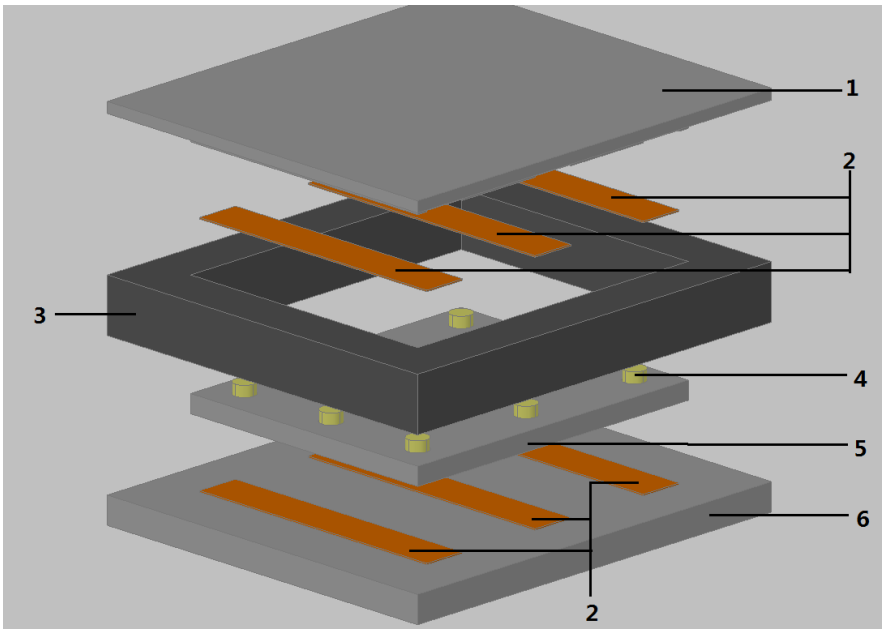

Figure 56. Chart. Three dimensional view of the Assembly Design VII (disassembled).

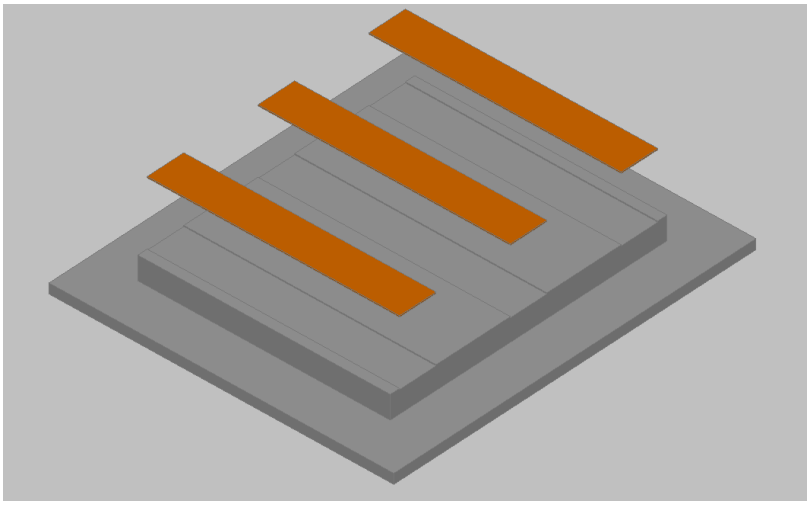

Figure 57. Chart. Three dimensional bottom view of the Assembly Design VII.

The fabricated energy harvester following AD7 without cover is shown in Figure 58. The cover is depicted in Figure 59.

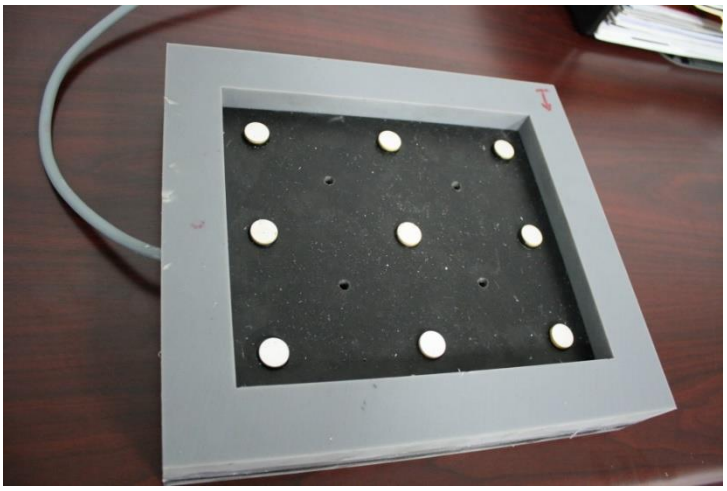

Figure 58. Photo. The energy harvester fabricated following AD7 (without cover).

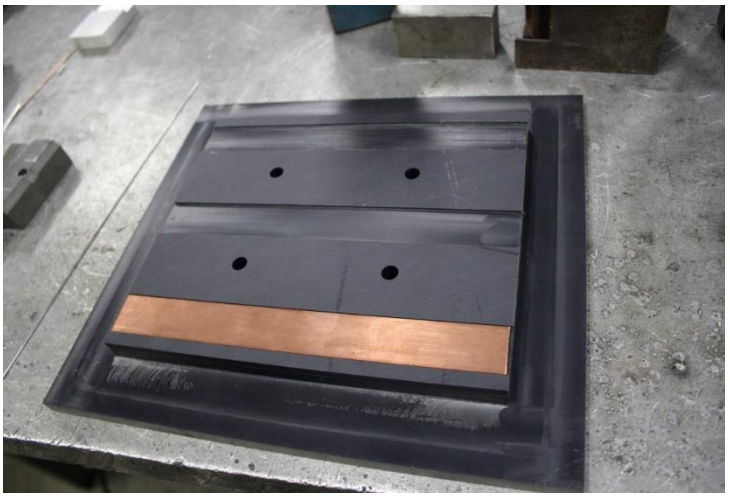

Figure 59. Photo. The cover of the fabricated energy harvester following AD7.

The assembled energy harvester is shown in Figure 60.

Figure 60. Photo. The energyharvester fabricated following AD7 (assembled).

Moving of the cable during laboratory tests and the installation might cause damage to the sealing material around cable. To avoid such damage, plastic flanges is used to protect the end of the cable. The wide end of the flange has enough space to contain both positive and negative cables. The inside of the flange will be filled with water-proof silicone which allows enough movement of the cables. Epoxy provided by Virginia Department of Transportation (VDOT), or the water-proof silicone will be used to fix the flange on the harvester. Figure 61 shows the candidate flange.

Figure 61. Photo. The candidate flange for protecting the cable exit in the Trouville installation.

3.9 Assembly Design VIII (AD8)

To improve the performance of the piezoelectric energy harvester, bar-shaped piezoceramic material was introduced. Assembly Design VIII is a new protective package design for the bar-shaped piezoceramic material. It has very similar concept to the previous ADs which utilize engineering plastic blocks and distribute the load uniformly by the cover. A thicker copper electrode is used in this design (1/8”). Figure 62 is a three-dimensional sketch of the assembled AD8.

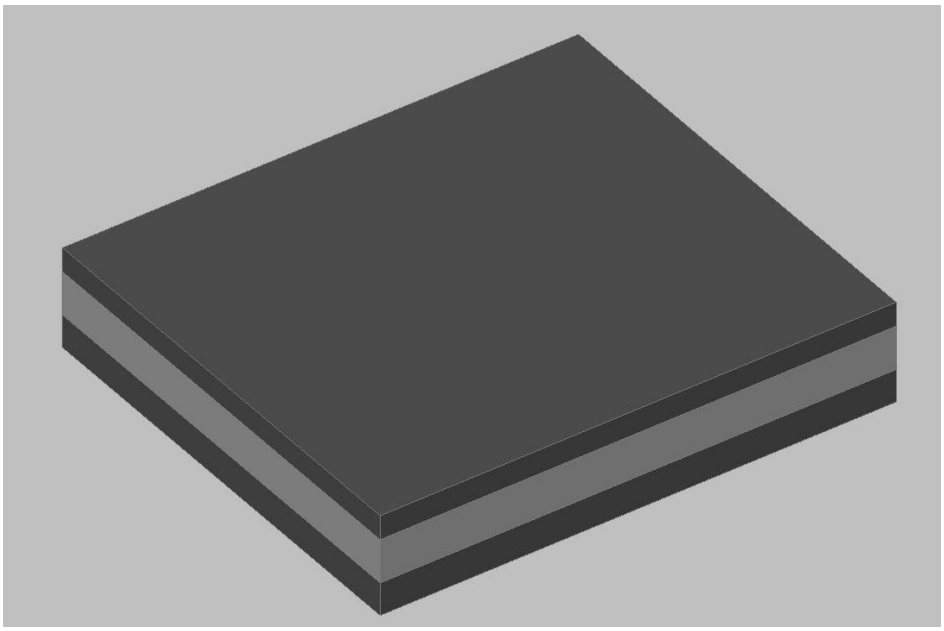

Figure 62. Chart. Three dimensional view of the Assembly Design VIII.

The material will be used to fabricate cover, protective wall and base are the same. The difference on the color is to provide a clearer view of the structure. As shown in Figure 63, AD8 has six parts:

1. Cover (MDS-filled cast nylon);
2. 3 positive (upper, copper alloy) and 3 negative (lower, copper alloy) electrodes;
3. 6 piezoceramic bars;
4. Protective wall (MDS-filled cast nylon);
5. Protective board (Light-weight PVC foam);
6. Base board (MDS-filled cast nylon).

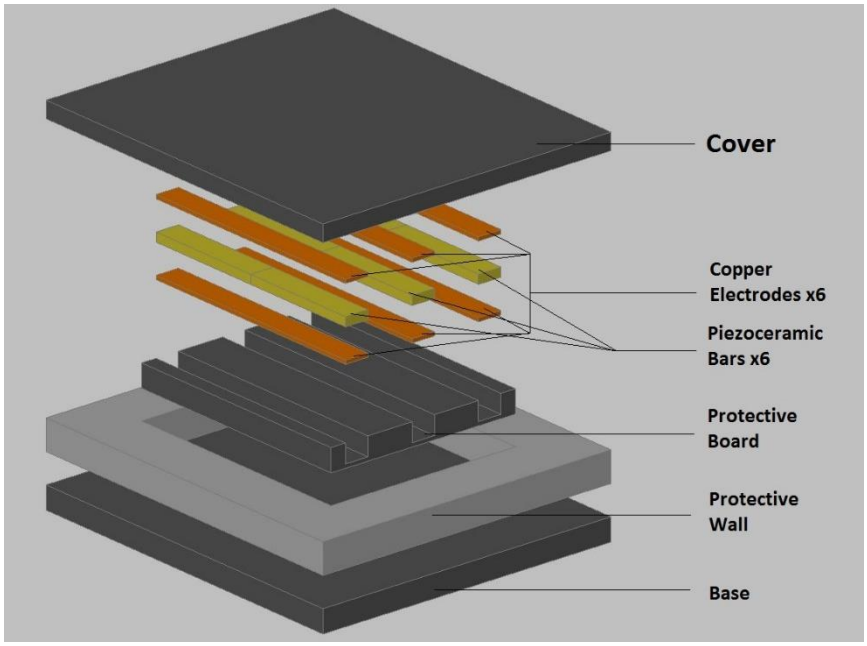

Figure 63. Chart. Three dimensional view of the Assembly Design VI (disassembled).

To apply the load uniformly and fix its position tightly, the cover will be specially fabricated as in the sketch below.

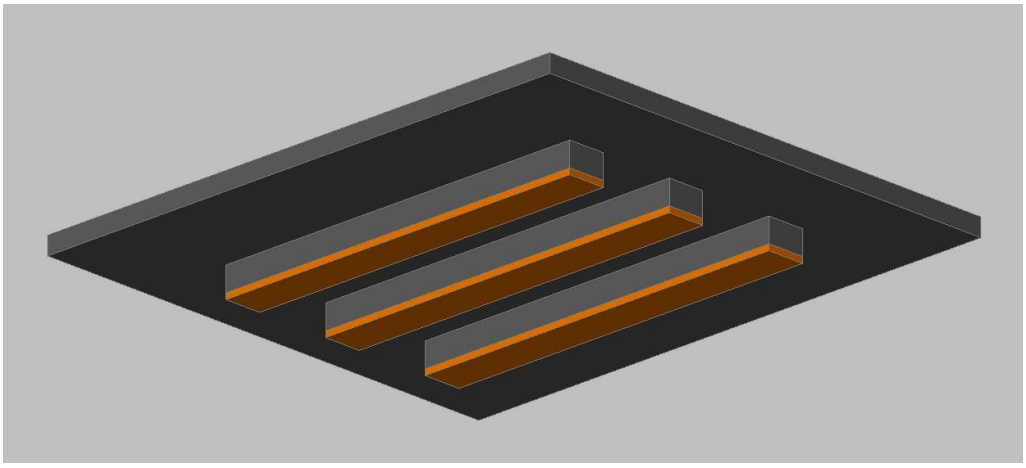

Figure 64. Chart. Three dimensional view of the cover in AD8 with positive electrodes attached.

3.10 Assembly Design IX (AD9)

The testing results indicates that the wandering of the vehicles will result in a big difference of the output power. To have a stable power output, another longer protective package was designed (Assembly Design IX, AD9). The length is about two times of previous design (547mm). The width and the thickness of the package remain the same. With this lengthened design, more piezoceramic disks are incorporated to fabricate one harvester. There will be two different stacking methods of piezoceramic disks to compare. 0.9-inch-thick piezoceramic disk with 0.8 inch of diameter will be put in the first harvester. Stack contains three piezoceramic disks with 0.3 inch of thickness and 0.8 inch of diameter will be used in another harvester. Figure 65 is the 3D illustration of AD9.

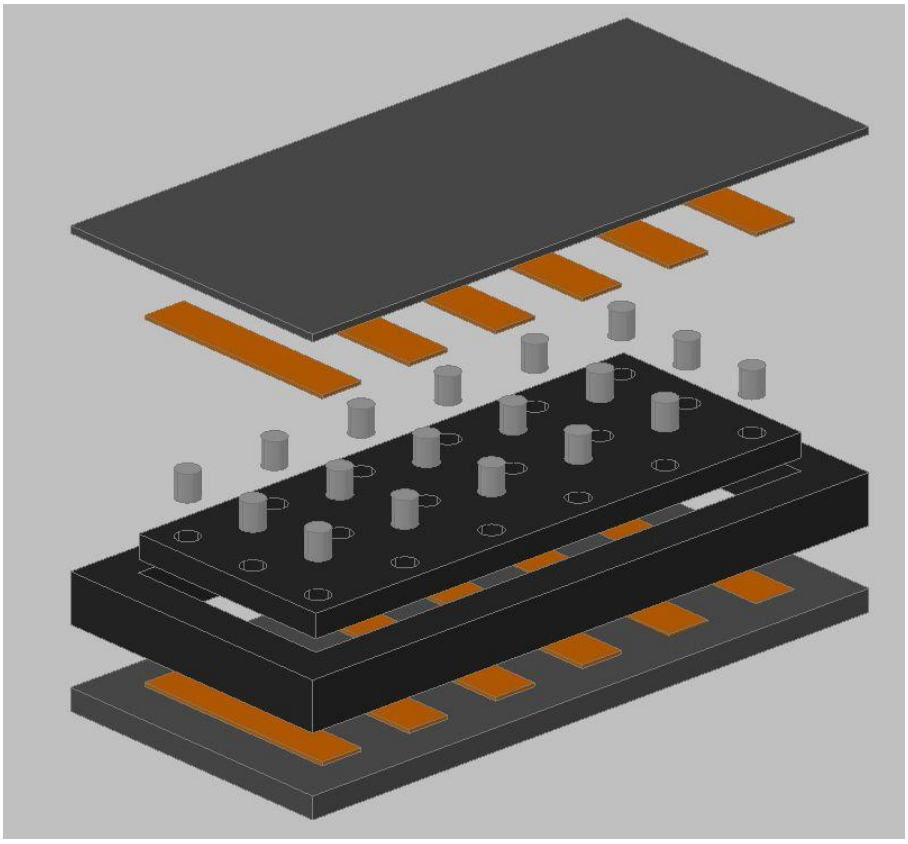

Figure 65. Chart. Three dimensional view of the Assembly Design IX.

The difference on the color is to provide a clearer view of the structure. Expect the length of the harvesters and the number of the piezoceramic disks, the design is the same as in AD7. The fabricated energy harvester is shown in Figure 66.

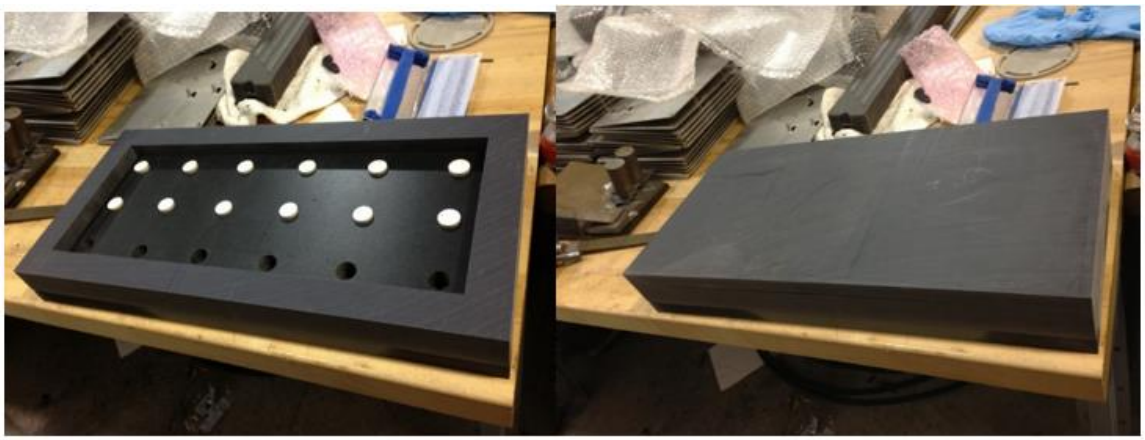

Figure 66. Photo. Energy harvester fabricated following AD9.

4 Preliminary Tests

4.1 Laboratory tests of stack of piezoceramic-disk stacks

To understand the basic mechanism of the power generation of piezoelectric material, simple tests are performed on three stacks of piezoceramic disks. The specimen used to perform the tests are supplied by Shandong Zibo Piezoceramic Ltd. Co. Three specimens have been prepared as single-layer, triple-layer and five-layer stack of disks. Each specimen has copper electrodes attached and conductive wire is connected with the electrodes. Insulating tape is used to cover the specimen. The figures below shows the specimen and the accessories.

Figure 67. Photo. Piezoceramic disk specimens for simple preliminary tests (single-layer, tripple-layer and five-layers, from left to right).

Figure 68. Photo. Copper electrodes.

A customized testing frame is used perform the test. The frame consists of an electric shaker, a force sensor, a voltage meter and a steel stabilizer. It was manufactured collaborating with the Department of Mechanical Engineering of Virginia Tech. The

figure below depicts the setup of the testing frame. The specimen is placed above a force meter and connected to a loading resistance. The force meter is set about the electric shaker and the specimen and meter is sandwiched between the steel stabilizer and the shaker. The testing data is collected by one computer connected to the meters using Lab Master software.

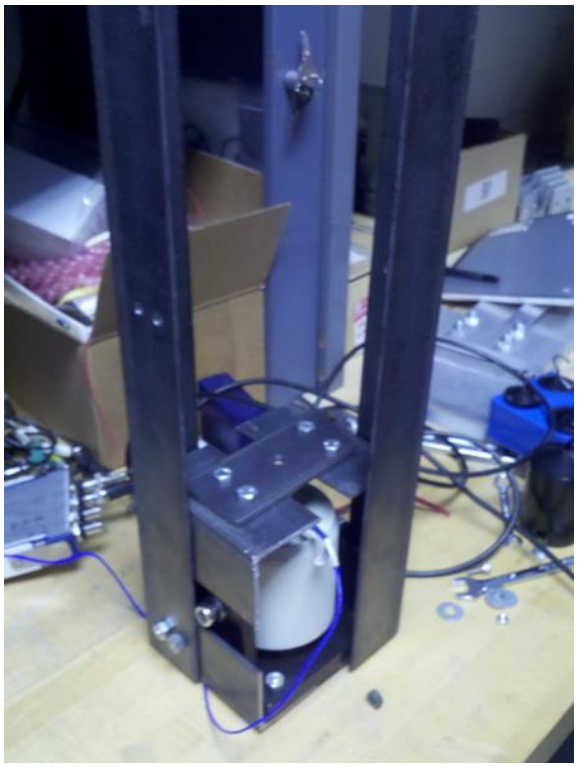

Figure 69. Photo. The schematic of the setup of the testing frame.

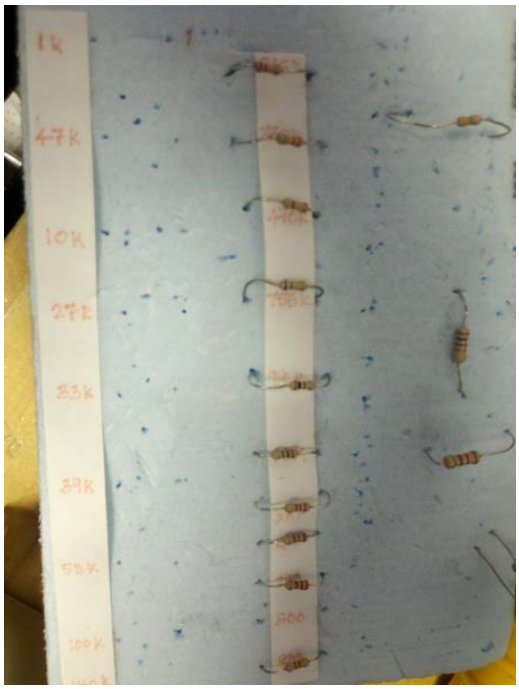

Figure 70. Photo. Loading resistors used during the tests.

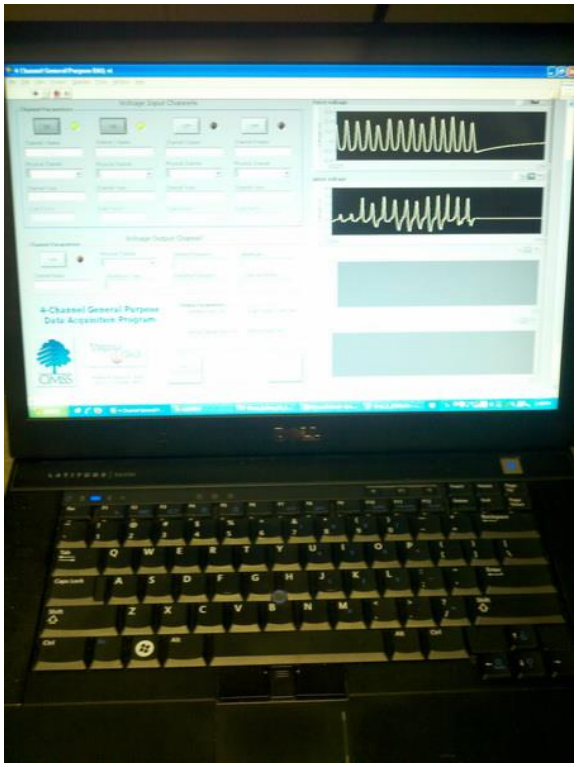

Figure 71. Photo. Laptop and software interface for data collection.

The objective of the pretests is to have a basic understanding about the testing procedure and requirement of piezoelectric energy harvesters. The stabilizer is not optimized and the stress is not evenly distributed on the surface of the specimen. The power output is relatively low due to the non-evenly distributed stress.

The voltage output data of the three specimens under cyclic loading are collected by applying different loading resistance. The cyclic force data is recorded using the Model 208C02 force sensor supplied by PCB Piezotronics as the voltage signal. Every 1 V of voltage signal can be converted into 90N of stress.

In the data analysis, power / force ratio is calculated from the output voltage by the following equation. The output performance of three generators is evaluated by comparing the P / F.

$$\frac{P}{F} = \left(\frac{\int V^2}{tR_l}\right) \Big/ \left(\frac{\int F}{t}\right) = \frac{\int V^2}{R_l \times \int F}$$

Figure 72. Equation. Power/force ratio equation for the preliminary tests.

Since piezoceramic disks are parallel connected, the loading resistance will be different when the system reaches the maximum power output. R_{lmax} is defined as the loading resistance when the power / force ratio of the generator is maximum. Theoretically, the R_{lmax} of the single-piece generator will be the greatest one among the three generators and

the R_{lmax} of the five pieces will be the lowest. The power/force ratio of five-piece generator will have the best power output performance and for single-piece generator it should be the smallest. The following figures are showing the plots of Power / Force versus loading resistance of three specimens. The maximum P/F of single-piece generator is about $1x10^{-9}$ watts/N. The R_{lmax} of the single-piece generator is not shown at Figure 73 because the greatest resistance we have, which is 2150 kΩ, is not enough. It should occur around 2500 kΩ from the theoretical calculation. As estimated, the R_{lmax} of single-piece generator is the largest one. The maximum P/F of triple-piece generator is about $3*10^{-9}$ watts/N, the R_{lmax} is about 1350 kΩ. The maximum P/F of five-piece generator is about $8*10^{-9}$ watts/N, its R_{lmax} is about 1250 kΩ. The testing result matchesthe theoretical estimation, the R_{lmax} for single-piece generator is greatest and the Power / Force ratio for the five-piece generator is the largest.

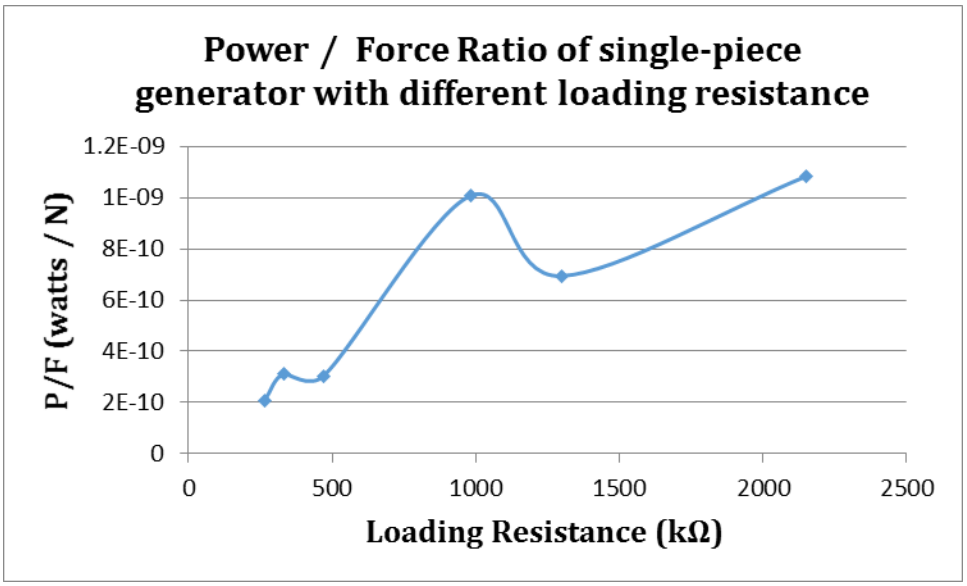

Figure 73. Chart. The plot of Power / Force Ratio of single-layer generator with different loading resistance.

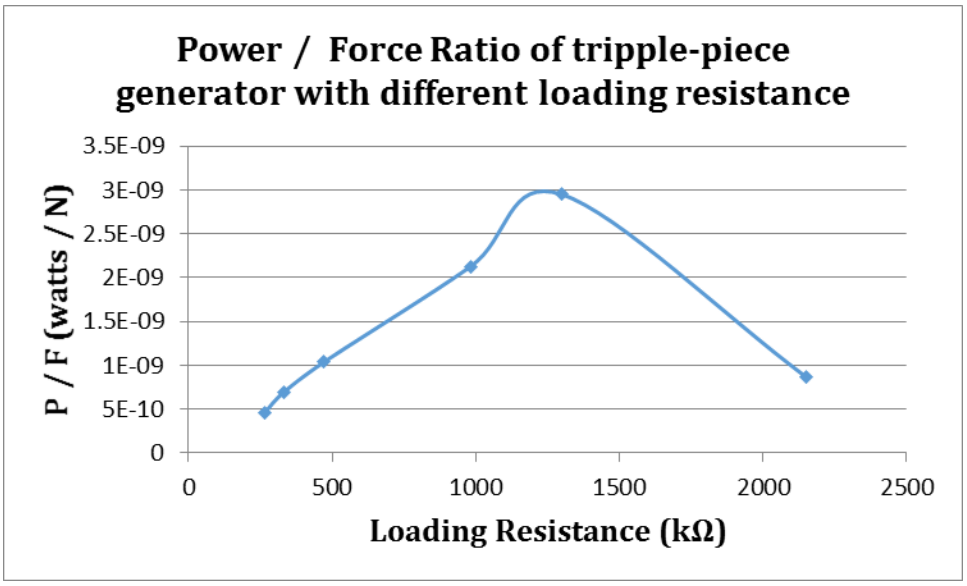

Figure 74. Chart. The plot of Power / Force Ratio of three-layered stack with different loading resistance.

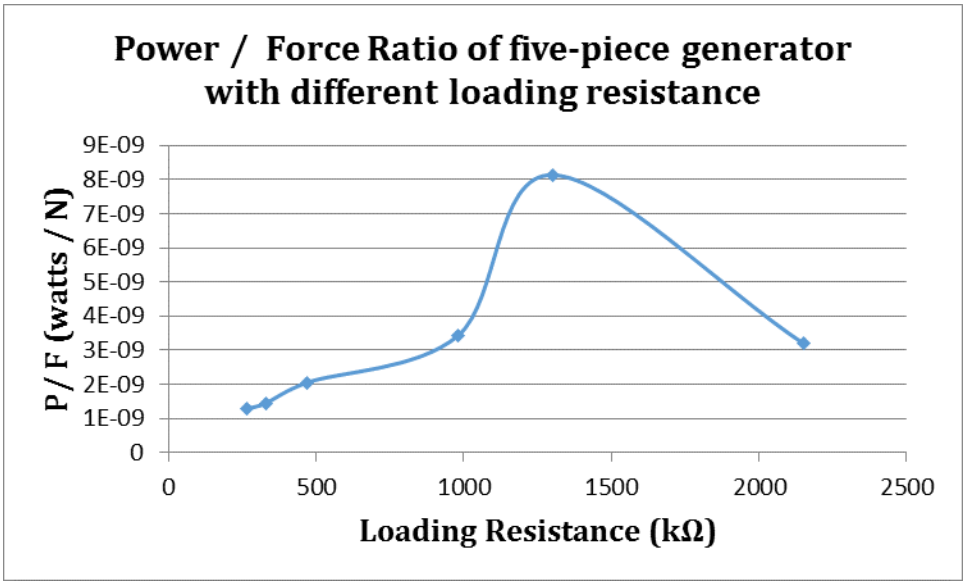

Figure 75. Chart. The plot of Power / Force Ratio of five-layered stack with different loading resistance.

4.2 Laboratory tests of AD1 harvester

The energy harvester fabricated following AD1 is tested under a Model Mobile Loading Simulator (MMLS). It can apply cyclic loading onto the specimen installed in the testing frame by three wheels. The wheel speed ranges from 0 to 12 km/hr (0 to 50Hz). By putting the energy harvester in between asphalt slabs provides very similar loading condition of real pavement under real traffic. Figure 76 is a photo of the MMLS used to perform most of the laboratory tests.

Figure 76. Photo. Model Mobile Loading Simulator

The current and voltage output from the energy harvester are measured using a laptop and a digital mutimeter manufactured by National Instrument. The measured data are analyzed to obtain the power output. Figure 77 shows the testing results of AD1 harvester with different wheel speeds and different resistors. The power output increases by increasing the electrical resistance of the resistor and the testing speed. The power output should reach a maximum when the loading electrical resistance equals to the equivalent resistance of the harvester (470k).

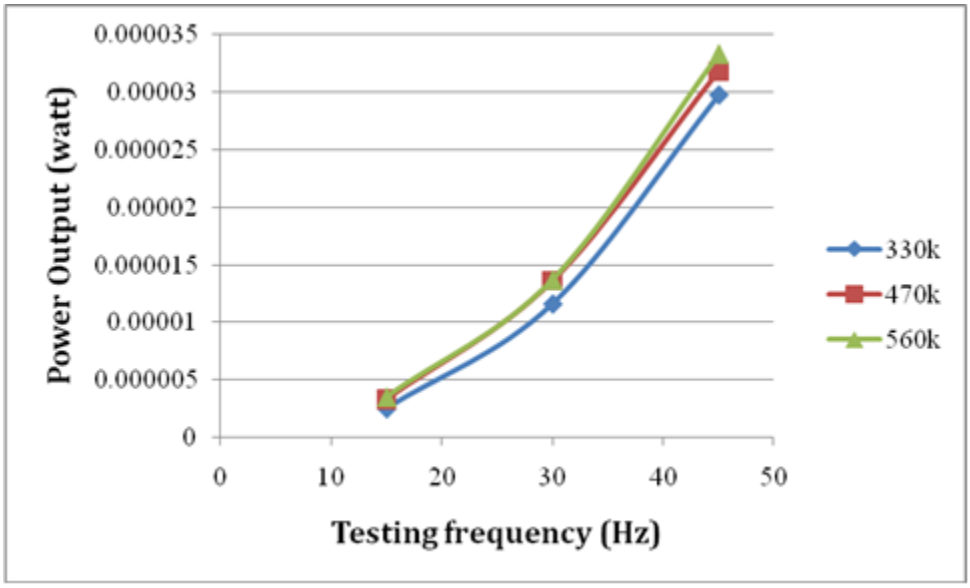

Figure 77. Chart. Power output of the AD1 harvester.

4.3 Laboratory Tests of AD2 harvester

The harvester fabricated following AD2 contains 20 pieces of parallel-connected piezoceramic discs. The "body" of this harvester is made of concrete and the cover is made of aluminum. Due to voltage limitation of the measuring device the four metal strips containing five discs each were measured independently. Figure 78 to Figure 81 show the power output from each electrode of the harvester with different wheel speeds and loading resistance. As with the first device, the power output increases by increasing the wheel speed and loading resistance. The maximum power of Design 2 harvester was also not reached during testing as it will occur when the loading resistance equals to the equivalent resistance of the harvester. The total power output was calculated by adding up the power outputs of the four strips. It was 8.1×10^{-5} watts at 45 Hz of wheel speed and 560k ohms loading resistance.

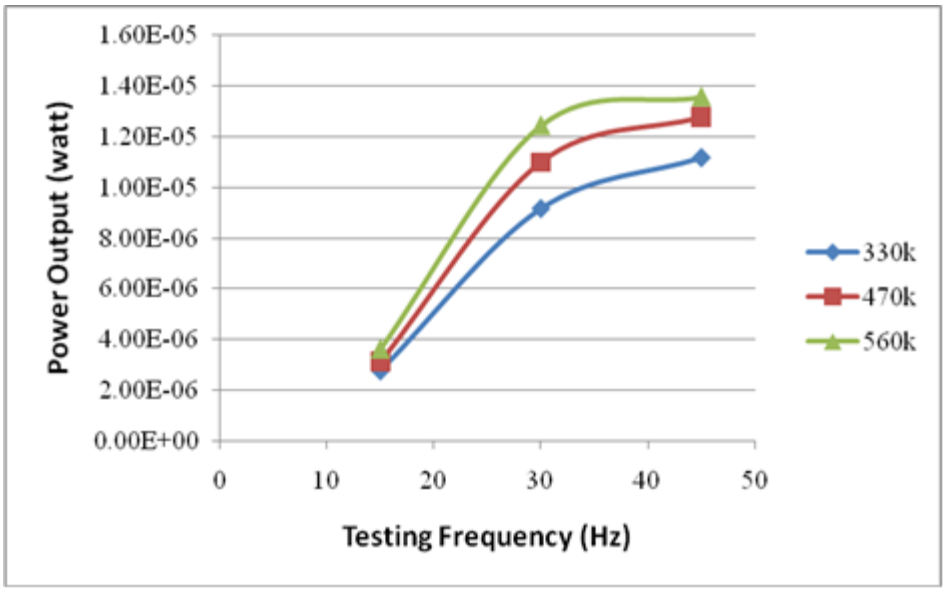

Figure 78. Chart. Power output of AD2 harvester with different wheel speeds and loading resistance (electrodes 1).

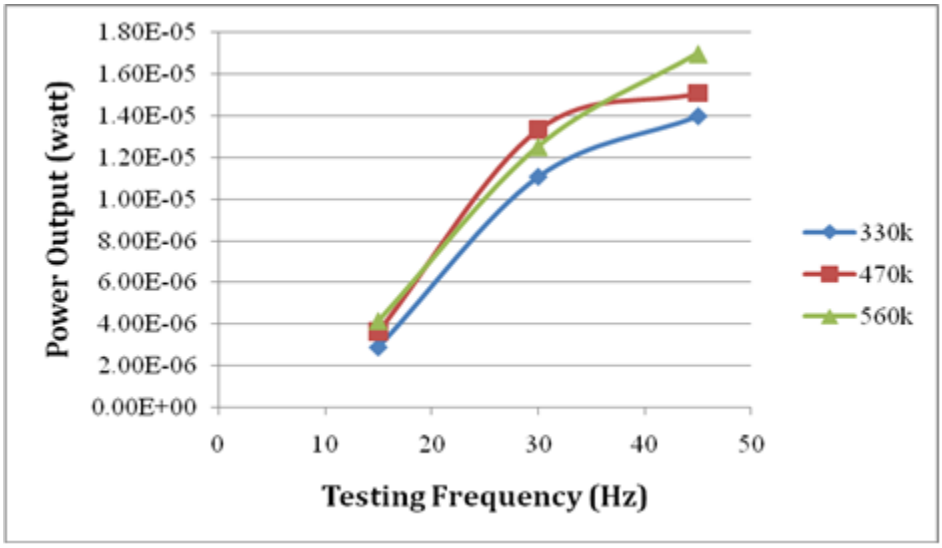

Figure 79. Chart. Power output of AD2 harvester with different wheel speeds and loading resistance (electrodes 2).

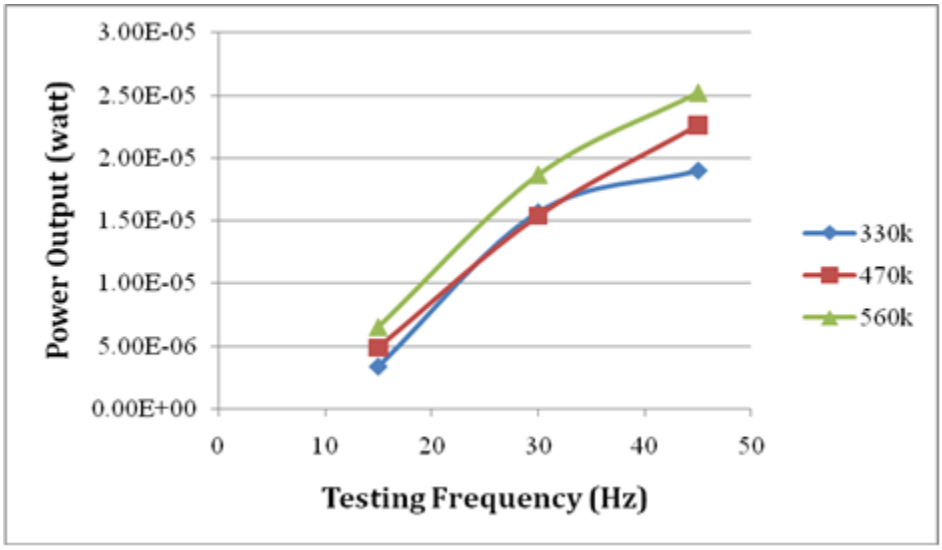

Figure 80. Chart. Power output of AD2 harvester with different wheel speeds and loading resistance (electrodes 3).

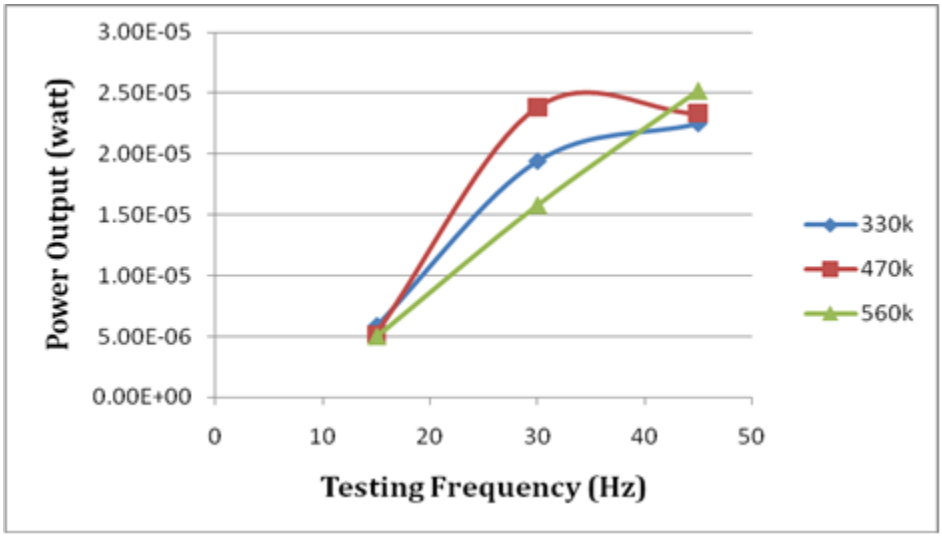

Figure 81. Chart. Power output of AD2 harvester with different wheel speeds and loading resistance (electrodes 4).

4.4 Laboratory tests of AD6 harvester

4.4.1 Voltage Output Tests

To evaluate the productivity of harvesters fabricated following AD6. The voltage output spectrums of the harvesters were measured using the MMLS. The harvesters were tested with different wheel speeds and loading resistances. Three wheel speeds used during the tests are 3.2 km/hr, 4.8 km/hr and 9.6 km/hr. Three harvesters are place in the testing. Harvester 1 (H1), Harvester 2 (H2) and Harvester 3(H3) were placed from the right to the left. Only the central rows of piezoceramic disks were tested in each energy harvester due to the lack of rectifier. The voltage output spectrums were measured with individual harvester and combined harvesters. Average power outputs were calculated based on the measured voltage spectrum.

The calculated average power outputs of the combined harvesters (H1, H2 and H3) are shown in Figure 82. Same as the previous tests, the power increases as the wheel speed increases. When 10M Ohms were applied as the resistance, the maximum total power output of 0.27 mW was observed with a wheel speed of 12 km/hr. The power outputs decrease when the loading resistance increases. The power output with 60M Ohms is the lowest one and the one with 4.7M Ohms is very similar to it. It indicates that 4.7M Ohms and 60M Ohms are very different from the equivalent resistance of the combined harvesters.

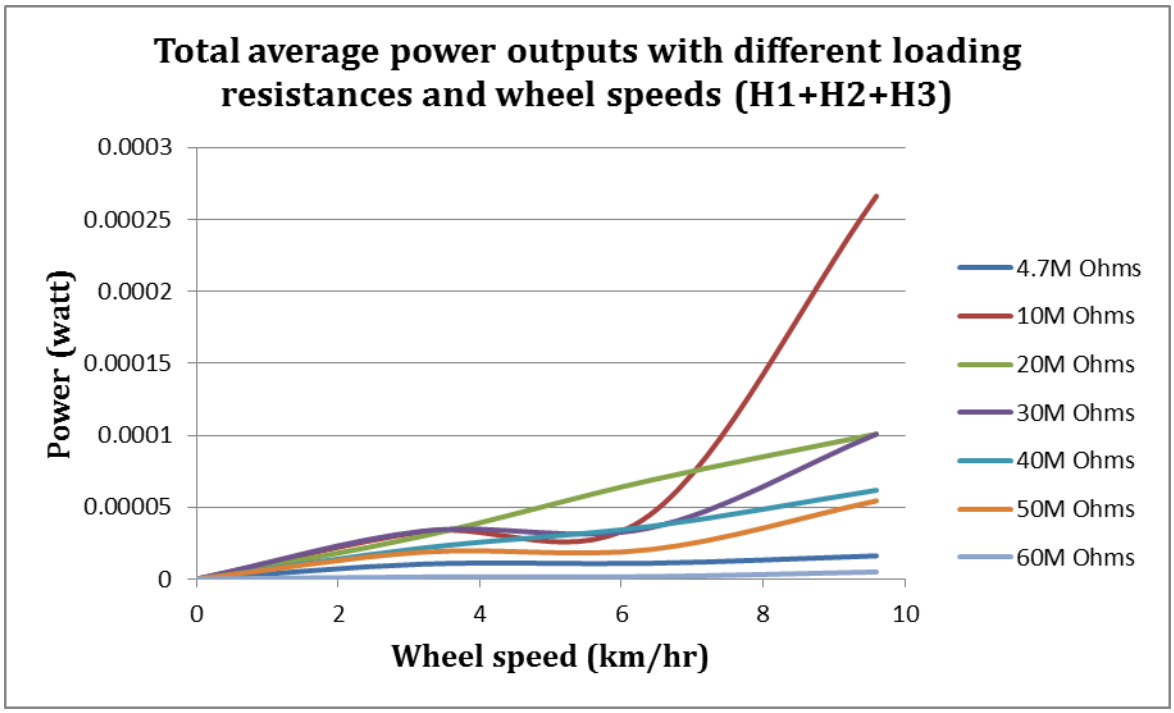

Figure 82. Chart. The total average power outputs with different loading resistances and wheel speeds.

Figure 83 shows part of the voltage output spectrum of the combined harvester with 10M Ohms resistor and 12 km/hr of wheel speed. The part of the spectrum measured in the first four seconds is included. There are about seven pulses of voltage wave in this part and each pulse has multiple peaks. These peaks are generated by individual harvesters. The negtive voltage is a result of instant releasing of loading and the positive voltage is

from the applied loading. Thus, only the positive voltage has been compared. The maximum positive voltage observed is 167 V.

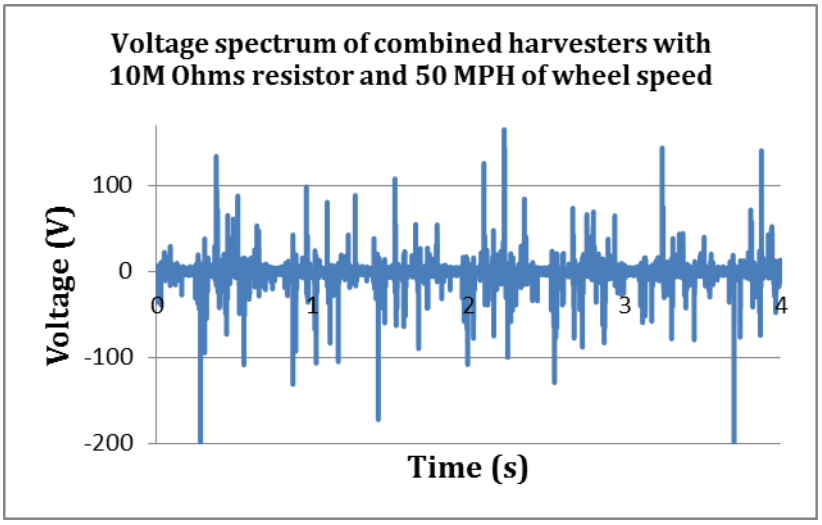

Figure 83. Chart. The Voltage output spectrum of combined harvesters with 10M Ohms loading resistance and 12 km/hr of wheel speed.

The voltage output spectrums of each harvester are presented in Figure 84, 85 and 86. The maximum positive voltages generated by each harvester (67V, 70V and 74V) are all smaller than 167 V. Thus, the maximum voltage generated by combined harvester can be explained as the result of accumulation of the voltages from individual harvesters.

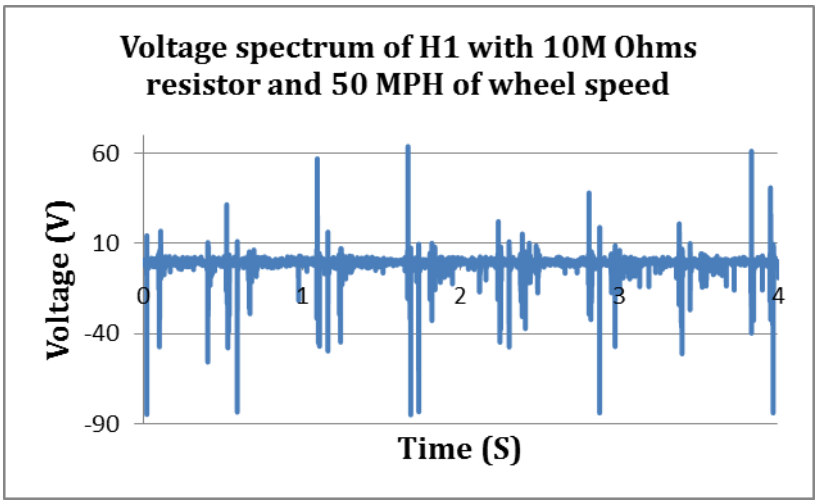

Figure 84. Chart. Voltage output spectrums of H1 with 10M Ohms resistor and 12 km/hr of wheel speed.

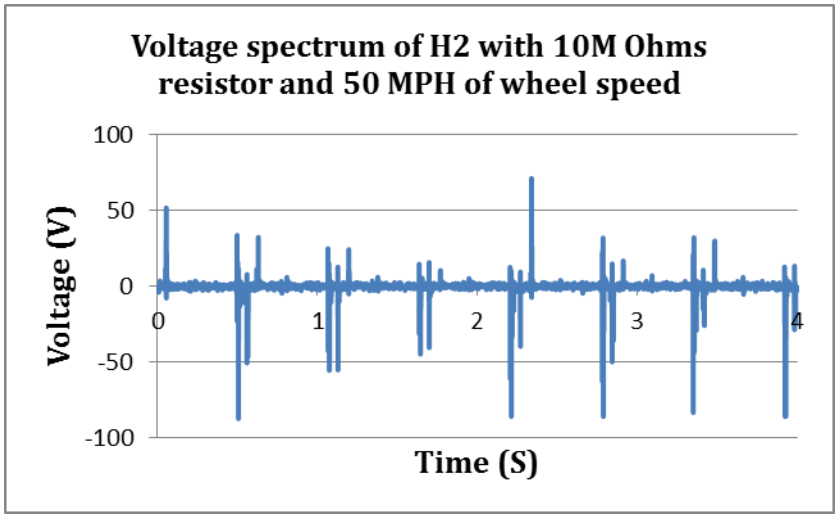

Figure 85. Chart. Voltage output spectrums of H2 with 10M Ohms resistor and 12 km/hr of wheel speed.

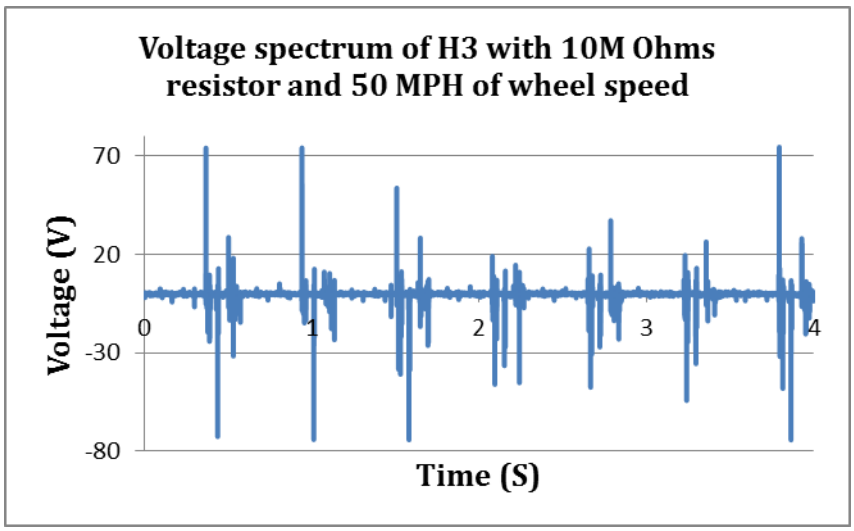

Figure 86. Chart. Voltage output spectrums of H3 with 10M Ohms resistor and 12 km/hr of wheel speed.

The average power outputs of individual harvesters and combined harvesters are listed in Table 3. The average power outputs of combined harvesters are close to the sum of the individual harvesters.

Table 3. The average power outputs (mV) of individual harvesters and combined harvesters with 12 km/hr of wheel speed and different resistance.

Resistance (MΩ)	**4.7**	**10**	**20**	**40**
H1	0.008	0.055	0.057	0.005
H2	0.013	0.038	0.012	0.028
H3	0.005	0.074	0.032	0.081
Sum	0.026	0.167	0.101	0.114
Combined	0.023	0.166	0.1	0.102

4.4.2 Capacitor Charging Tests

The charging times for a capacitor (22μF, 630V) to reach a certain voltage were measured with different loading resistance and wheel speeds. The testing results are listed in Table 4, 5 and 6.

Table 4. The charging times (s) for the capacitor to reach 30V, 60V and 100V with a wheel speed of 6 km/hr and different loading resistance.

Target Voltage	30 V	60 V	100 V
0 Ohm	80	169	304
10M Ohm	103	360	600
20M Ohm	91	221	569
40M Ohm	86	194	390
50M Ohm	85	180	366

Table 5. The charging times (s) for the capacitor to reach 30V, 60V and 100V with a wheel speed of 9 km/hr and different loading resistance

Target Voltage	30 V	60 V	100 V
0 Ohm	49	109	191
10M Ohm	50	152	600
20M Ohm	50	122	258

40M Ohm	50	115	217
50M Ohm	50	112	215

Table 6. The charging times (s) for the capacitor to reach 30V, 60V and 100V with a wheel speed of 12 km/hr and different loading resistance.

Target Voltage	**30 V**	**60 V**	**100 V**
0 Ohm	42	87	154
10M Ohm	44	112	295
20M Ohm	44	97	194
40M Ohm	44	92	176
50M Ohm	42	90	171

Shorter charging time can be obtained by using a higher wheel speed. This is in accordance with the results obtained from voltage-output tests. With the same wheel speed, the charging time to reach 30V didn't change a lot with the loading resistance. The charging time decreases as increase in the loading resistance when the target voltages are 60V and 100V. But the shortest charging time was obtained when the capacitor was connected to the voltage output without any resistor. It indicates that the equivalent resistance of the capacitor is closer to the combined harvesters than the other circuit setup under such voltage wave.

The average power was calculated from the measured charging time. Only the power obtained with a wheel speed of 12 km/hr is presented in Table 7 since it is obviously

greater than the others. The average power increases when the target voltage is greater. The maximum power of 0.143 mW is obtained from charging the capacitor to 100V with no resistor.

Table 7. The average powers (mW) calculated from the charging time with different Target Voltage, resistance and the wheel speed of 12 km/hr.

Target Voltage	**30 V**	**60 V**	**100 V**
0 Ohm	0.047	0.091	0.143
10M Ohm	0.045	0.071	0.075
20M Ohm	0.045	0.082	0.113
40M Ohm	0.045	0.086	0.125
50M Ohm	0.047	0.088	0.129

4.4.3 Durability Tests

To investigate the durability of the fabricated energy harvesters, water-proof-function tests were performed. All six fabricated harvesters were submerged in a filled water tank. The increase of their mass was measured and the inside of the harvesters was visually inspected. Table 8 lists the results of the water-proof function tests. The increase in mass of all harvesters is smaller than 20 gram. The insides of them are still dry. Thus the water-proof design is reliable.

Table 8. The results of the water-proof-function tests.

Harvesters	H1	H2	H3	H4	H5	H6
Increase of mass (g)	16.5	14.2	15.4	10.8	18.2	13.3

Damage test is performed using the MMLS. Harvesters H1, H2 and H3 have been tested for 8 hours twice with a wheel speed of 9 km/hr and the loading of 1.3 kN. There was no damage observed.

4.5 Preliminary Tests of the energy harvesters for on-site installation (AD7)

4.5.1 Simple In-field Tests

The simple field test was performed at the parking lot behind the Building II at VTTI. The objective of this test is to evaluate the environmental durability, damage resistance and power productivity of the harvesters under realistic condition. The embedded harvesters were tested with heavy vehicles. Pits were cut in the gravel and soil ground into the shape of the energy harvesters. The bottom of the pits is leveled with gravel and asphalt crack filler. As suggested by the staff from VDOT, metal plates will be added on top of the harvester. Adding metal plates can avoid the direct contacting between the tires and harvester and protect the sealing material on the cover. They were also added in this test to verify their compatibility to the harvester. In Figure 87, two harvesters were placed in the pits, with one being flush with the ground surface; the other is a little lower than the ground surface, which was then flush with the ground surface when a thin metal plate is added. All three harvesters were placed on pieces of cement slab.

Figure 87. Photo. The energy harvesters in the ground without filling the space.

The space between the harvesters and pit edges was filled with cement grout as shown in Figure 88. After the cement is set, no movement of the harvester would be allowed.

Figure 88. Photo. Filling the space with cement grout.

As shown in Figure 89, two metal plates were placed on the harvester and the top of the metal plate was flush with the ground surface.

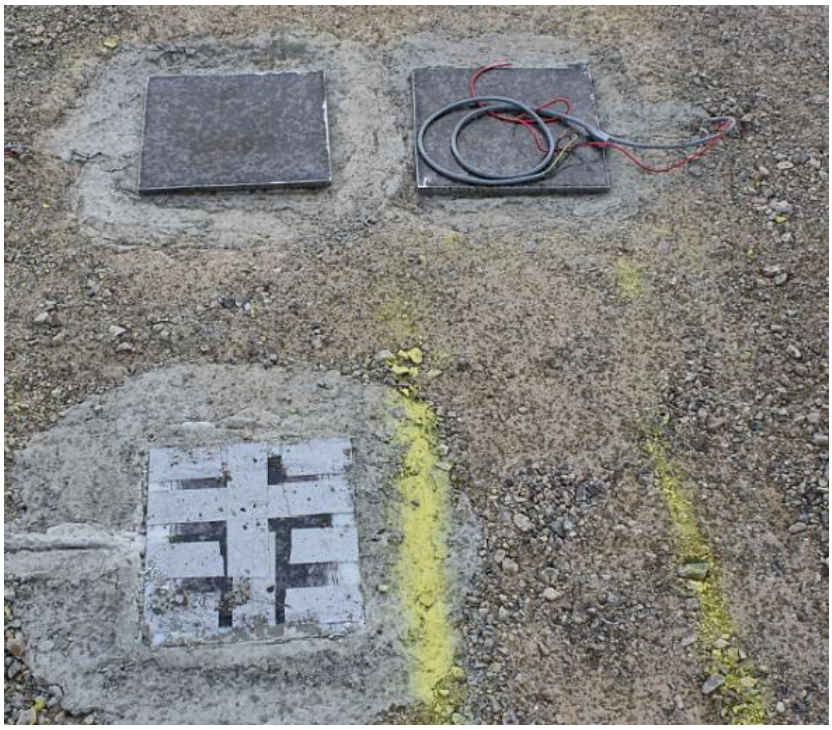

Figure 89. Photo. The energy harvester with (upper) and without (down) metal plate.

The electric performance of the embedded harvesters was tested using a pickup truck (Figure 90) and a dumper truck (Figure 91).

Figure 90. Photo. The pickup truck used to test the electric performance.

Figure 91. Photo. The dumper truck used to test the electric performance.

The average power output collected from the test using pickup truck and dumper truck is about 145 volts and 172 volts. The tire pressure of the pickup truck and the dumper truck is 79 psi and 98psi. The speed of the vehicle is about 4.8 km/hr. Since the voltage output is linearly proportional to the tire pressure, the results are reasonable. The deviation of the results might be caused by the change of the modulus of the soil after precipitation.

4.5.2 Laboratory Tests

To evaluate the electric performance of the energy harvesters, power output tests were performed with the MMLS by measuring the capacitor charging time. The capacitor was charged to 30, 60 and 90 volts under 2.7 kN of load. The wheel speed was 4.8 and 9.6 km/hr in the tests. The energy stored in the capacitor is calculated as:

$$E=1/2(CV^2)$$

Figure 92. Equation. Energy stored in a capacitor.

Where C is the capacitance and V is the voltage of the capacitor. The capacitance of the capacitor used is 22μF. Thus the average power output of the charging process can be determined by dividing energy stored in the capacitor by the time duration as:

$$P=E/t$$

Figure 93. Equation. Average power of charting a capacitor.

Three harvesters were tested to charge the capacitor with open circuit. They are harvester #1, 2 and 3. The charging time and calculated power output are shown in the following table.

Table 9. The electric performance of three energy harvesters obtained from capacitor charging time tested with MMLS.

Identity	Wheel speed (km/hr)	Time (s)	Target Voltage (V)	Average Power (mW)
#1	4.8	72.5	30	0.136551724
		156.5	60	0.253035144
		250	90	0.3564
	9.6	31	30	0.319354839
		70	60	0.565714286
		115	90	0.774782609
#2	4.8	79	30	0.125316456
		171	60	0.231578947
		290	90	0.307241379
	9.6	40	30	0.2475
		95	60	0.416842105
		145	90	0.614482759
#3	4.8	70	30	0.141428571
		155	60	0.255483871
		252.5	90	0.352871287
	9.6	36	30	0.275
		80	60	0.495
		130	90	0.685384615
Together	4.8	22.5	30	0.44
		60	60	0.66
		95	90	0.937894737
	9.6	12	30	0.825
		27	60	1.466666667
		43.5	90	2.048275862

The maximum power output of 2.04 mW was observed from three harvesters connected together at 4.8 km/hr of wheel speed when they are charging the capacitor till 90V. It equals to the sum of the power output of three individual harvesters under the same condition.

5 Interfacial circuit

Currently, three types of circuits are designed for the piezoelectric generator. The layouts of the circuits are shown in Figures 94, 95 and 96.

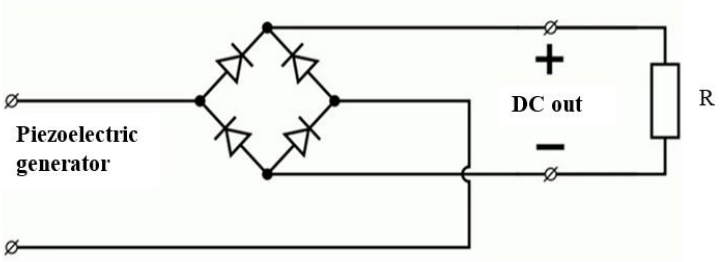

Figure 94. Chart. Rectifier-resistor circuit.

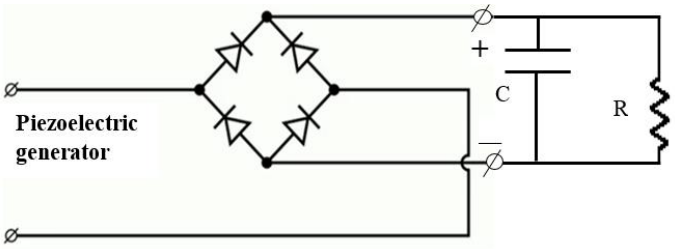

Figure 95. Chart. Rectifier- capacitor-resistor circuit.

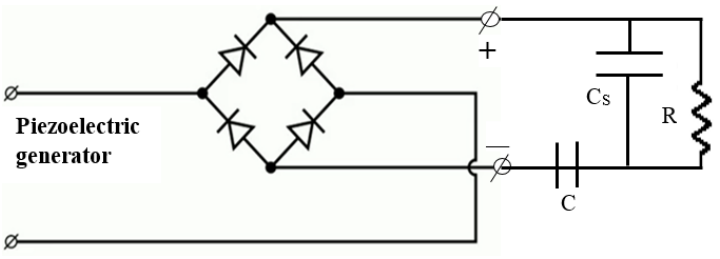

Figure 96. Chart. Circuit with Rectifier-capacitor-resistor and capacitor for energy storage.

As shown in Figure 94, the full-wave bridge rectifier, composed of diodes D1 – D4, rectifies the voltage produced by a piezoelectric generator. In Figure 94, the circuit with the voltage rectified by the bridge rectifier was directly connected with a resitor I. In Figure 95, the circuits are composed of a bridge rectifier, a capacitor and an external resistor. The capacitor is used to store electrical energy. In addition, the charging current is controlled by the resistor. In Figure 95, the circuits are composed of the resistor I, smoothing capacitor (Cs) and capacitor for storing energy. Density and stability of the charging current depend on the resistor I and the smoothing capacitor (Cs). The smoothing capacitor (Cs) convert the full-wave rippled output of the rectifier into a smooth DC output voltage. C_S should be chosen such that $C_S >> C_{generator}$ for this circuit to function correctly.

5.1 Selection of the Bridge Rectifier

The bridge rectifier is selected because full-wave rectification is needed. A bridge rectifier makes use of four diodes in a bridge arrangement, and the highest voltage generated from energy harvester embedded in the pavement is about 500 V. Thus, the

peak repetitive reverse voltage (Vrrm) must be higher than 500V; the bridge rectifier DF06M is selected for rectifying the voltage of piezoelectric generator.

5.2 Selection of the Basic Circuit

Since the one-time power output of the energy harvester is low, the rectifier-resistor-capacitor circuit is selected to be the candidate circuit design. The capacitor, C, will be charged by the voltage applied on the resistor, R. The charged capacitor could support electronic components.

5.3 Interfacial Circuit Using for On-Site Installation

In the previous power-output tests performed using MMLS, the total power output of one harvester is not, which it should be, the sum of the power outputs of each row of piezoceramic disks. By analyzing the voltage output spectrum, the reason for the decrease in total power output was found in the voltage phase interference. The voltage spectrum has sinusoidal shape and each row of the piezoceramic disk may generate positive and negative voltage. When all the electrodes are connected together to measure the total power output, the overlapped positive and negative voltage would be canceled out and the total power output would decrease. To avoid such voltage phase interference, the bridge rectifier must be connected to each row of the piezoceramic disk. The circuit layout of the connection of the rectifiers on single energy harvester is shown in Figure 97.

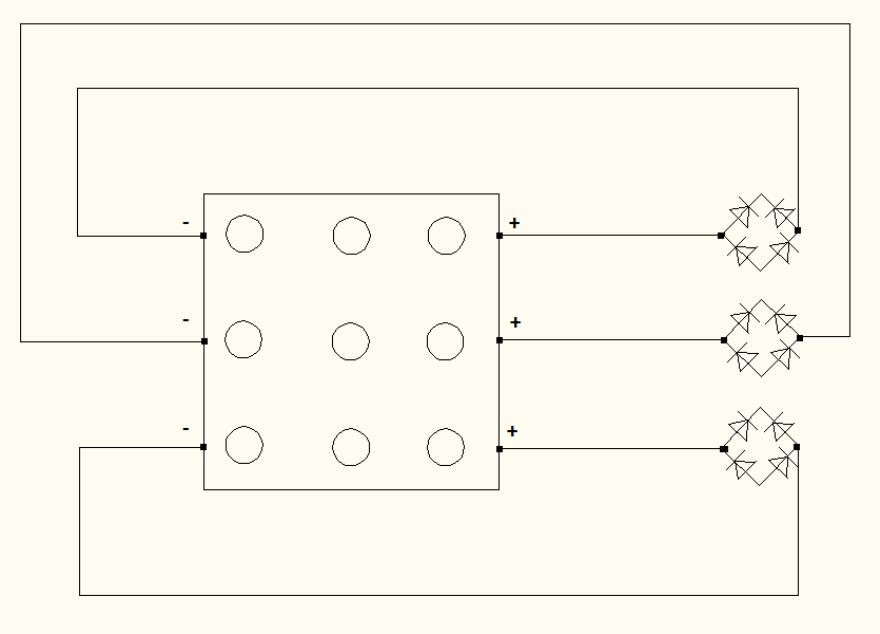

Figure 97. Chart. The layout of the circuit for the connection of the rectifiers on single energy harvester.

The bridge rectifier will convert the negative part of the voltage wave into positive and the voltage will be accumulated rather than being canceled. All of the positive ends and the negative ends of the bridge rectifiers will be connected to offer a voltage output. Figure 98 shows the circuit layout for multiple-energy-harvesters system.

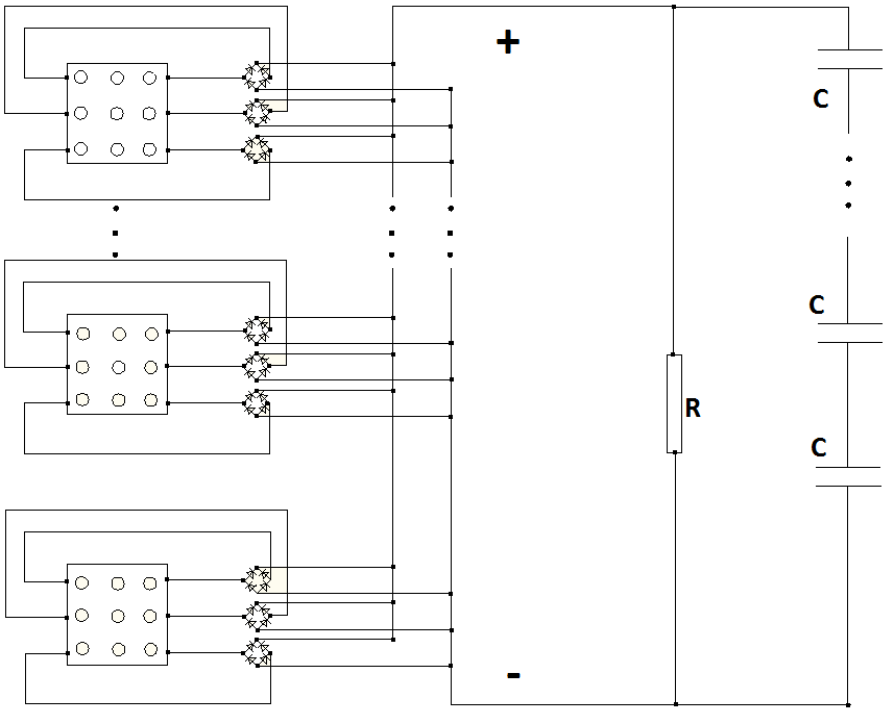

Figure 98. Chart. The circuit layout for multiple-energy-harvesters system.

The resistance of the resistor in the circuit depends on the equivalent resistance of the entire energy harvester system. The resistance of the piezoelectric material varies under the loadings with different frequencies. The resistance reduces as the frequency increases. Thus the equivalent resistance will be different when different loadings are applied. The resistor will be adjusted for the specific loading condition.

5.4 Optimization

From observation of previous tests, the discharging rate of the capacitor is too high to keep the input voltage on LED in a appropriate range. Unstable power input may cause damage to the electronics. A resistor-diode circuit is designed to optimize the input

voltage on LED or other electronics. Figure 99 shows the circuit layout. This diagram will smoothen the power input after the rectifying process.

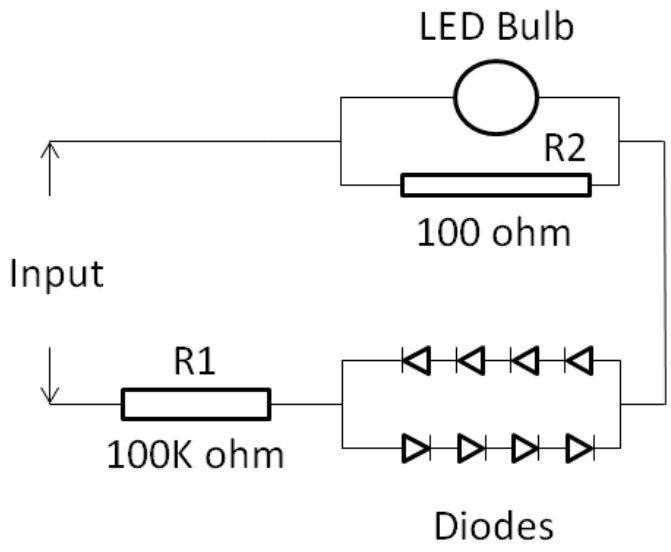

Figure 99. Chart. The circuit layout of the optimization circuit.

The resistor R1 (100k ohm) is to control the voltage on LED. It will reduce the input voltage to about 5V. The eight diodes will further reduce the voltage down to about 1.5V. The resistor R2 (100 ohm) connected in parallel with LEB is to control the current on LED bulb. We measured the input power and the power on the LED bulb. They are 0.0845mW and 0.032mW. The input power is less than the one we calculated from the capacitor charging time (average 0.68mW).

6 Installations

6.1 Installation at Route 114 (Peppers Ferry Rd.)

To investigate he performance of the protective package, one energy harvester fabricated following AD3 is installed in the pavement on Virginia State Route 114. It is a primary state highway in the state of Virginia connecting US 11 and US 460 acrossing Radford,

Christiansburg and Centerville. Figure 100 shows the location where the harvester was installed. The section to conduct installation of SR 114 is a two-lane road. It has passenger vehicles, light trucks and multi-axle trailer trucks passing every day.

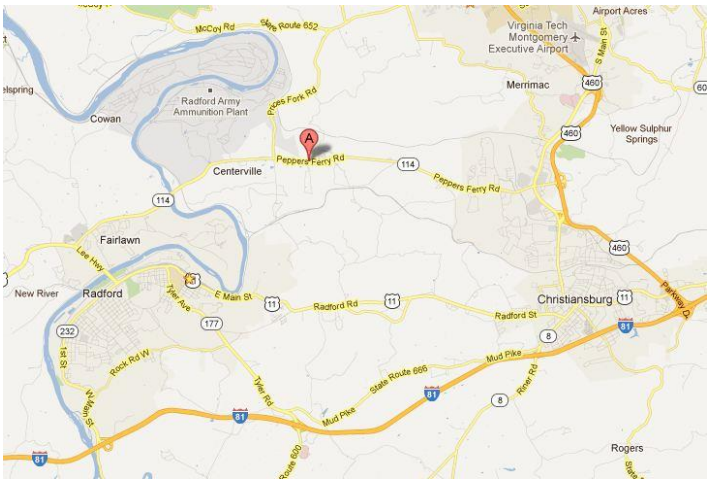

Figure 100. Chart. The location of the installation.

The exact location of the field installation is near the exit of Amber Road and marked with red in Figure 101.

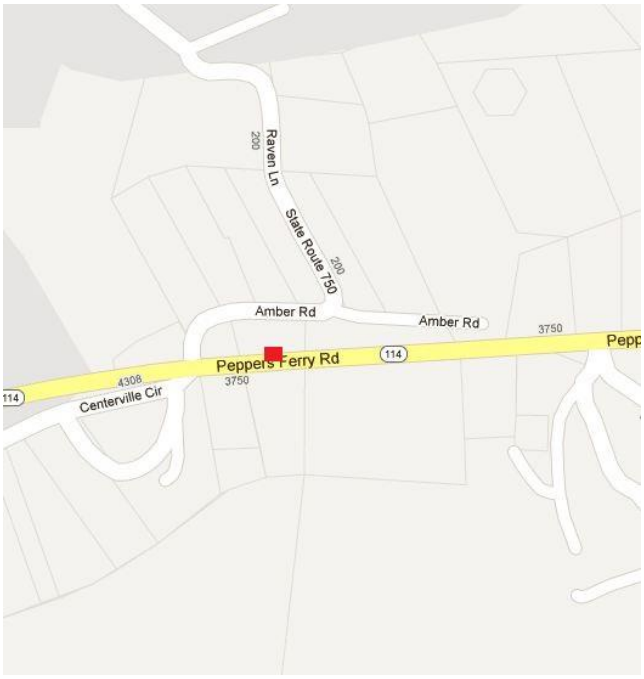

Figure 101. Chart. The exact location of the installation

6.1.1 Layout

The energy harvester was installed under a 1.5 inch asphalt overlay on the right wheel path. The layout is illustrated in Figure 102. As shown in the Figure 102, the electrical cord is connected on the energy harvester and extends to the shoulder in a pre-made channel. The cord is wrapped in a data collection box and buried in the shoulder.

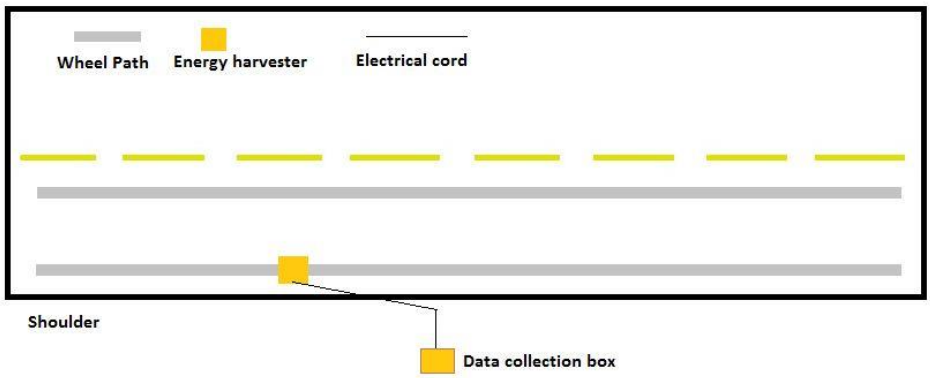

Figure 102.Chart. The layout of the energy harvester installation on Peppers Ferry Road.

6.1.2 Procedures

First, the position and the dimension of the harvester to be installed were marked on the asphalt pavement after the traffic was controlled. Figure 103 depicts the marked pavement.

Figure 103. Photo. The pavement marked with the dimension and the location of the energy harvester.

Then the marked asphalt pavement was cut using an asphalt saw and the rest of the pavement was chiseled out. Figure 104 shows the process of chiseling.

Figure 104. Photo. The scene of chieling the pavement

Before putting the energy harvester into the chiseled pit, appropriate amount of Hot Mix Asphalt (HMA) was placed at the bottom to level the surface. After placing the harvester in the pit. HMA was used to fill the rest of the space. Then the energy harvester was then covered with a layer of HMA which was slightly compacted later. The process is further illustrated in Figure 105 and 106.

Figure 105. Photo. The energy harvester being covered with HMA.

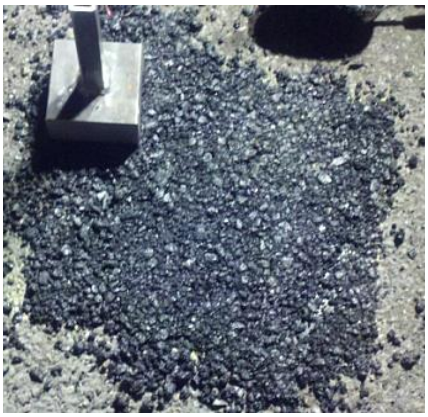

Figure 106. Photo. The energy harvester covered with slightly compacted HMA.

A channel from the harvester to the shoulder was cut using the asphalt saw to place the electrical cord. The cord was covered with a protective PVC tube on the shoulder end. Figure 107 shows the cord covered with protective tube.

Figure 107. Photo. The electrical cord covered with a PVC tube.

The 1.5-inch asphalt overlay was paved above the existing pavement lastly. Voltage output was measured after a two-day cooling phase.

6.1.3 Results

Unfortunately, the responses measured from the installed energy harvester are very weak, and the power output is very low. The compaction process may have destroyed the piezoelectric material sealed in the package.

6.1.4 Installation at Smart Road (VTTI)

Four energy harvesters fabricated following AD4 and AD5 were installed on the testing section. Smart Road at Virginia Tech Transportation Institute (VTTI). The tests can be easily conducted due to the controlled access to Smart Road.

6.1.5 Location

The Smart Road is a 3.5-kilometers road with controlled access. The location of the testing pit for installing the energy harvesters is on the shoulder which has about 10-in of asphalt surface layer. Figure 108 shows the location of the Smart Road (red part).

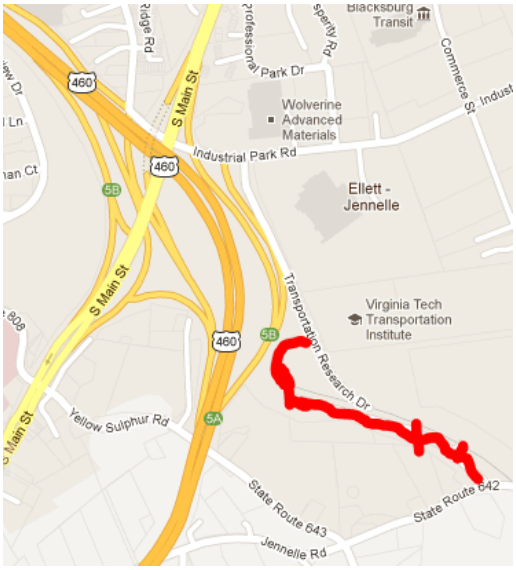

Figure 108. Chart. The location of the Smart Road (highlighted as red).

6.1.6 Layout & Procedures

Figure 109 illustrated the layout of the testing pit drawn using AutoCAD. The dimension of the testing pit is 6.5-feet long, 2-feet wide and 7-inches deep.

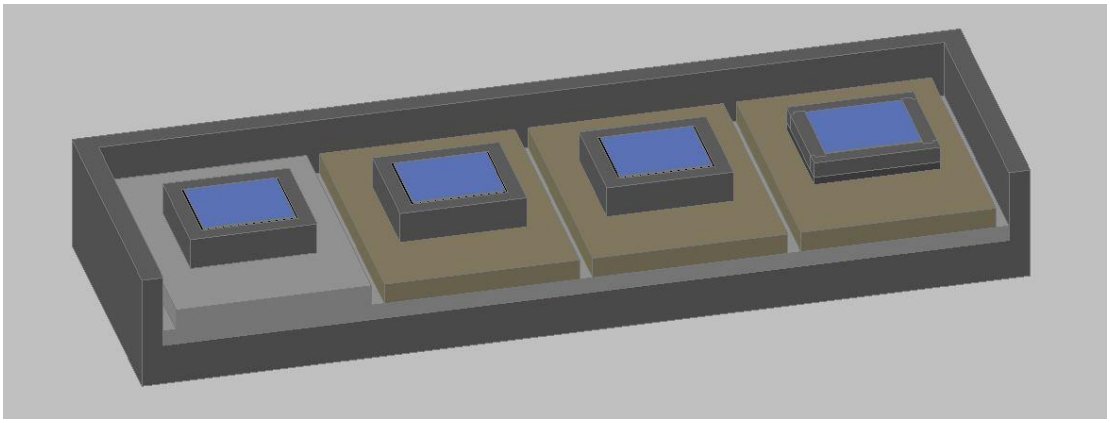

Figure 109. Chart. Three dimensional layout of the testing pit.

Figure 110 is the disintegrated 3D layout with the components labeled.

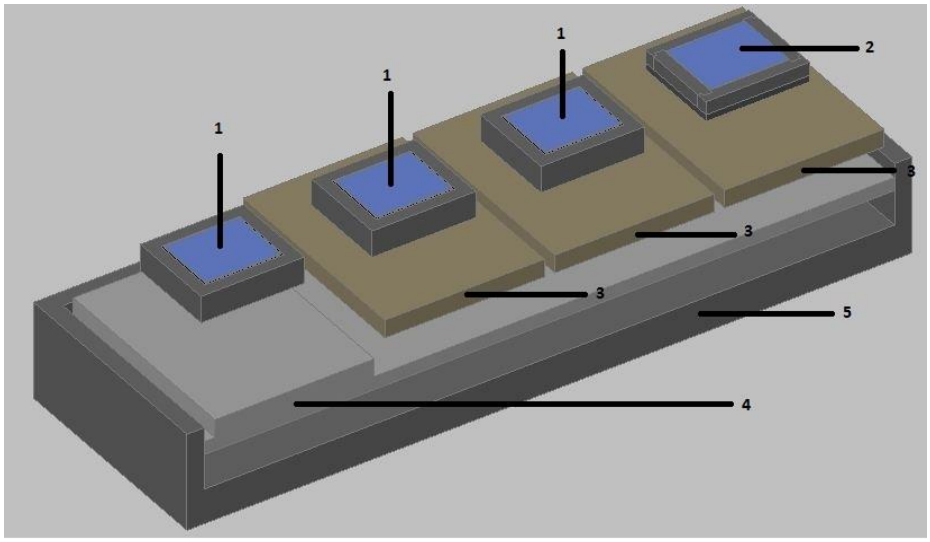

Figure 110. Chart. Three dimensional disintegrated layout of the testing pit

The components are:

1. Energy harvesters following AD4;
2. Energy harvester following AD5;
3. Pre-made cement concrete slabs;
4. Gravels;
5. Existing asphalt.

One harvester with AD4 design was placed on gravels directly to have power output comparison with the one having pre-made cement concrete slab base.

The shoulder of the Smart Road was cut to make a 6.5 ft by 2 ft testing pit. The pit was cut to 7 inches deep using an asphalt saw. 1.5 inch of gravels are paved after the pit is finished for leveling its bottom. Then three pre-made cement concrete slabs were placed

on the gravel layer to provide a stiffer base for the energy harvesters. The length, width and thickness of the pre-made slab are 24 inches, 18 inches and 2 inches respectively. Some asphalt binder is put between the slab and the harvesters to keep them from shifting during the compaction. After placing everything in the pit, the top of the four energy harvesters was one inch from the ground surface. Then the HMA was dumped into the pit and compacted. Figure 111 shows the process of installation. Figure 112 depicts the filled testing pit.

Figure 111. Photo. The actual field of the installation on the Smart Road.

Figure 112. Photo. The testing pit filled with compacted hot mix asphalt.

6.1.7 Results

The voltage output was measured after the two-day cooling phase. The test was performed by driving a four-door sedan over the compacted testing pit. Multimeter was used to measure the voltage output. The maximum voltage on day 3 was 34 volts. The maximum voltage on day 5 was 16 volts. The maximum voltage on day 10 dropped to 8 volts. The deduction of the voltage output may be caused by the dropping of temperature, or the increase of stiffness, which reduced the load transfer to the harvesters. All these tests and previous tests indicate that the harvesters must be installed with top surfaces leveled with the pavement surface.

6.2 Installation at Weight Station on I-81 Troutville

Six energy harvester fabricated following AD7 and two energy harvester from Innowattech are installed at the weigh station which is located at the exit 149 of Interstate highway I-81 at Troutville near the Roanoke city (Figure 113). There are about 3300 trucks passing the scaling system of the weigh station every day.

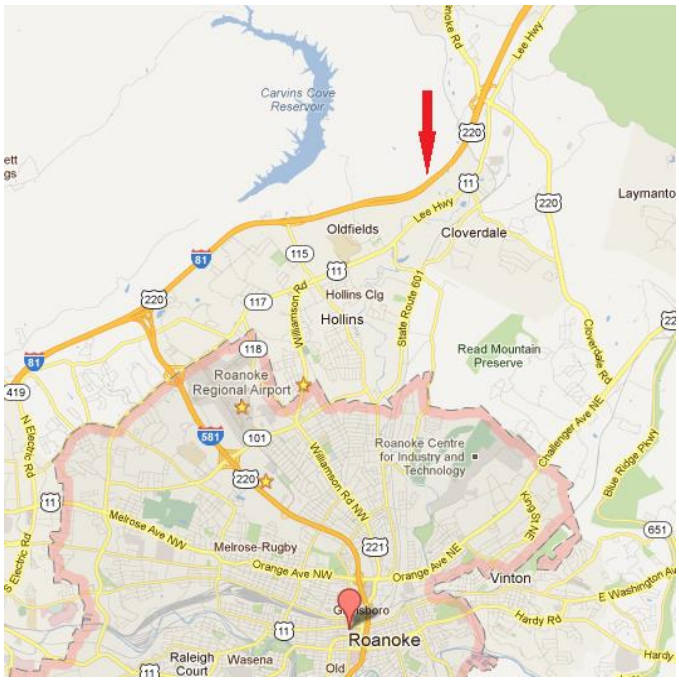

Figure 113. Chart. The location of the weigh station.

The weigh station can provide the information about the mass and axel of the passed truck. The vehicle mass is an important variable in predicting the power output. The weigh station has a one-lane entrance and a one-lane exit. Figure 114 depicts the bird-view of the weigh station. The energy harvesters will be installed in the asphalt pavement at either the entrance.

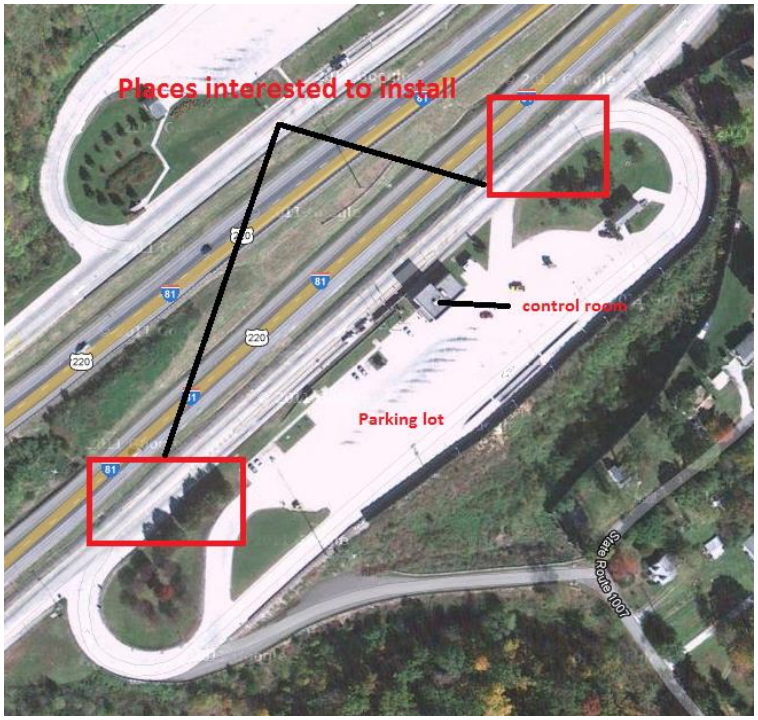

Figure 114. Photo. The bird view of the weigh station.

6.2.1 Layout and Procedures

The location selected for the actual embedment of the energy harvesting units is in the bypass lane at the Troutville weigh station as shown in Figure 115. This location was selected through coordination with VDOT and the Department of Motor Vehicles (DMV) because it offers more continuous traffic, without too much braking or stops from the trucks. This way, the shearing effect from the tires on top of the devices will be diminished.

Figure 115. Photo. Location for the installation.

The detailed operation procedures of the installation is proposed:

- Saw-cut across the lane width then excavate and remove the resulting material. 12’ L x10’ W x12” H pits is recommended for harvester to fit in.
- Prepare/level the bottom of the cut section (pits) using epoxy grout or concrete.
- Sit/Align the energy harvest units on top of the concrete layer according to the layout in Figure 116. After the first concrete layer has set, another concrete layer should be poured around them for fastening. All units should be installed flush with the second concrete layer.

- Put electrical cables through grooves cut in the concrete layer to the side of the road. Cables will be covered by epoxy before the second layer of concrete is placed.
- Provide enclosure/power supply (120V) for data loggers – coordinate with VTTI electrical engineer/electrician.

As shown in Figure 116, the blue squares represent the energy harvester developed by Virginia Tech. The orange one represents the harvester developed by Innowattech. Harvesters will be installed along the wheel path of the trucks. The relative location was determined by measuring the trace from the field. In the layout, the vehicles are supposed to travel from the left to the right.

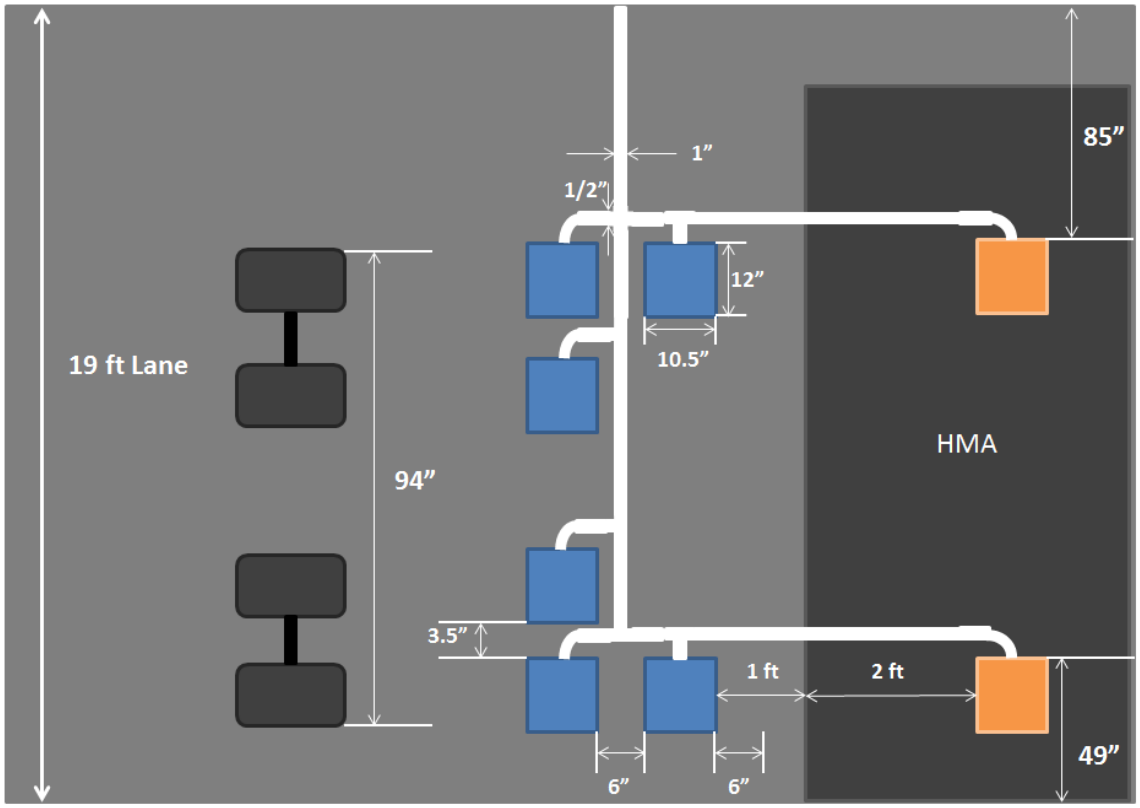

Figure 116. Chart. The layout of Trouville weigh station installation.

Figure 117 shows the cross-sectional view of the layout. The dimension of the surrounding pavement of the harvester developed by Innowattech is following their installation procedure.

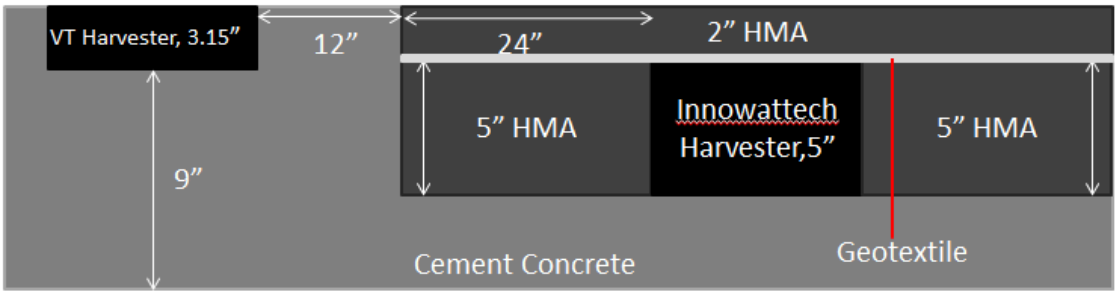

Figure 117. Chart. Cross-sectional view of the layout of Trouville weigh station installation.

The installation is following the directional layout. Firstly, pavement was marked for exact locations for all energy harvest devices in the wheel path of the bypass lane (Figure 118). A trailer truck (provided by the maintenance and design engineers) was used to mark the location for perfect alignment.

Figure 118. Photo. Marking the pavement for the alighment of the energy harvesters.

Rectangular concrete blocks were cut following the marks in the pavement using a concrete saw, at different depths, to accommodate the energy harvesting units (Figure 119).

Figure 119. Photo. Cutting holes on pavement for energy harvesters.

Then air compressed jack hammers were used to break/remove the concrete from the cuts (Figure 120).

Figure 120. Photo. Jack hammering the cut pavement.

Remaining material and the side wall was chiseled until straight walls and relatively flat bottom were obtained (Figure 121).

Figure 121. Photo. Chiseling out the remaining material and preparing the side wall and bottom.

The bottom of cut pavement section (pits) was filled and leveled with grout based on designs provided by VDOT maintenance engineers. Then the prepared bottom was allowed to set for 12 hour before the units were placed in (Figure 122).

Figure 122. Photo. Preparing the bottom of the pits.

After all the pits were prepared, the pavement was marked for the cable trench based on the installation layout (Figure 123).

Figure 123. Photo. Marking the pavement for the cable trench.

Cable trench was cut in the pavement to route the cables from the harvest devices to the side of the road (Figure 124). Cables were subsequently protected by epoxy poured into the trench to be leveled with the surface of the pavement afterwards.

Figure 124. Photo. Cables in the prepared trench.

To allow enough movement of the cover plate of the harvester, rubber membrane is torched and applied to the upper part of sides of energy harvest devices before placed in the pavement pits (Figure 125).

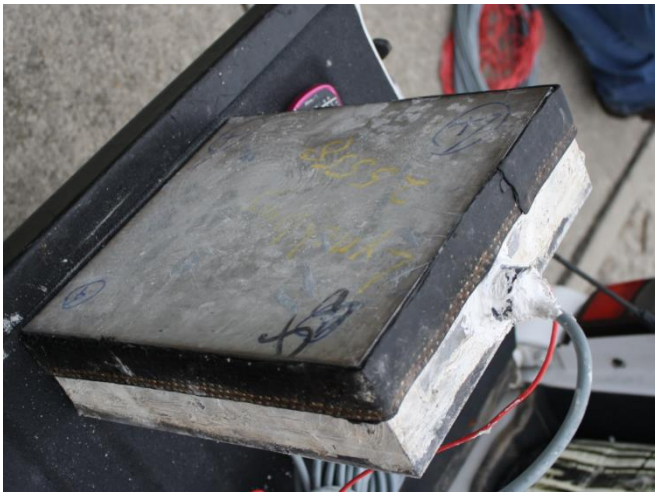

Figure 125. Photo. Wrapping the sides of energy harvester with rubber membrane.

A thin layer of epoxy (provided by the maintenance and design engineers) was applied on the prepared bottoms of the pitss to help positioning harvester (Figure 126). The harvesters were placed, seated and leveled at the bottom of pits. 2-3 inches space was allowed around the harvesters for filling the epoxy (Figure 127).

Figure 126. Photo. Applying a thin layer of epoxy in the prepared pits (to have a good bonding).

Figure 127. Photo. Placing the harvester in the prepared pits.

Epoxy was poured around the harvest devices and cables for locking in place and waterproof purposes. Strong bonding was provided together with the surrounding concrete to prevent units pumping out from the pavement. (Figure 128).

Figure 128. Photo. Pouring the epoxy in the prepared pits and cable trench.

After pouring the epoxy, a 2-in PVC conduit was used to protect all the cables coming out of the devices and then route them into an electrical weatherproof box for subsequent connection with data logging devices (Figure 129 and 130). The cables were routed following the layout as illustrated in Figure 131.

Figure 129. Photo. The protective conduit.

Figure 130.Photo. the water-proof cable box.

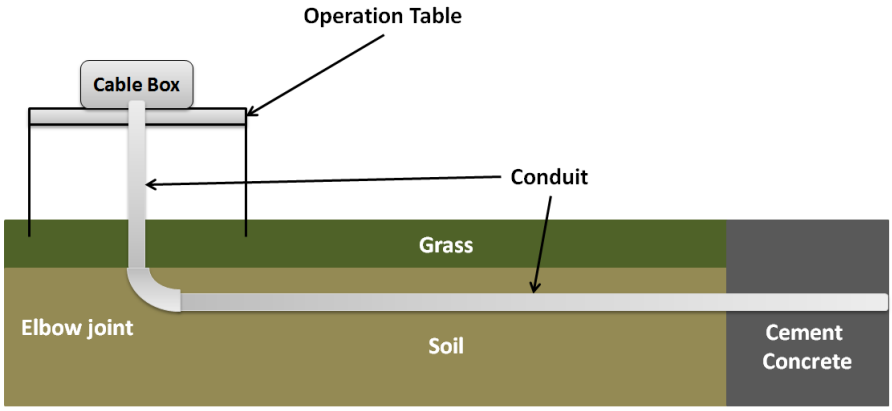

Figure 131. Chart. The layout of routing the cable through the PVC conduit.

After installation of the eight energy harvest devices in the rigid pavement is accomplished, epoxy was cast to fill the trenches to the same level with pavement surface (Figure 132).

Figure 132. Photo. Final pattern of the eight energy harvest devices installed in the wheel paths of the bypass lane.

6.2.2 Data Measurements

To monitor the electrical productivity of installed energy harvesters, the current and voltage generated from passing vehicles are periodically measured using a laptop connected digital 105ultimeter manufactured by National Instrument. About 50 measurements were taken on each harvester during every on-site evaluation. The only set with maximum electrical output voltage and current waveforms are selected to analyze the power output. Since all the voltage and current waveforms are similar, only the data measured on October 25th 2012 are shown in the figures below.

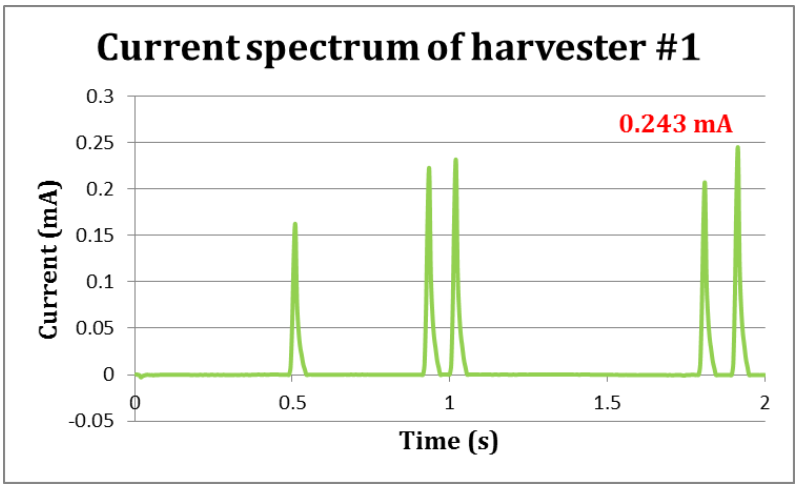

Figure 133. Chart The current spectrum of harvester #1 (measured on 10/25/2012).

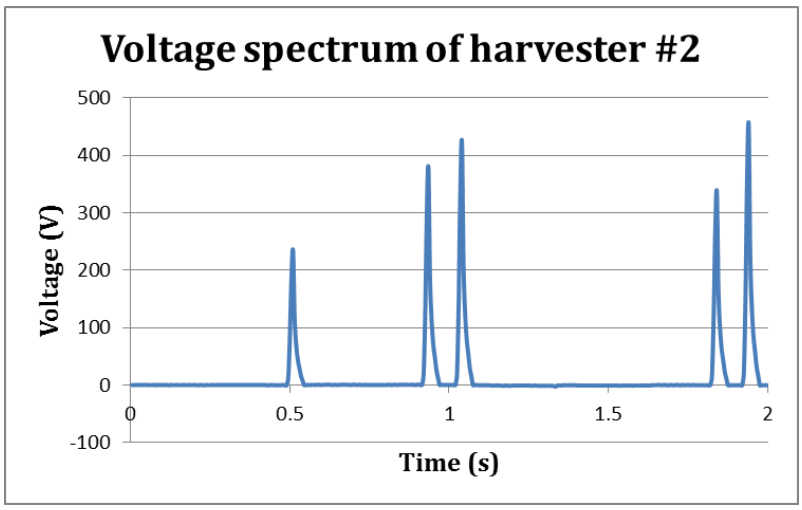

Figure 134. Chart. The voltage spectrum of harvester #1(measured on 10/25/2012).

6.2.3 Maintenance

After the energy harvesters were installed, there was no significant failure happened to the surrounding pavement. The installation of the energy harvesters did not affect the traffic flow in the weigh station. There was no fund spent on maintenance of the installed energy harvesters.

7 Electrical performance of installed harvester

7.1 Power Output Waveforms

The power waveforms of each energy harvester are calculated from correspondingly measured current and voltage. Total energy is obtained by integrating the power waveform over the time interval that the vehicle was passing the harvester. The average power is calculated by dividing the total energy with the time interval, which is about 1.5 second. Each set of power output waveforms in this section were analyzed from the data measured from more than 400 vehicles.

7.1.1 Power Spectrums (10/25/2012)

The power output waveforms analyzed from the data measured on Oct 25th 2012 are presented in the following figure.

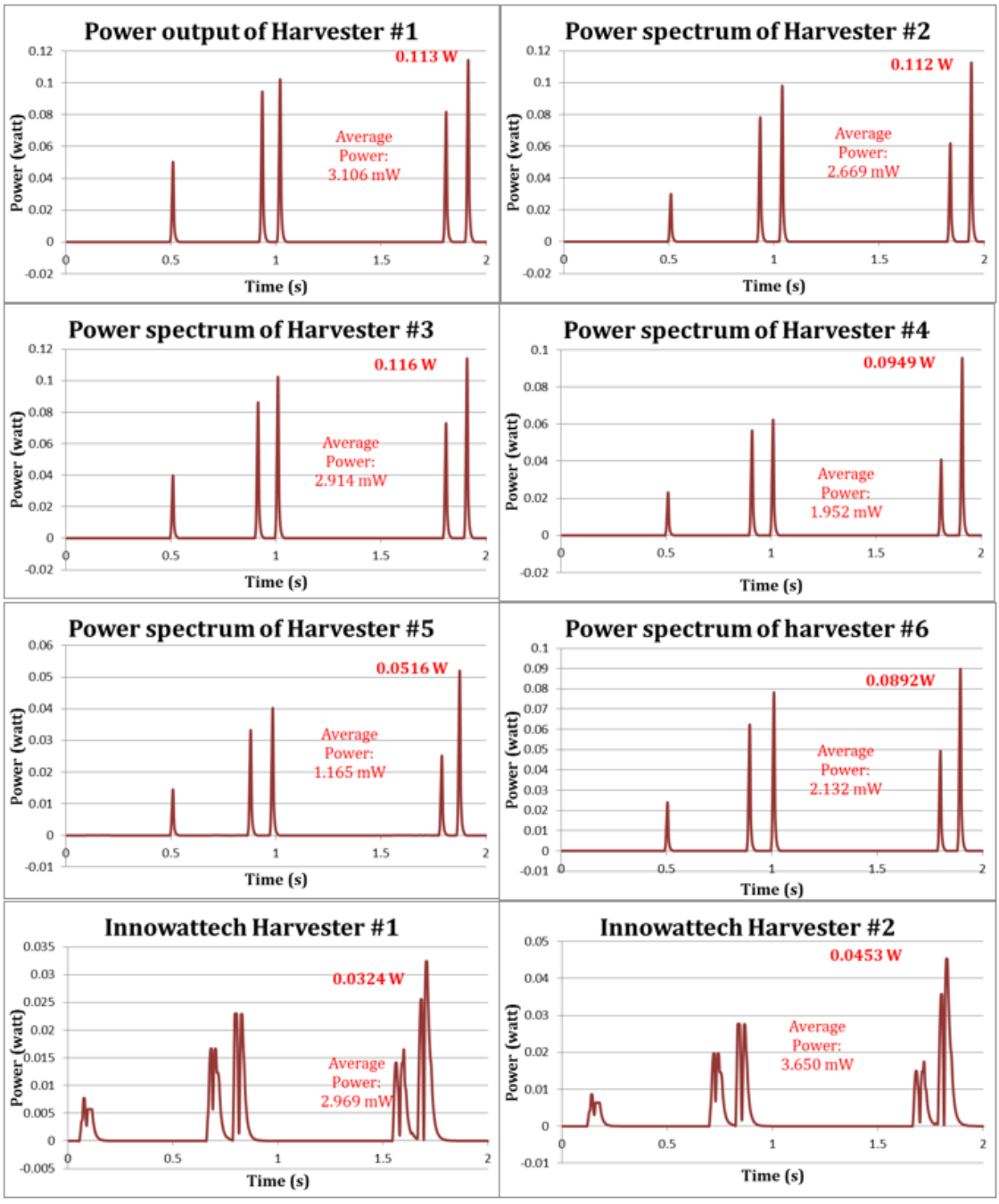

Figure 135. Chart. The power spectrums of the installed energy harvester calculated from the data collected on 10/25/2012 (VT and Innowattech).

7.1.2 Power Spectrums (11/30/2012)

The power output waveforms analyzed from the data measured on Nov 30th 2012 are presented in the following figure.

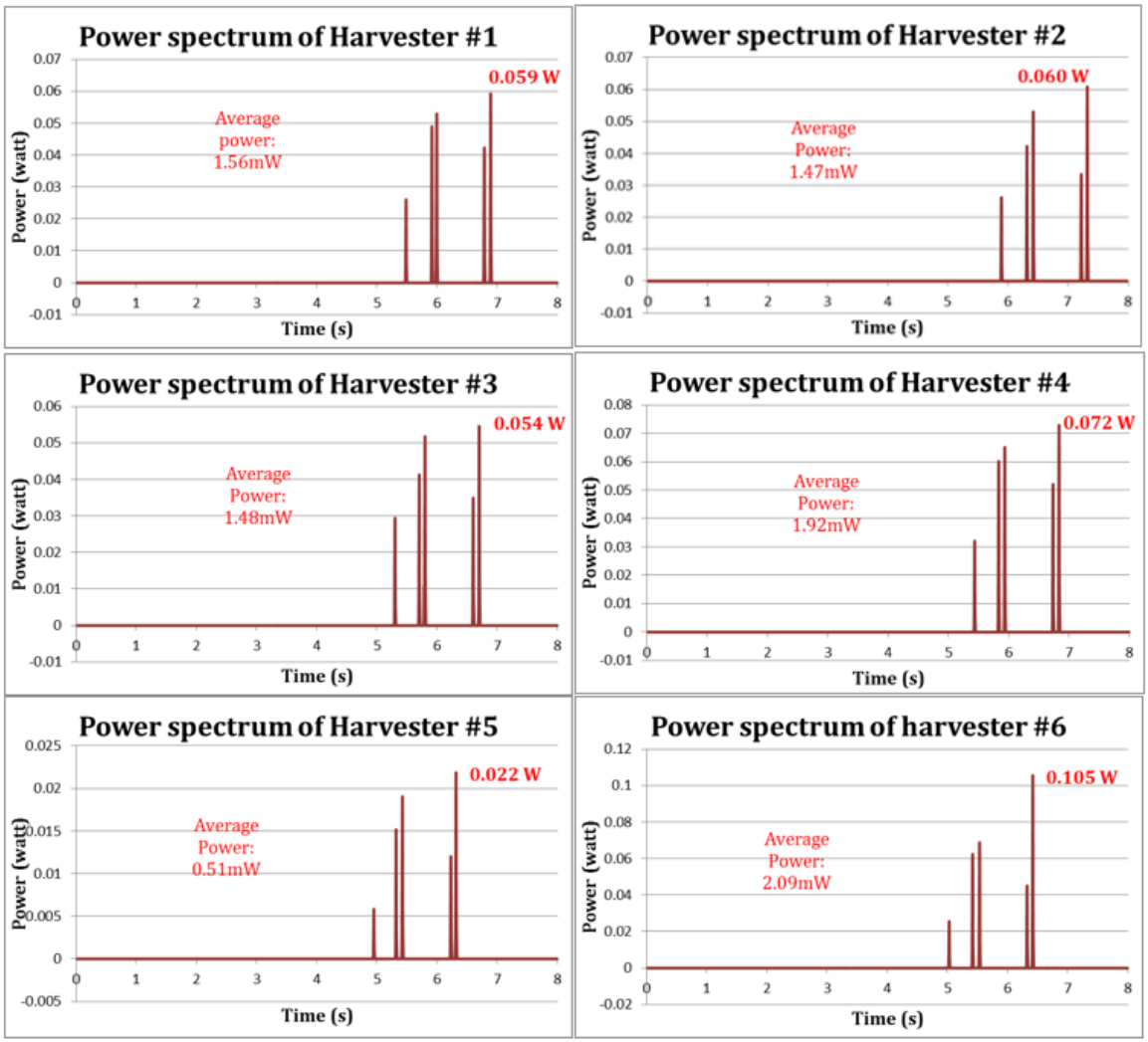

Figure 136. Chart. The power spectrums of the installed energy harvester calculated from the data collected on 11/30/2012 (VT).

7.1.3 Power Spectrums (01/31/2013)

Figure 137 shows the calculated power output spectrums of energy harvesters only from Virginia Tech.

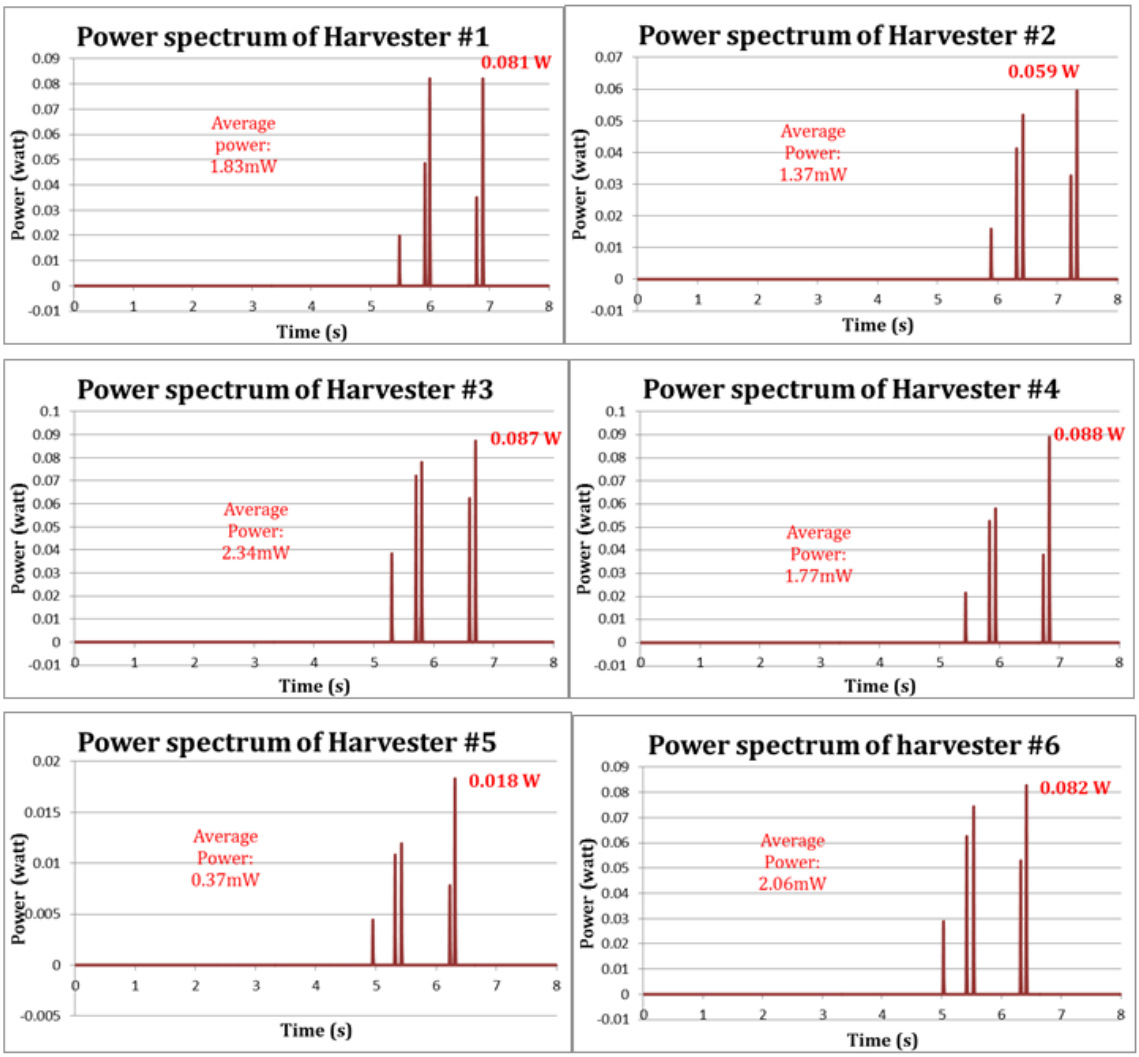

Figure 137. Chart. The power spectrums of the installed energy harvester calculated from the data collected on 01/31/2013 (VT).

7.1.4 Power Spectrums (02/14/2013)

Figure 138 shows the calculated power output spectrums of energy harvesters from Virginia Tech and Innowattech.

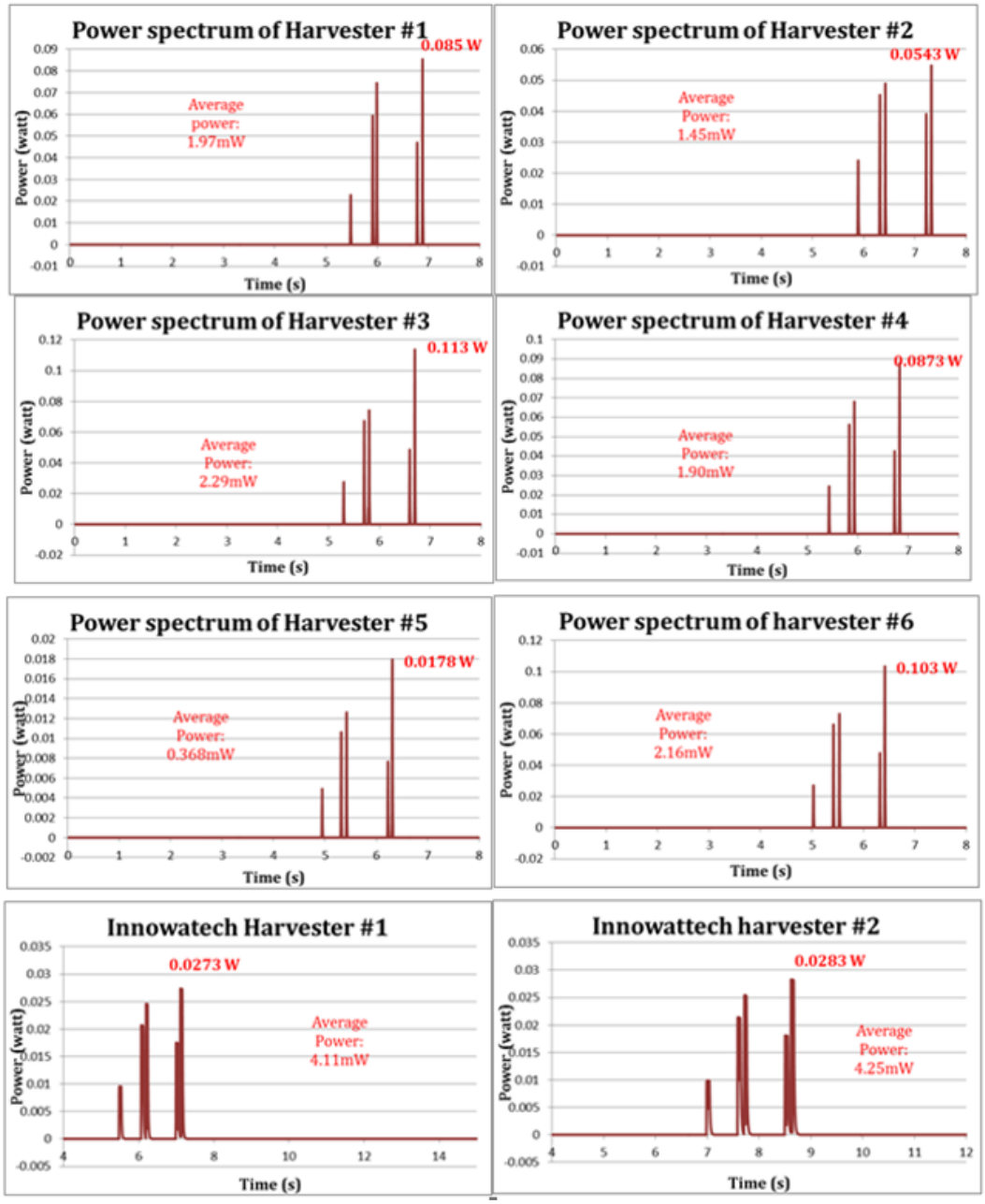

Figure 138. Chart. The power spectrums of the installed energy harvester calculated from the data collected on 02/14/2013 (VT and Innowattech).

7.1.5 Power Spectrums (02/22/2013)

Figure 139 shows the calculated power output spectrums of energy harvesters from Virginia Tech and Innowattech.

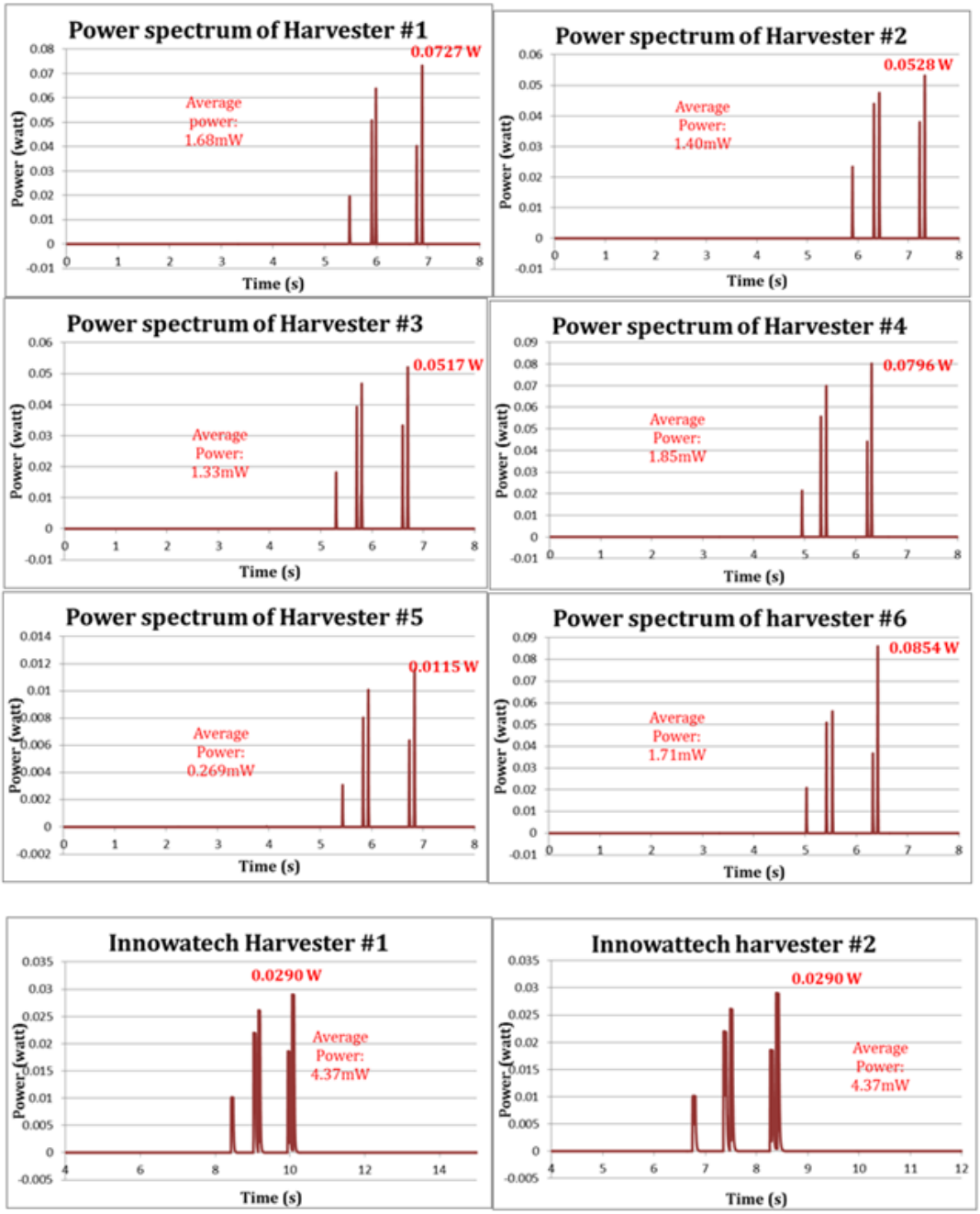

Figure 139. Chart. The power spectrums of the installed energy harvester calculated from the data collected on 02/22/2013 (VT and Innowattech).

7.1.6 Power Spectrums (03/01/2013)

Figure 140 shows the calculated power output spectrums of energy harvesters from Virginia Tech and Innowattech.

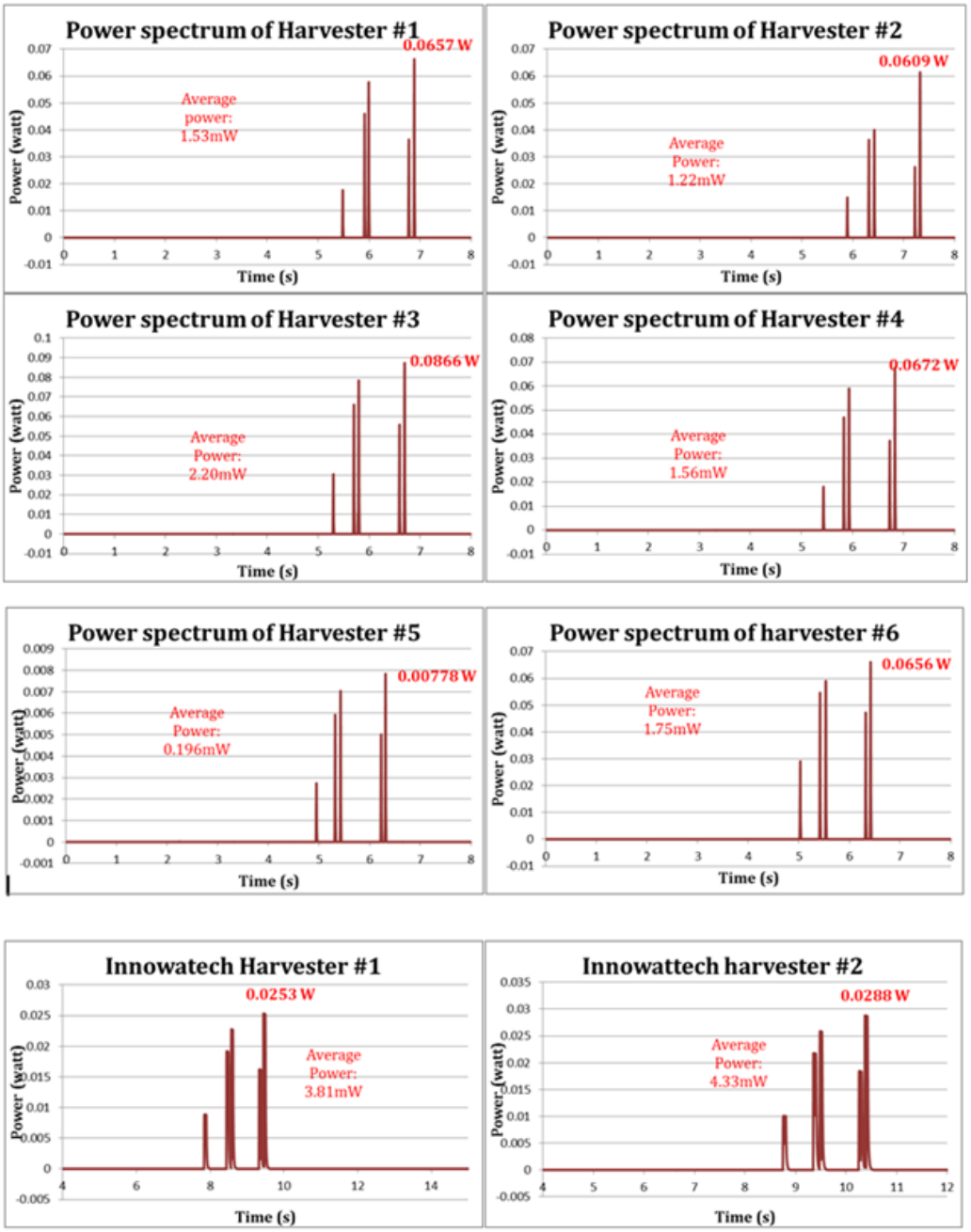

Figure 140. Chart. The power spectrums of the installed energy harvester calculated from the data collected on 03/01/2013 (VT and Innowattech).

7.1.7 Power Spectrums (03/07/2013)

Figure 141 shows the calculated power output spectrums of energy harvesters from Virginia Tech and Innowattech.

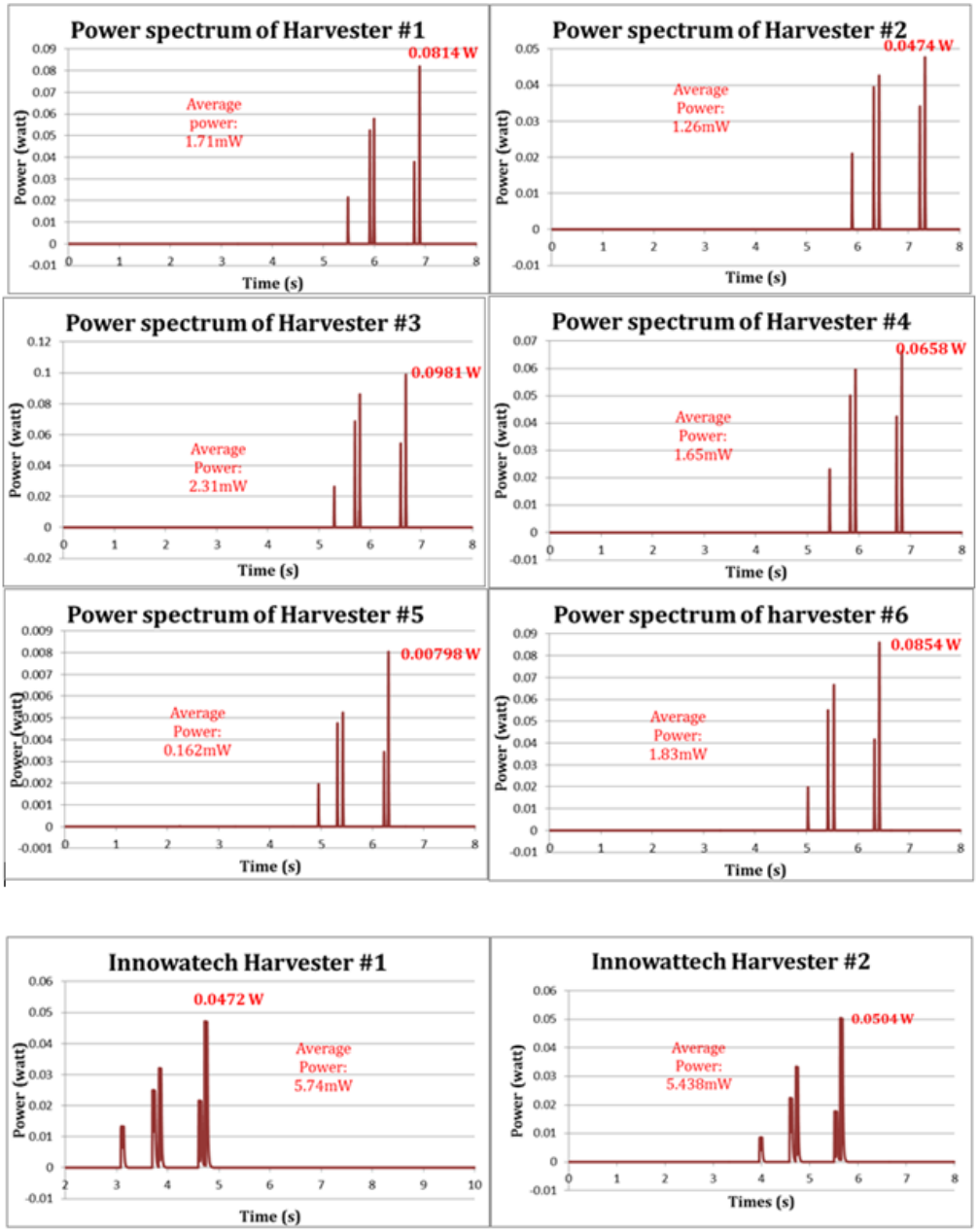

Figure 141. Chart. The power spectrums of the installed energy harvester calculated from the data collected on 03/07/2013 (VT and Innowattech).

7.1.8 Power Spectrums (03/22/2013)

Figure 142 shows the calculated power output spectrums of energy harvesters from Virginia Tech and Innowattech. To have a better look on the shape of the spectrums, Figure 142 shows only the effective part of the spectrums.

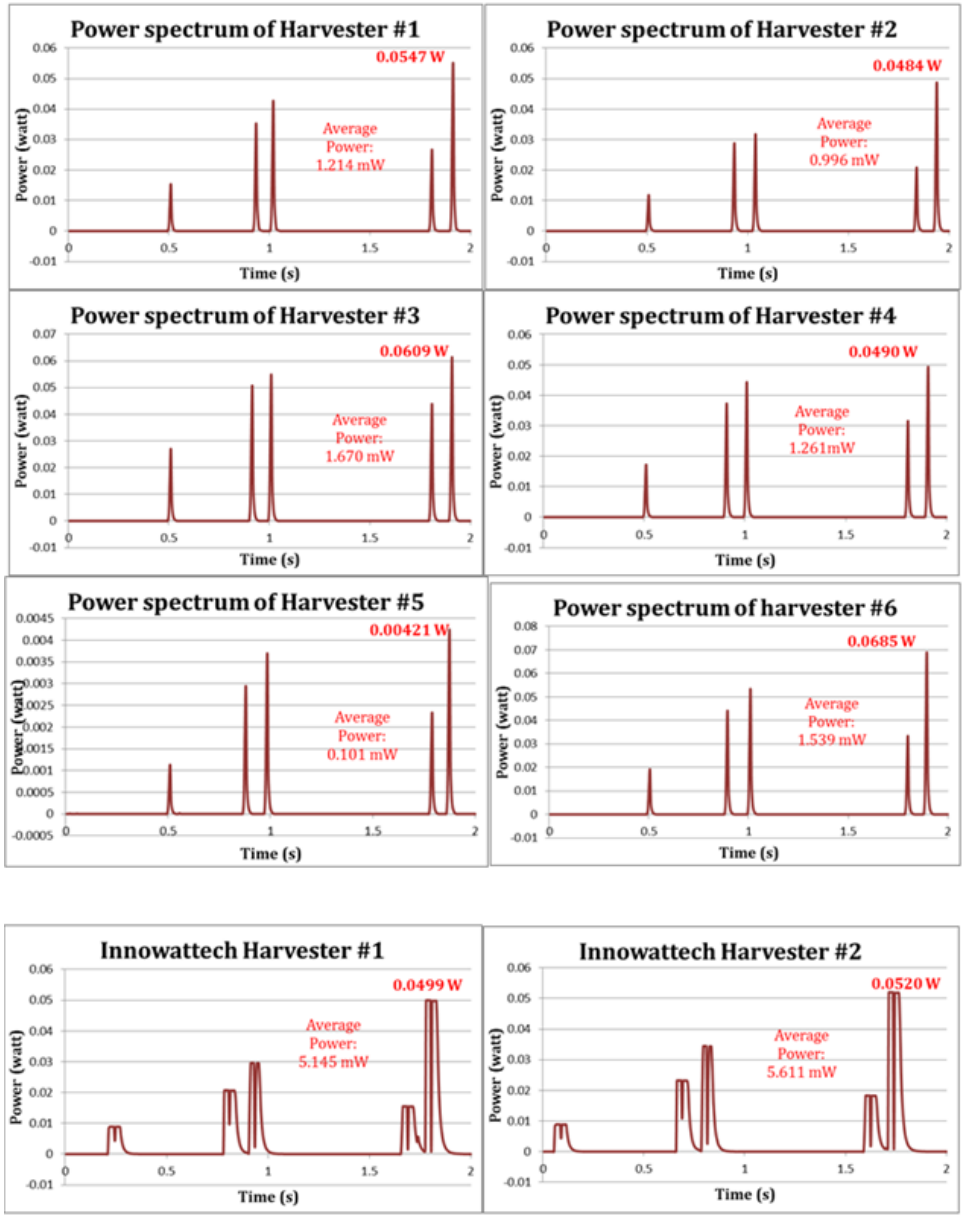

Figure 142. Chart. The power spectrums of the installed energy harvester calculated from the data collected on 03/22/2013 (VT and Innowattech).

7.1.9 Power Spectrums (03/29/2013)

Figure 12 shows the calculated power output spectrums of energy harvesters from Virginia Tech and Innowattech.

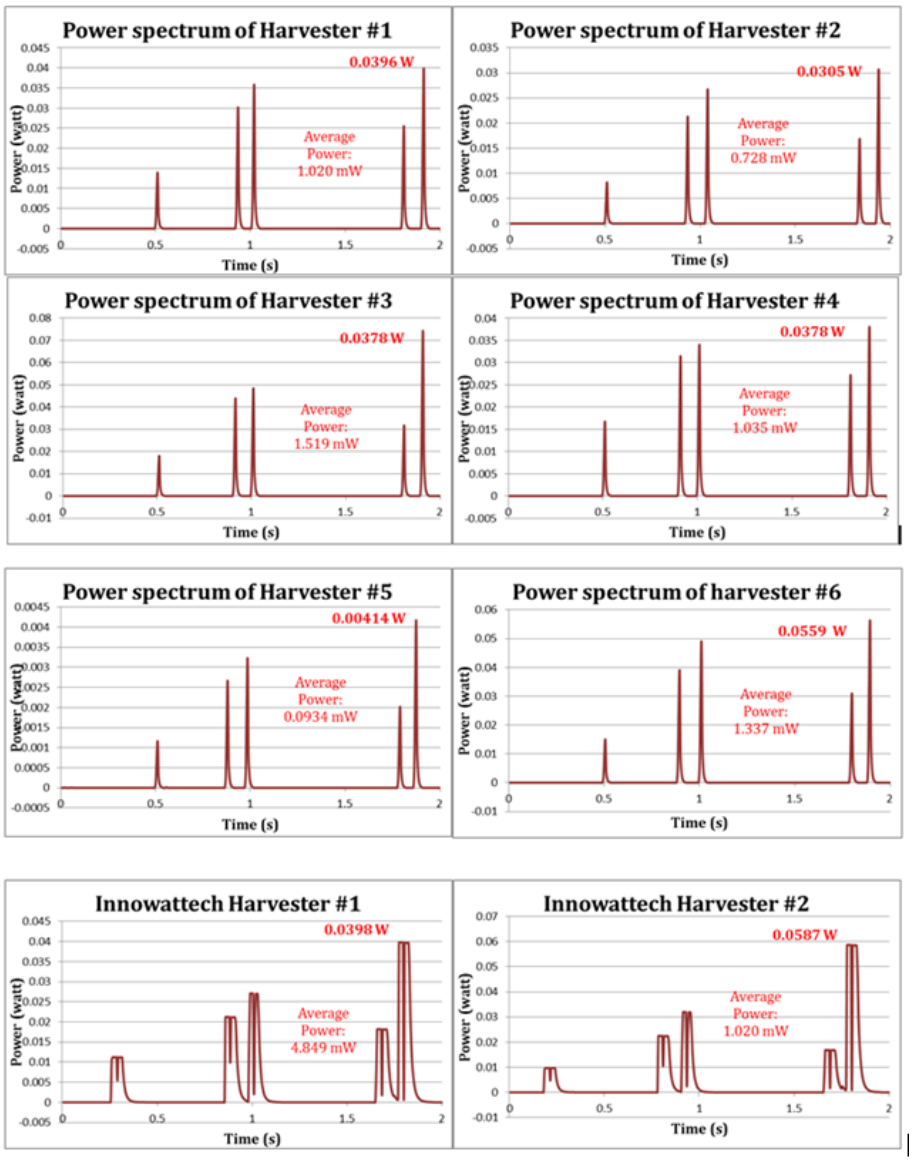

Figure 143. Chart. The power spectrums of the installed energy harvester calculated from the data collected on Power spectrums (04/05/2013).

7.1.10 Power Spectrums (04/05/2013)

Figure 144 shows the calculated power output spectrums of energy harvesters from Virginia Tech and Innowattech. The power output from Energy Harvester #5 significantly dropped.

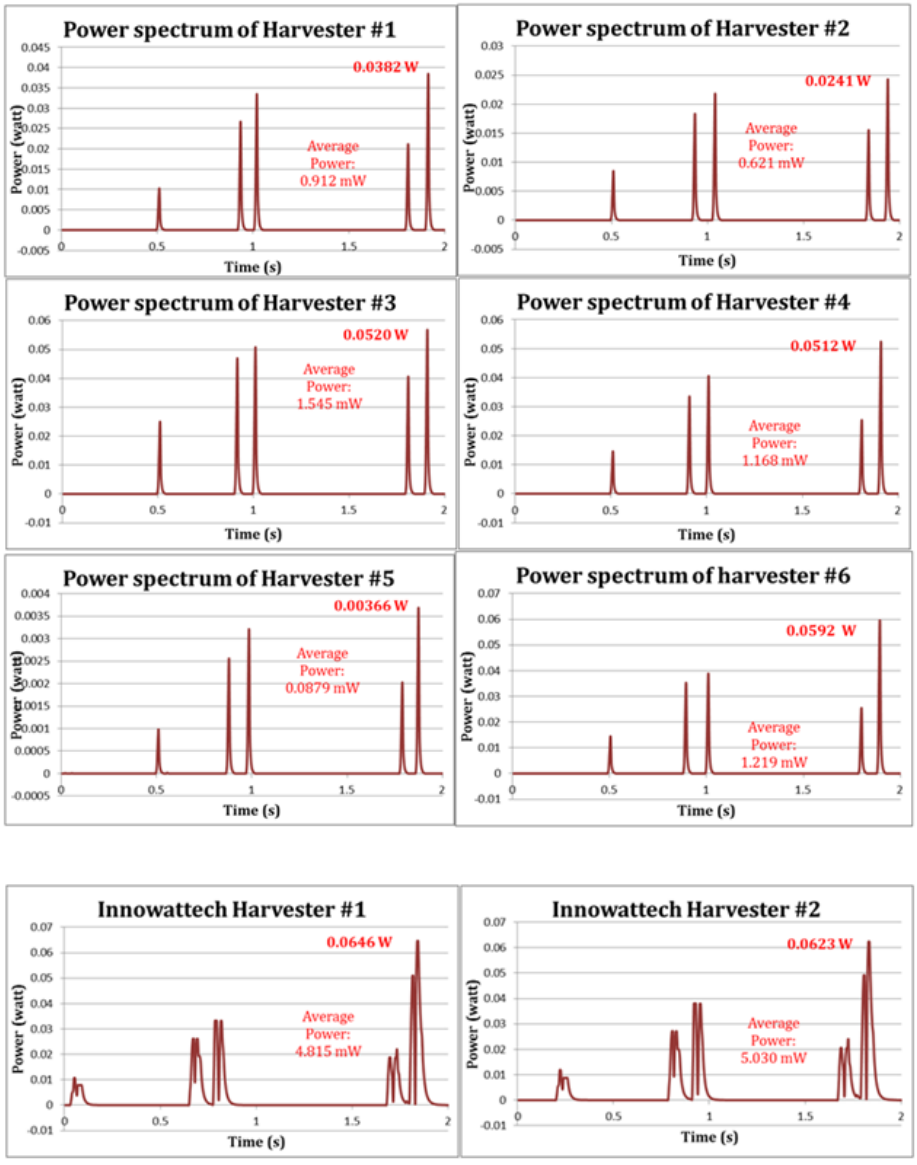

Figure 144. Chart. The power spectrums of the installed energy harvester calculated from the data collected on 04/05/2013 (VT and Innowattech).

7.1.11 Power Spectrums (04/11/2013)

Figure 145 shows the calculated power output spectrums of energy harvesters from Virginia Tech and Innowattech.

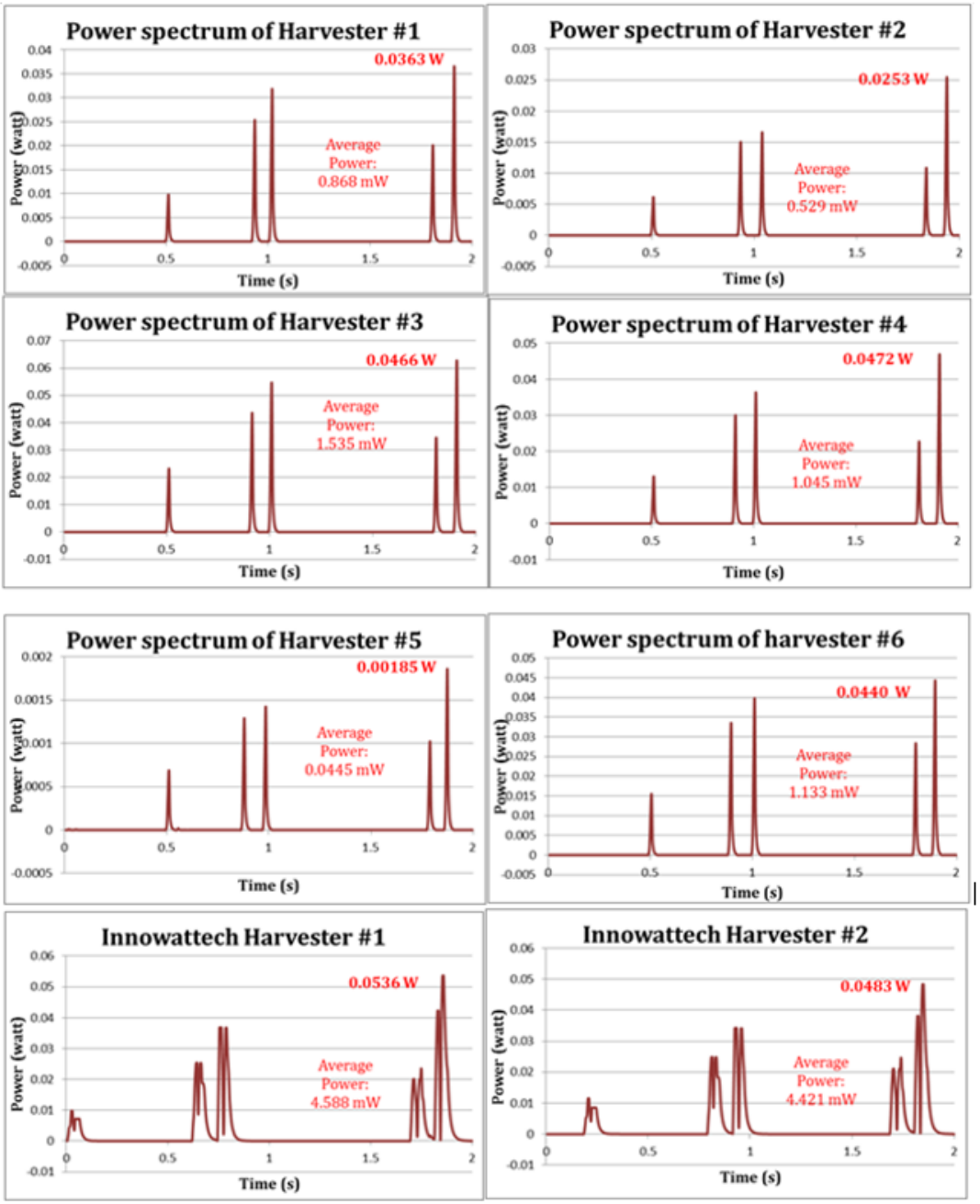

Figure 145. Chart. The power spectrums of the installed energy harvester calculated from the data collected on 04/11/2013 (VT and Innowattech).

7.1.12 Power Spectrums (04/19/2013)

Figure 146 shows the calculated power output spectrums of energy harvesters from Virginia Tech and Innowattech. Energy harvester #5 stopped working.

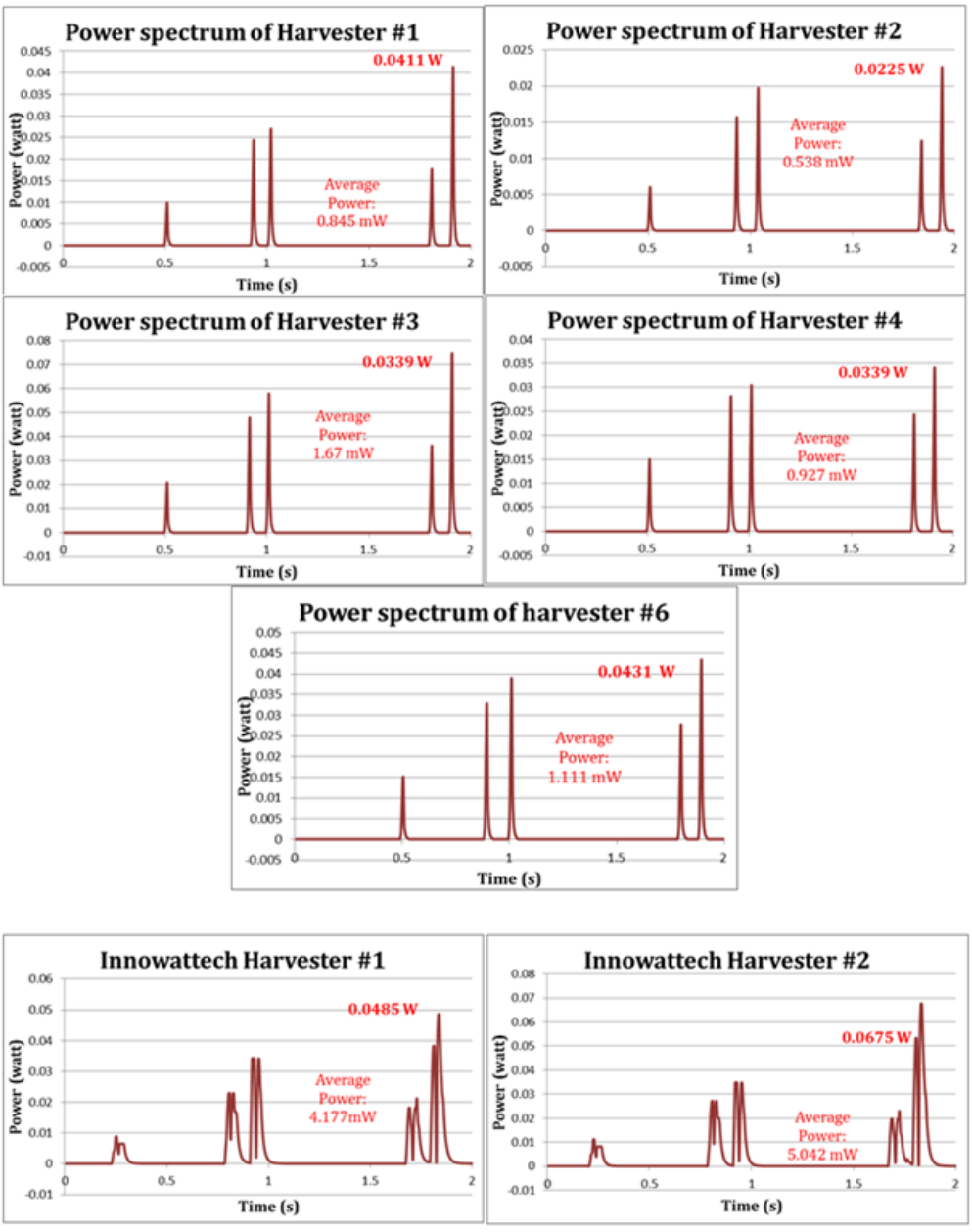

Figure 146. Chart. The power spectrums of the installed energy harvester calculated from the data collected on 04/19/2013 (VT and Innowattech).

7.1.13 Power Spectrums (04/26/2013)

Figure 147 shows the calculated power output spectrums of energy harvesters from Virginia Tech and Innowattech.

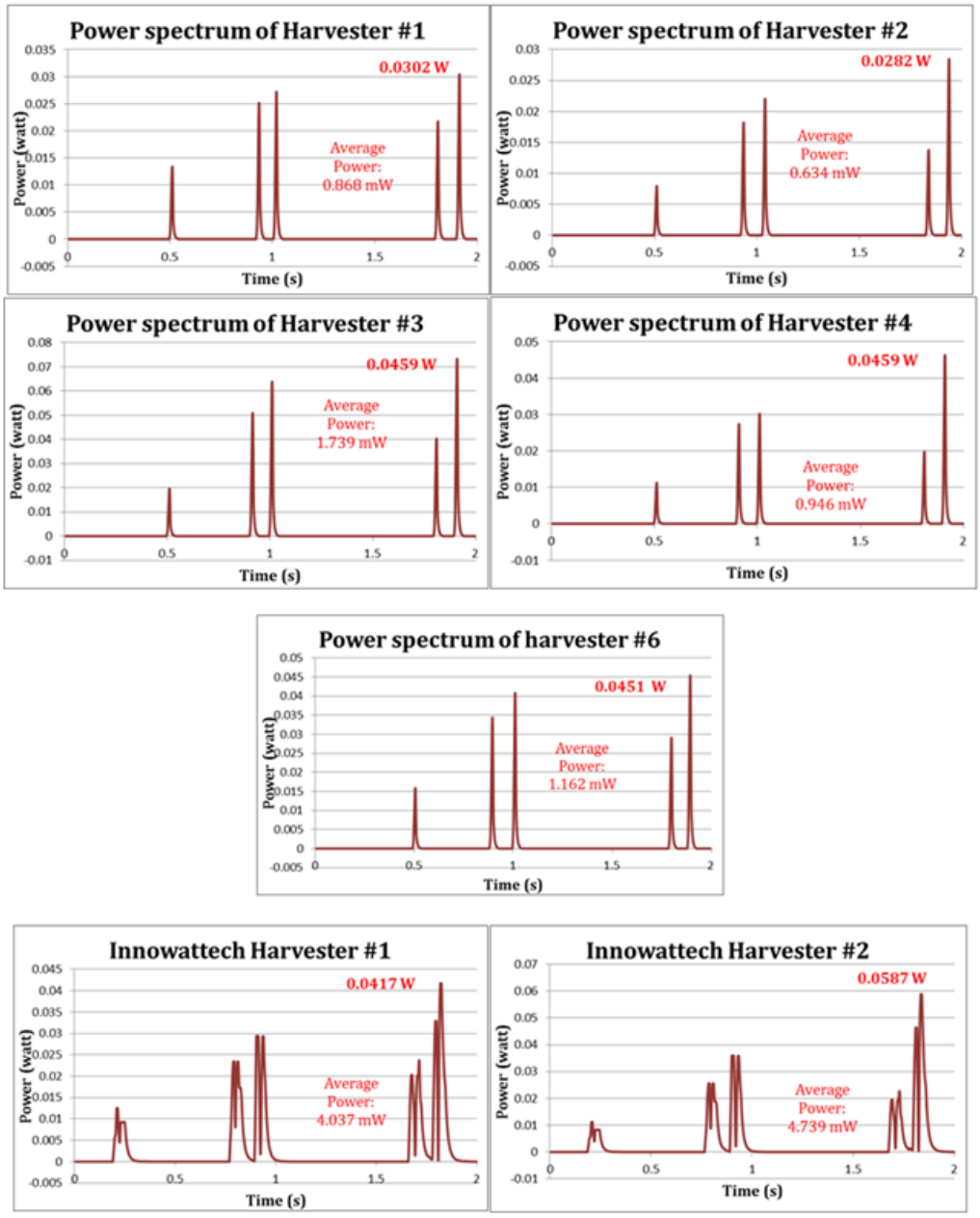

Figure 147. Chart. The power spectrums of the installed energy harvester calculated from the data collected on 04/26/2013 (VT and Innowattech).

7.1.14 Power Spectrums (05/10/2013)

Figure 148 shows the calculated power output spectrums of energy harvesters from Virginia Tech and Innowattech.

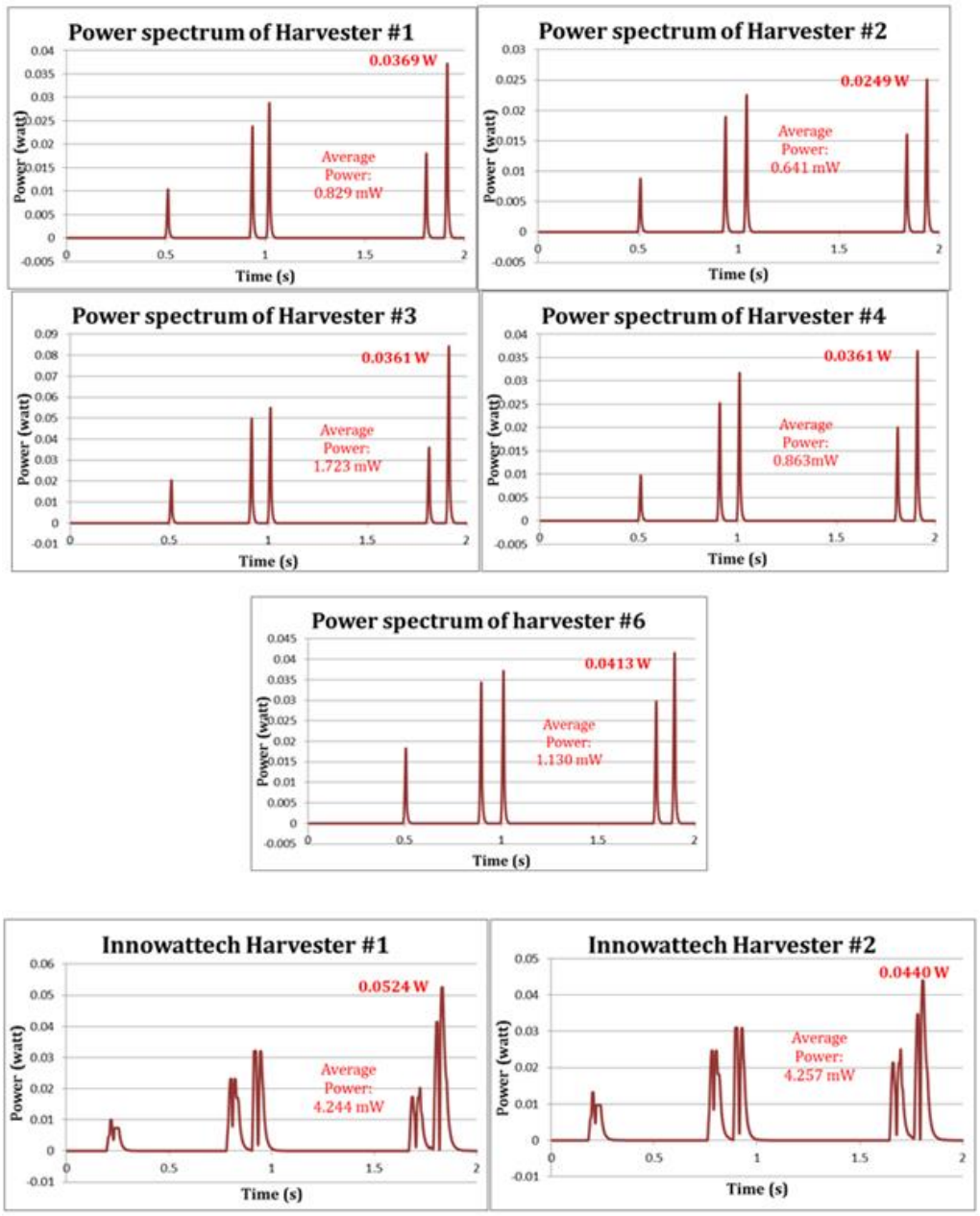

Figure 148. Chart. The power spectrums of the installed energy harvester calculated from the data collected on 05/10/2013 (VT and Innowattech).

7.1.15 Power Spectrums (06/14/2013)

Figure 149 shows the calculated power output spectrums of energy harvesters from Virginia Tech and Innowattech.

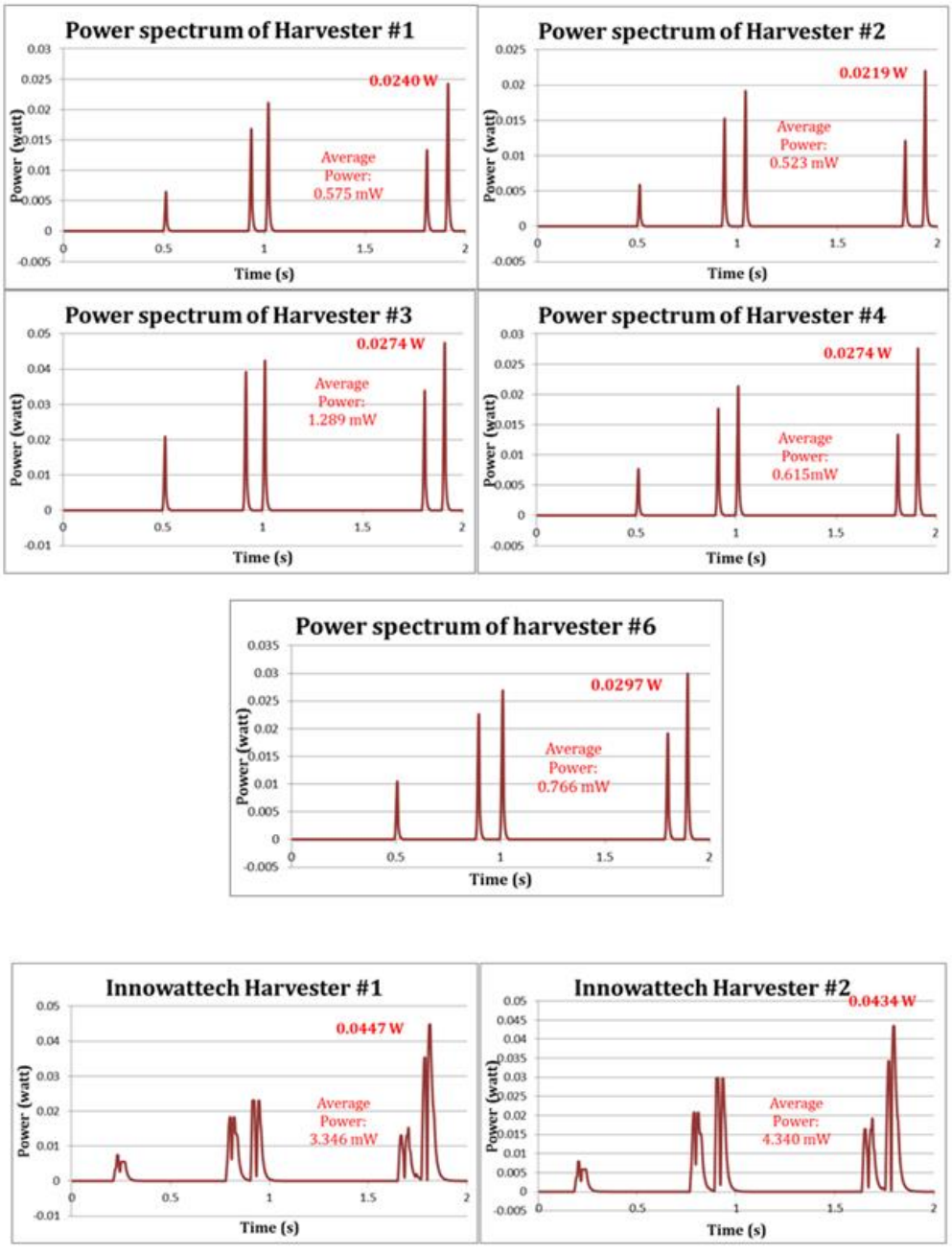

Figure 149. Chart. The power spectrums of the installed energy harvester calculated from the data collected on 06/14/2013 (VT and Innowattech).

7.1.16 Power Spectrums (06/21/2013)

Figure 150 shows the calculated power output spectrums of energy harvesters from Virginia Tech and Innowattech. The power output of Energy harvester #4 significantly redueced.

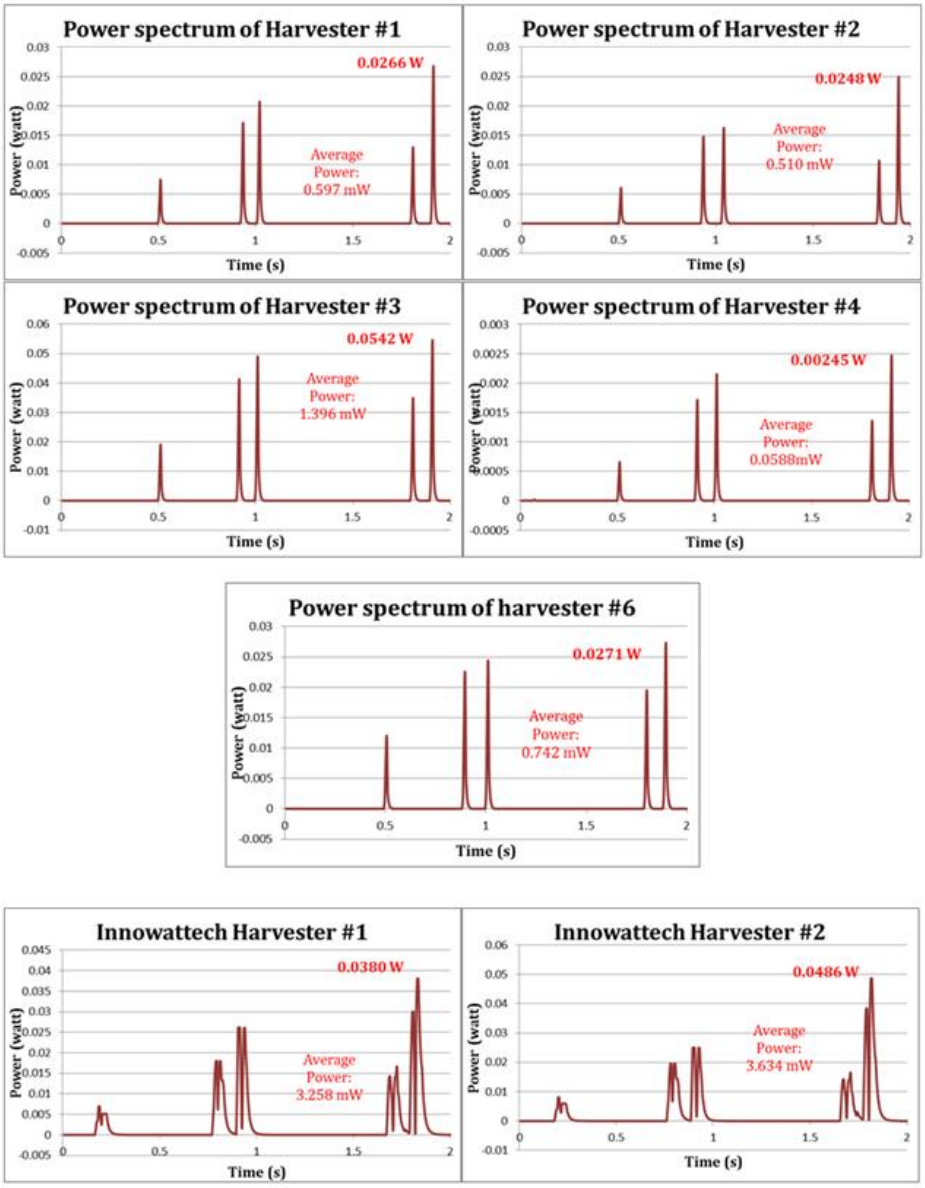

Figure 150. Chart. The power spectrums of the installed energy harvester calculated from the data collected on 06/21/2013 (VT and Innowattech).

7.1.17 Power Spectrums (06/28/2013)

Figure 151 shows the calculated power output spectrums of energy harvesters from Virginia Tech and Innowattech. To have a better look on the shape of the spectrums, Figure 151 shows only the effective part of the spectrums.

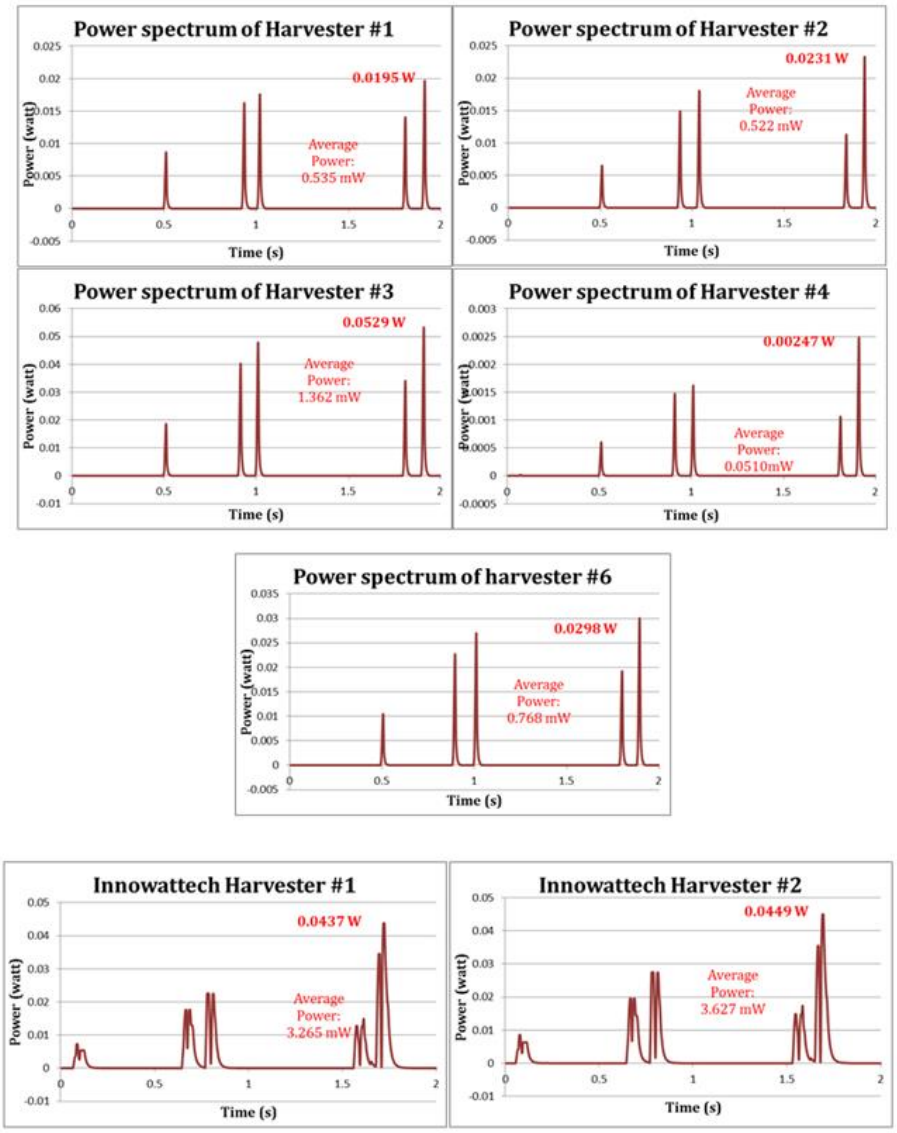

Figure 151. Chart. The power spectrums of the installed energy harvester calculated from the data collected on 06/28/2013 (VT and Innowattech).

7.1.18 Power Spectrums (07/05/2013)

Figure 152 shows the calculated power output spectrums of energy harvesters from Virginia Tech and Innowattech. Harvester #4 has stopped working.

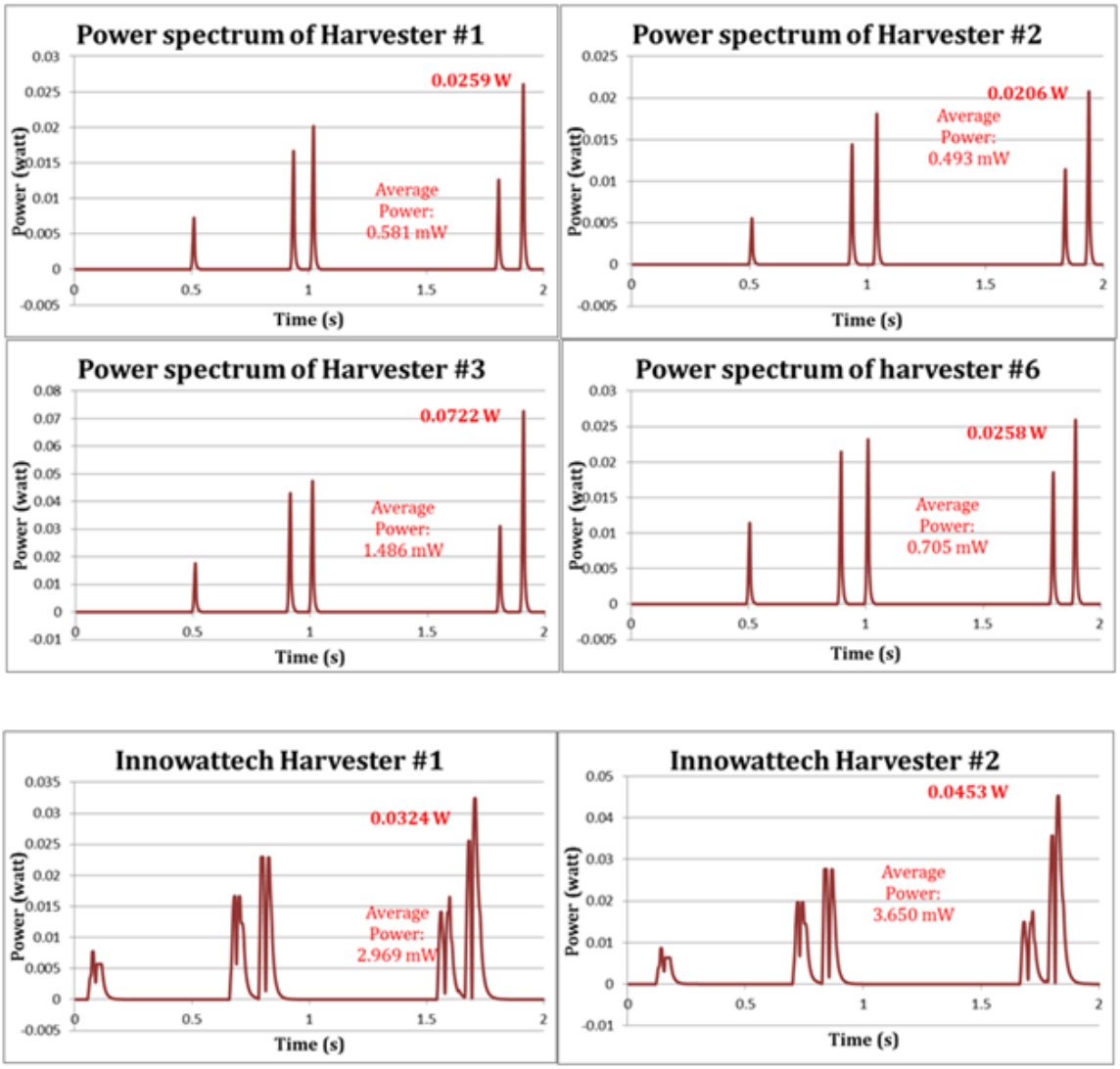

Figure 152. Chart. The power spectrums of the installed energy harvester calculated from the data collected on 07/05/2013 (VT and Innowattech).

7.1.19 Power Spectrums (07/26/2013)

Figure 153 shows the spectrums of power output measured from the energy harvesters fabricated by Virginia Tech and Innowattech.

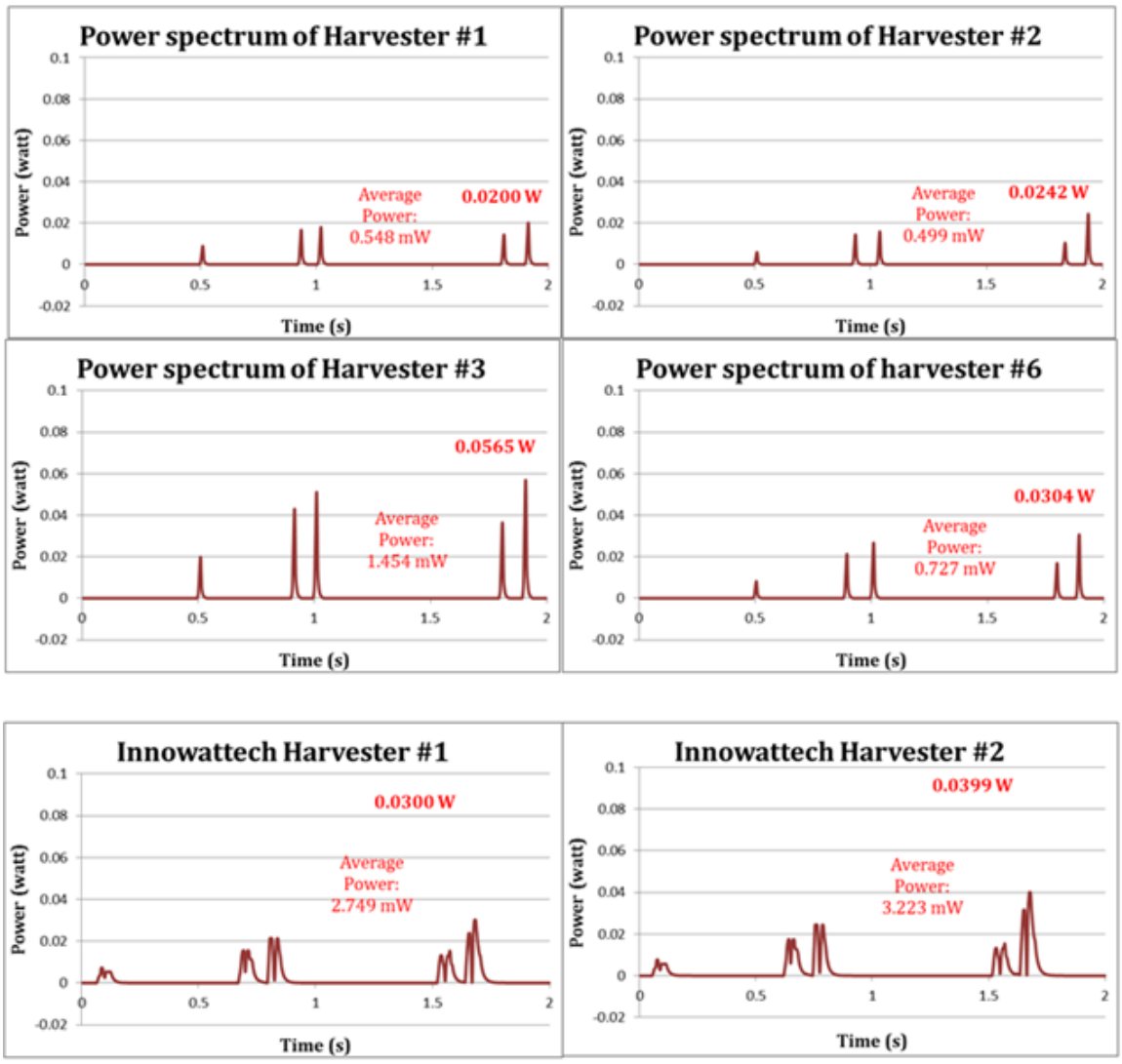

Figure 153. Chart. The power spectrums of the installed energy harvester calculated from the data collected on 07/26/2013 (VT and Innowattech).

7.1.20 Power Spectrums (08/09/2013)

Figure 154 shows the spectrums of power output measured from the energy harvesters fabricated by Virginia Tech and Innowattech.

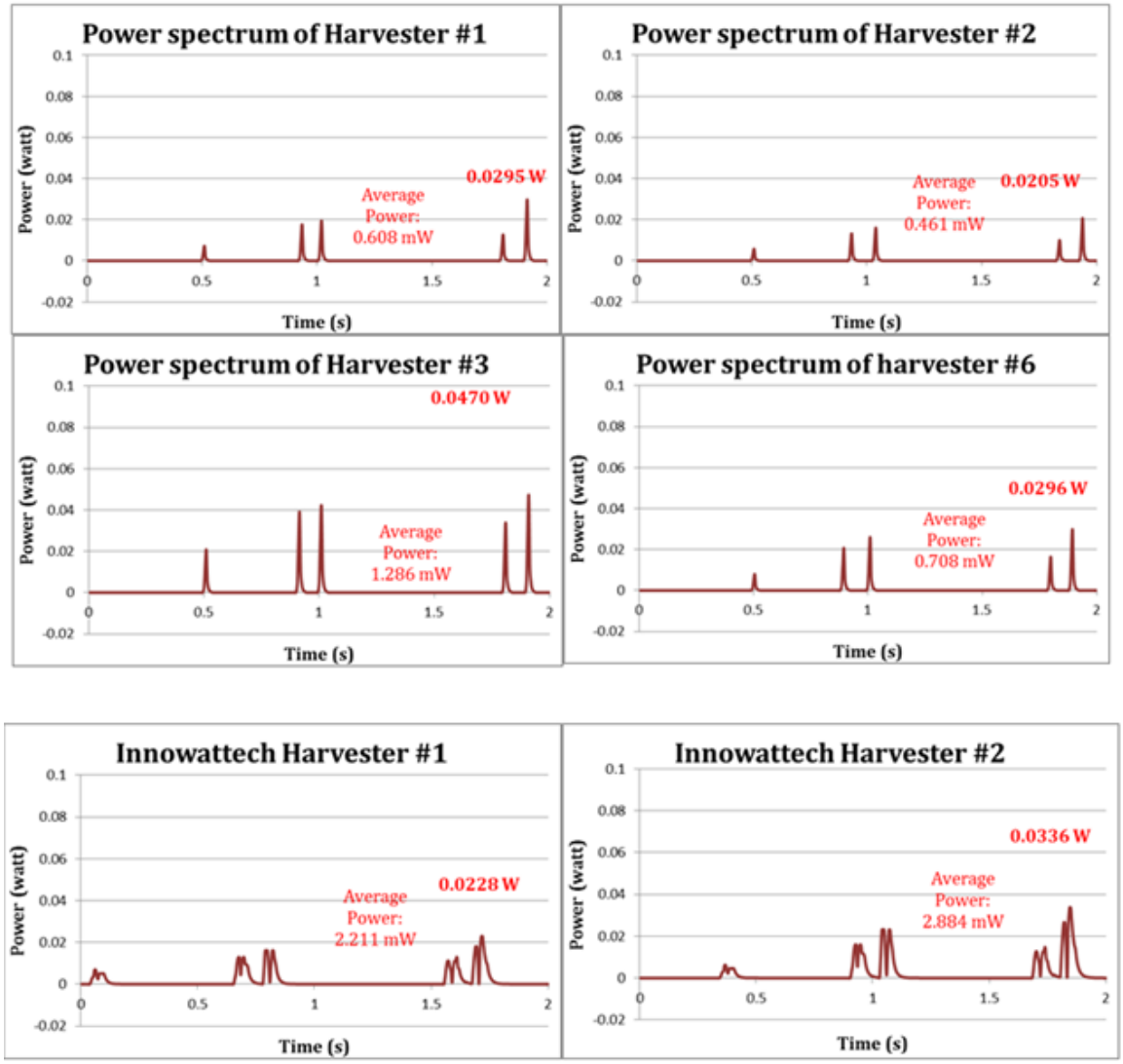

Figure 154. Chart. The power spectrums of the installed energy harvester calculated from the data collected on 08/09/2013 (VT and Innowattech).

7.1.21 Power Spectrums (08/16/2013)

Figure 155 shows the spectrums of power output measured from the energy harvesters fabricated by Virginia Tech and Innowattech.

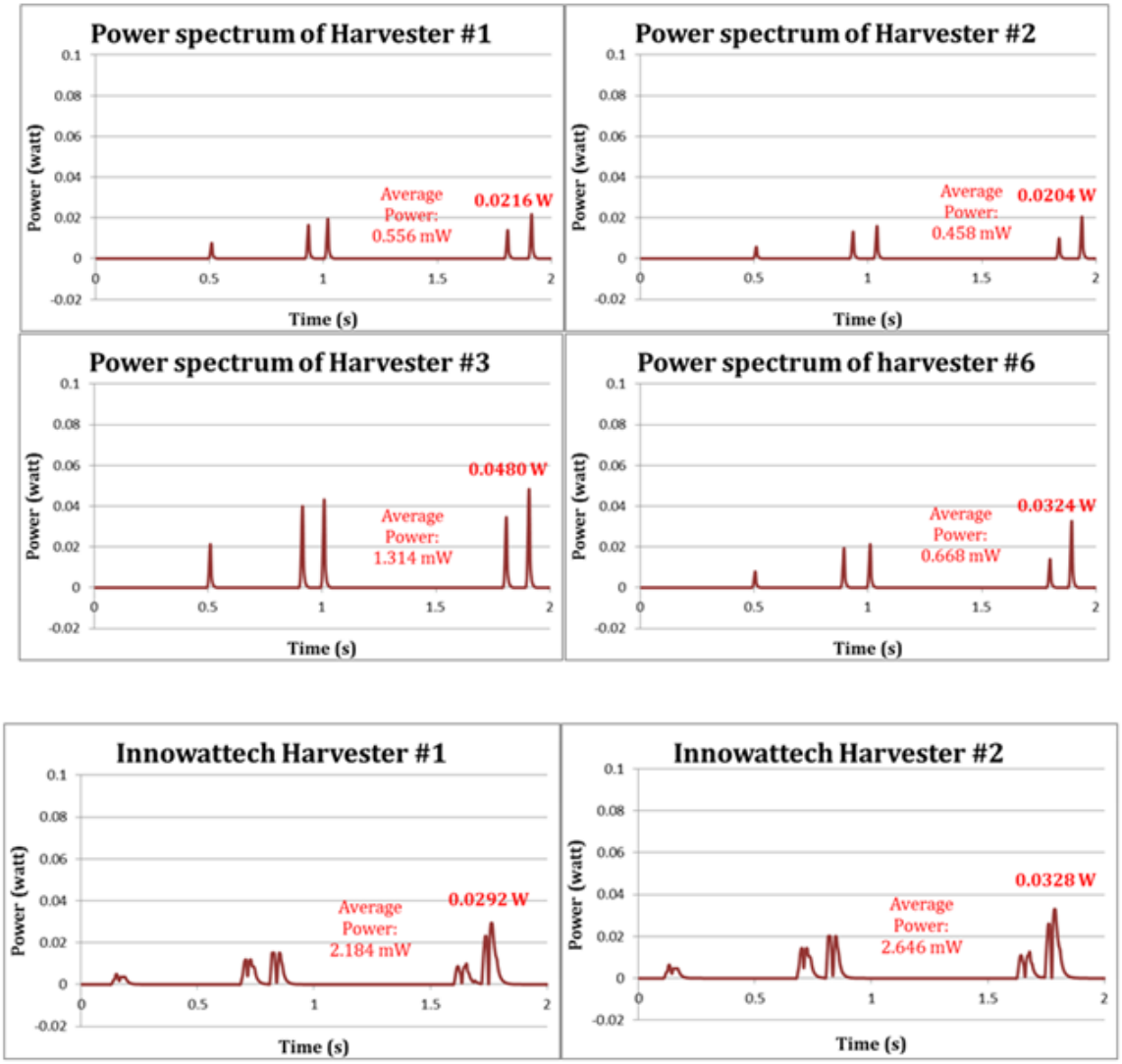

Figure 155. Chart. The power spectrums of the installed energy harvester calculated from the data collected on 08/16/2013 (VT and Innowattech).

7.1.22 Power Spectrums (08/23/2013)

Figure 156 shows the spectrums of power output measured from the energy harvesters fabricated by Virginia Tech and Innowattech.

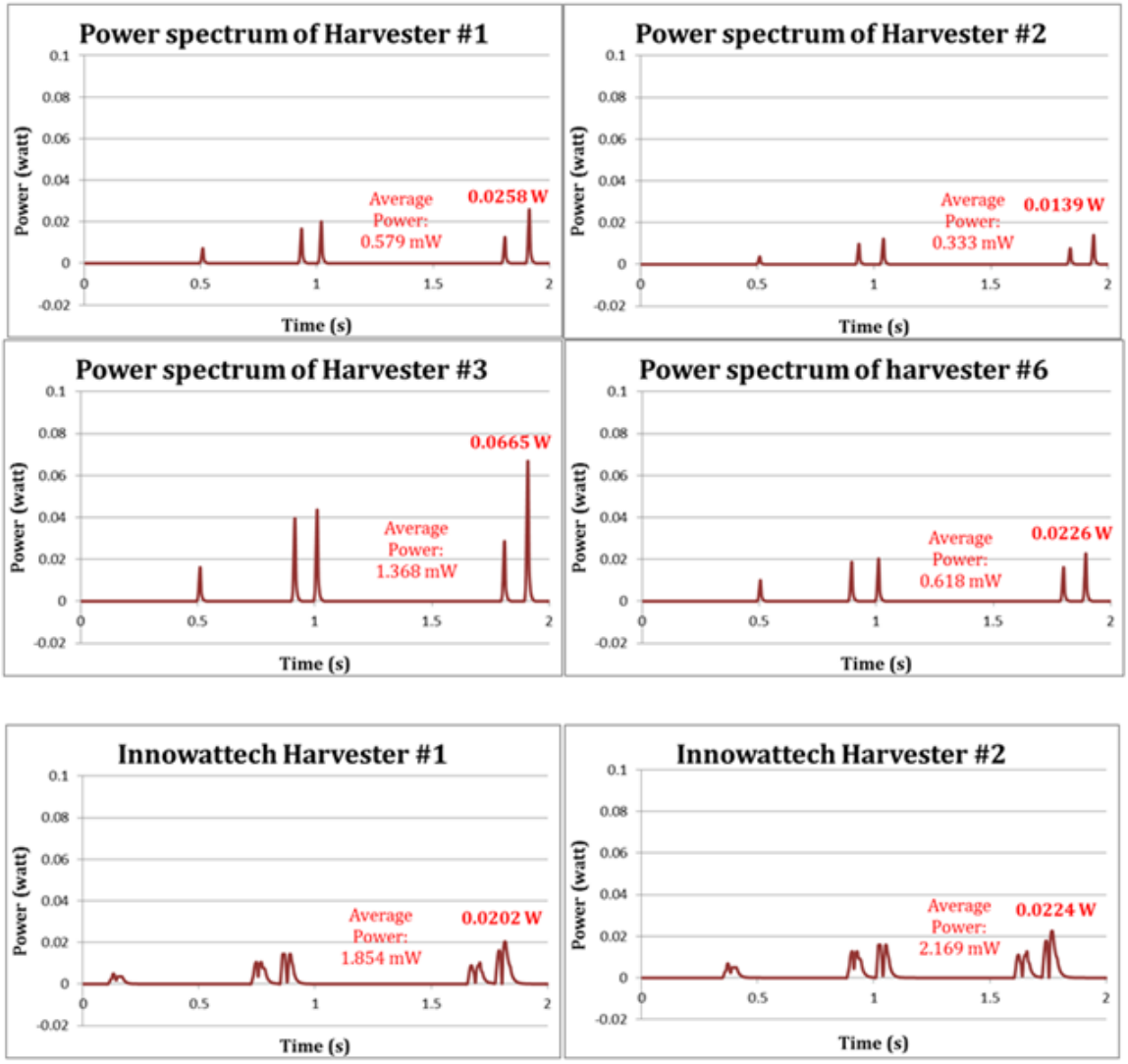

Figure 156. Chart. The power spectrums of the installed energy harvester calculated from the data collected on 08/23/2013 (VT and Innowattech).

7.1.23 Power Spectrums (08/31/2013)

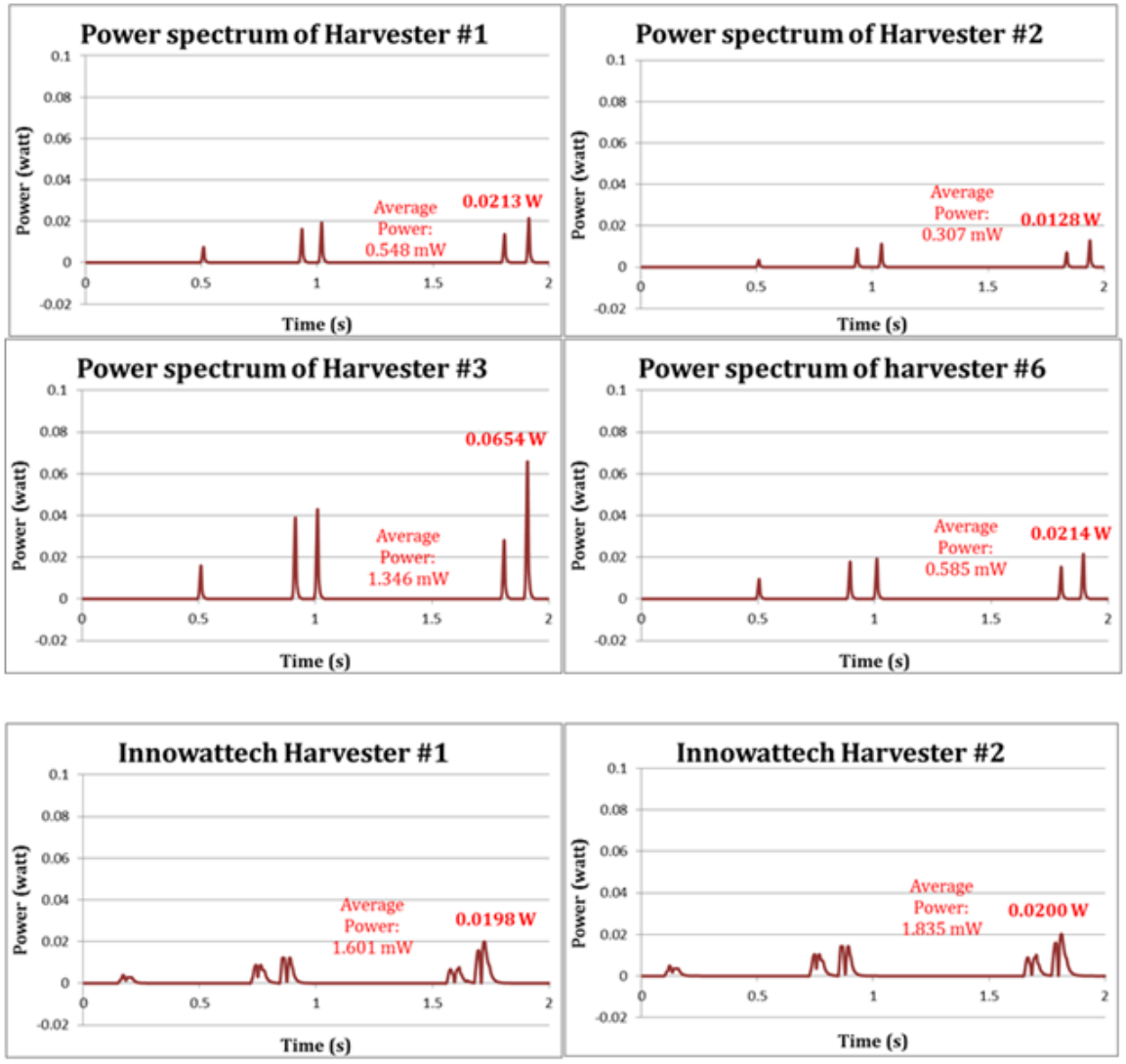

Figure 157. Chart. The power spectrums of the installed energy harvester calculated from the data collected on 08/31/2013 (VT and Innowattech).

7.1.24 Power Spectrums (09/25/2013)

Figure 158 shows the spectrums of power output measured from the energy harvesters fabricated by Virginia Tech and Innowattech. Energy harvester #2 and Innowattech Harvester #1 don't have any electric output from passing vehicles.

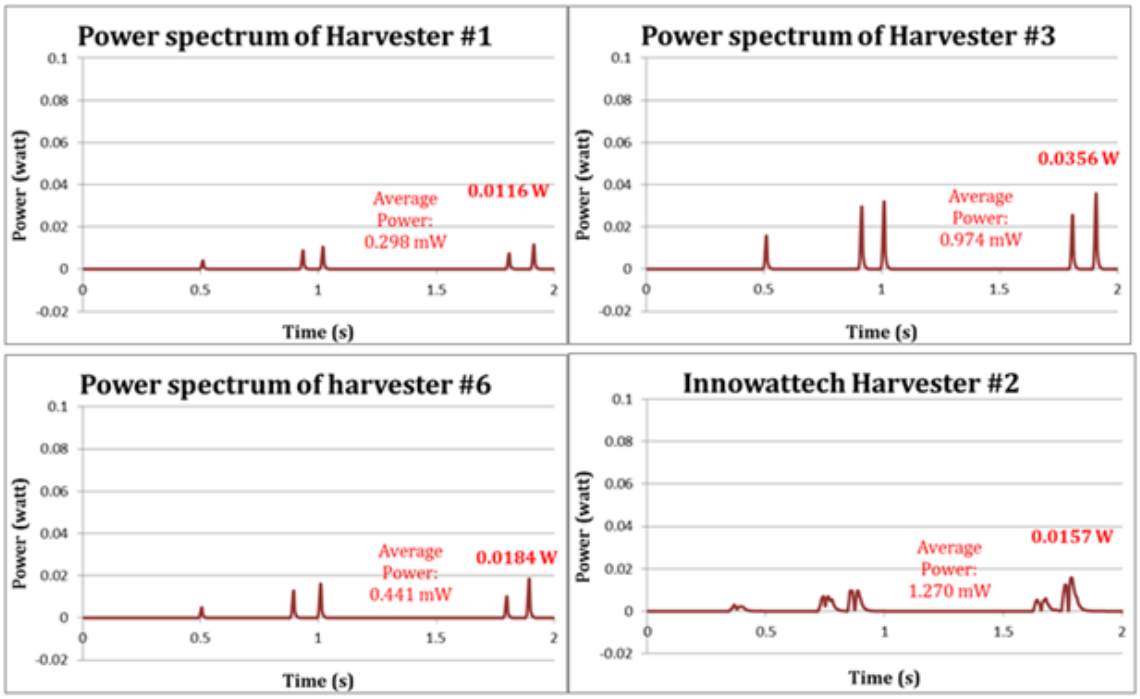

Figure 158. Chart. The power spectrums of the installed energy harvester calculated from the data collected on 09/25/2013 (VT and Innowattech).

7.1.25 Power Spectrums (10/18/2013)

Figure 159 shows the spectrums of power output measured from the energy harvesters fabricated by Virginia Tech and Innowattech.

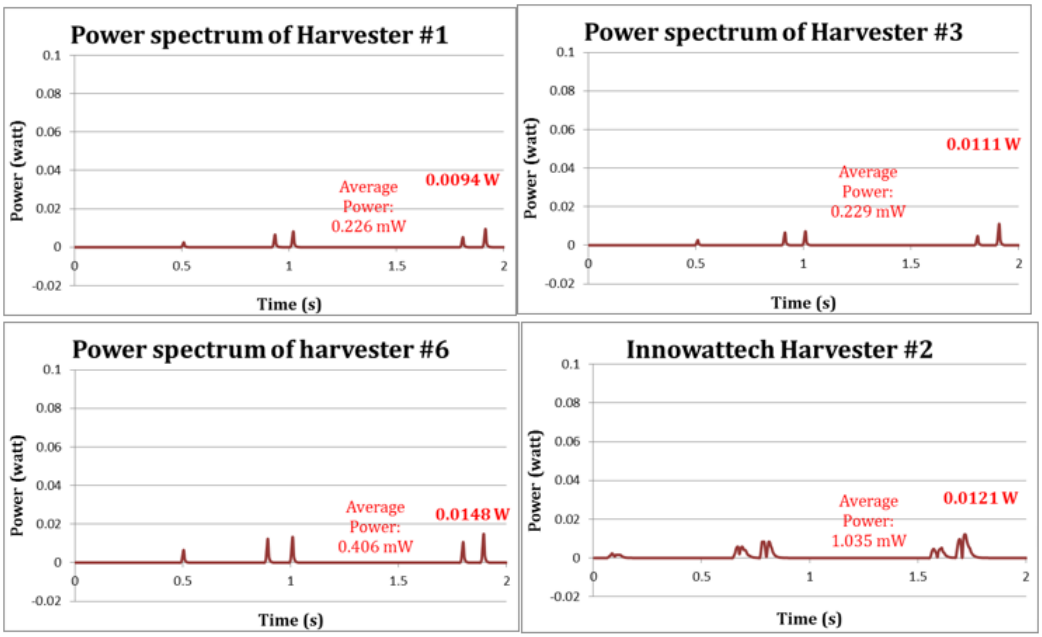

Figure 159. Chart. The power spectrums of the installed energy harvesters analyzed from the data collected on 10/18/2013 (VT and Innowattech).

7.1.26 Power Spectrums (11/07/2013)

Figure 160 shows the spectrums of power output measured from the energy harvesters fabricated by Virginia Tech and Innowattech.

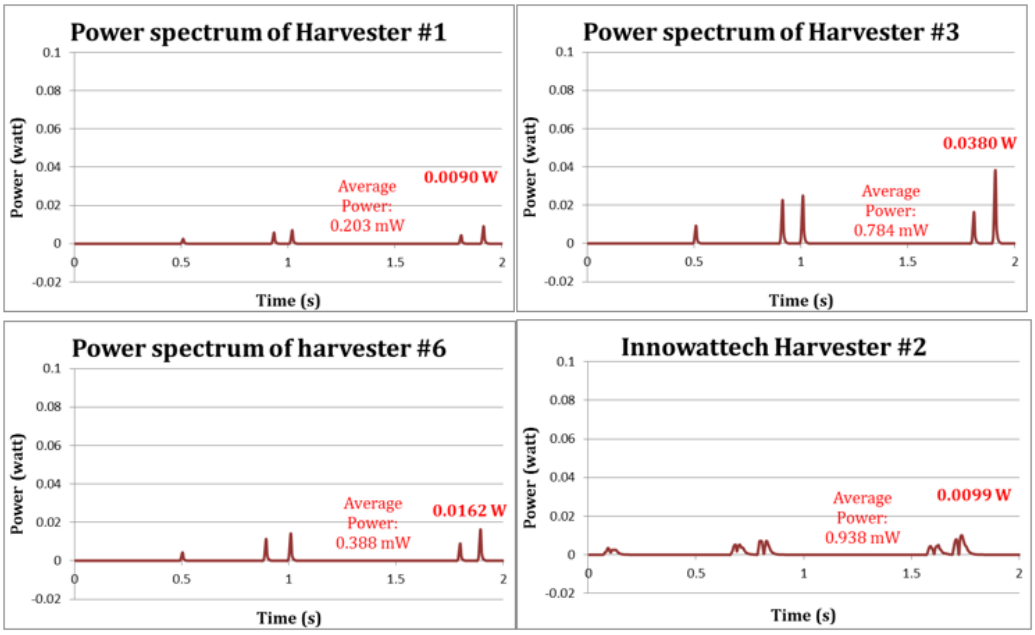

Figure 160. Chart. The power spectrums of the installed energy harvesters analyzed from the data collected on 11/07/2013 (VT and Innowattech).

7.1.27 Power Spectrums (11/11/2013)

Figure 161 shows the spectrums of power output measured from the energy harvesters fabricated by Virginia Tech and Innowattech. Energy harvester #1 had stopped working.

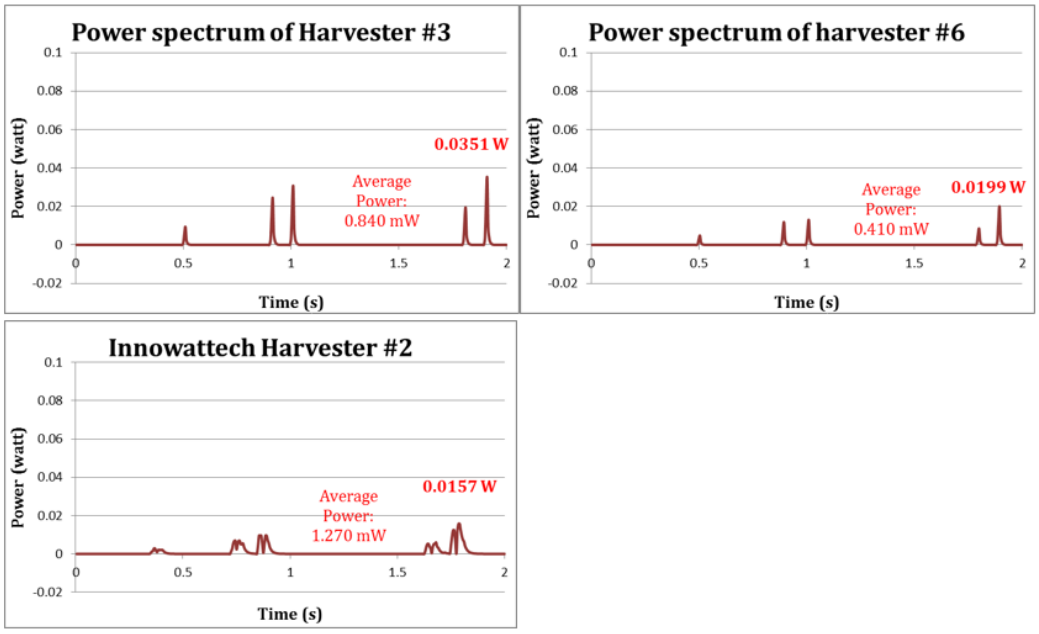

Figure 161. Chart. The power spectrums of the installed energy harvesters analyzed from the data collected on 11/11/2013 (VT and Innowattech).

7.1.28 Power Spectrums (11/18/2013)

Figure 162 shows the spectrums of power output measured from the energy harvesters fabricated by Virginia Tech and Innowattech.

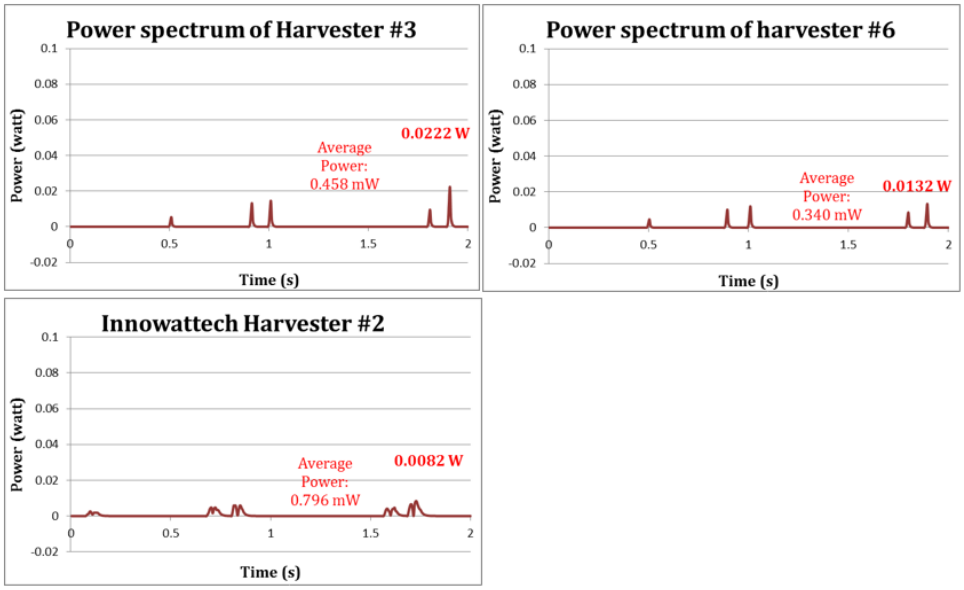

Figure 162. Chart. The power spectrums of the installed energy harvester calculated from the data collected on 11/18/2013 (VT and Innowattech).

7.1.29 Power Spectrums (12/06/2013)

Figure 163 shows the spectrums of power output measured from the energy harvesters fabricated by Virginia Tech and Innowattech.

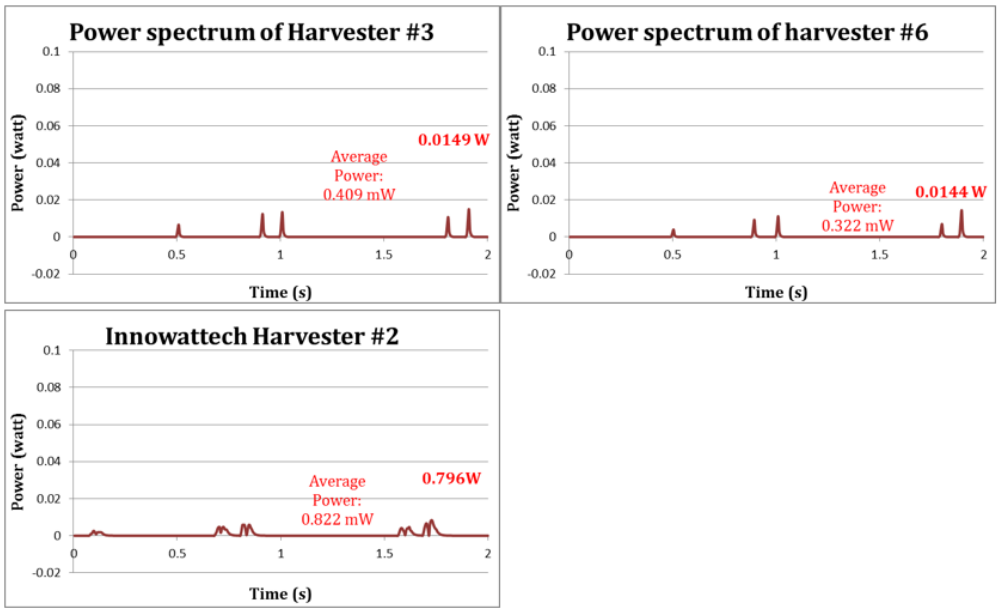

Figure 163. Chart. The power spectrums of the installed energy harvester calculated from the data collected on 12/20/2013 (VT and Innowattech).

7.1.30 Power Spectrums (01/03/2014)

Figure 164 shows the spectrums of power output measured from the energy harvesters fabricated by Virginia Tech and Innowattech. Energy harvester #5 has stopped working.

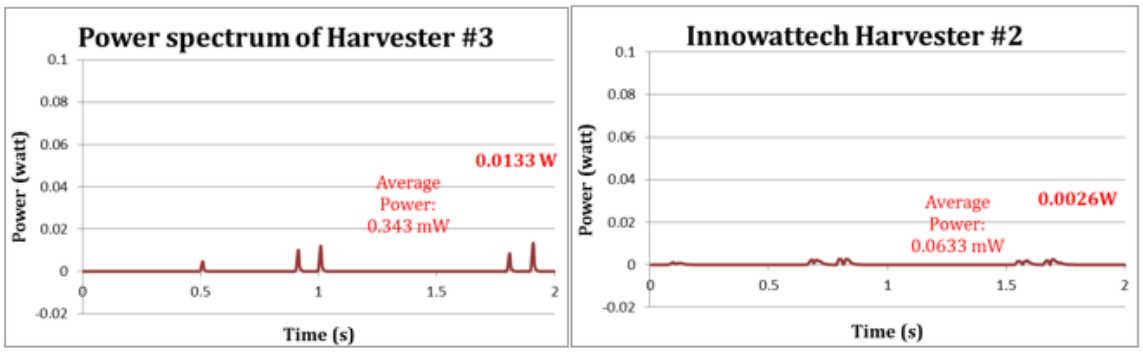

Figure 164. Chart. The power spectrums of the installed energy harvesters analyzed from the data collected on 01/03/2014 (VT and Innowattech).

7.1.31 Power Spectrum (02/14/2014)

All eight energy harvesters installed at Troutville weigh station have stopped working by Feb 14th 2014.

7.2 NiMH Batteries Pack Charging

NiMH battery is known as a rechargeable battery with high capacitance. One important characteristic of this type of battery is that it doesn't require special charging voltage and current. It provides an easier methodology of energy storage of energy harvesting technology. To better understand the electric characteristic of the NiMH battery, the charging and discharging curves of the NiMH battery were studied by performing charging and discharging tests.

One NiMH battery stack is parallel connected to all six installed energy harvesters at weigh station to perform the charging test. The battery stack consists of three NiMH battery and can be charged up to 3.6V. The charging curve (voltage versus time) is

measured using a data logger which records the data automatically. The charging tests were performed in November 2012 and November 2013. Figure 165 shows the NiMH battery stack being charged and connected to the data logger.

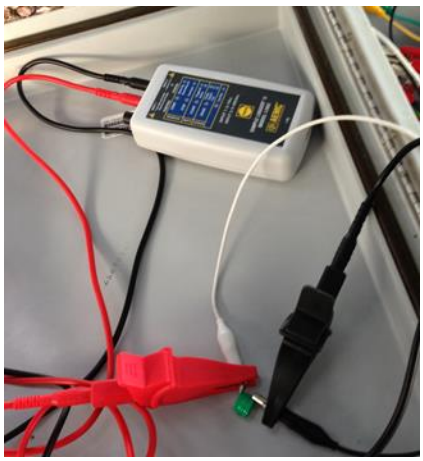

Figure 165. Photo. The charging NiMH battery stack connected with the data logger.

7.2.1 Charging Test (Nov, 2012)

The same NiMH battery pack has being tested by getting charged using the energy harvesters installed at Troutville weigh station. The voltage of the battery pack was measured by a data logger for every 8 hours. It linearly increases over time until it reaches 2V. Then voltage increased with a much lower rate until the battery pack was fully charged after the 6 days. Figure 166 shows the curve of the voltage measured during the charging process. The battery pack would be charged with a constant charging rate if the traffic at weigh station remain on the same level. As a result, 5% of the capacitance of the battery pack would be charged by the energy harvester for every eight hours.

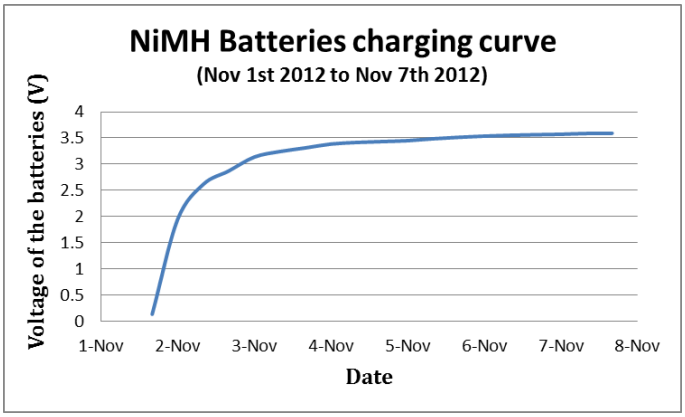

Figure 166. Chart. The voltage of the NiMH battery pack measured during the charging process (Starting Nov 1st 2012, using energy harvesters installed at Troutville weigh station).

7.2.2 Charging Test (Nov, 2013)

To investigate how much it will impact the charging process, another charging test was performed using the same battery pack. The battery was connected to the energy harvesters after getting fully discharged. Figure 167 shows the voltage on the battery pack measured during the charging process by a data logger for every 8 hours. According to the voltage curve, the voltage on the battery pack increased linearly over time until it reaches 2V. Then voltage on the battery pack increased with a much lower rate till the battery get fully charged. The charging started from November 11th and ended on December 26th 2013. It took 50 more days than the first charging test to fully charge the same battery pack. The difference of charging time duration is caused by the energy output degradation. The average power output of the energy harvesters from each pass of vehicle during the first charging test is 13.938mW. The average power output of the energy harvesters during the second charging test is 1.25mW, which is about 1/10 of the

power output during the first charging test and makes the charging time of the second test reasonable.

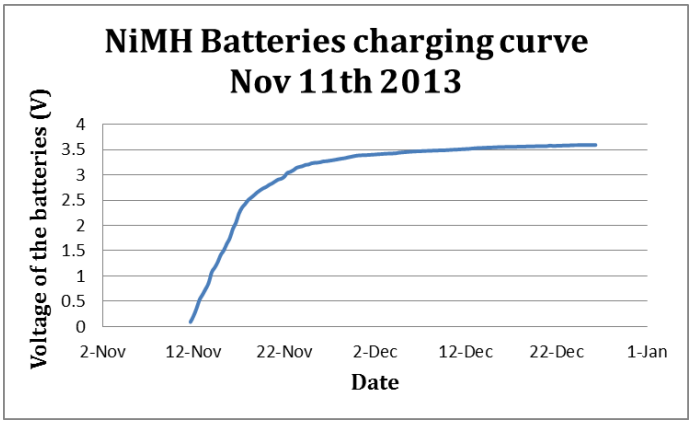

Figure 167. Chart. The voltage of the NiMH battery pack measured during the charging process (Starting from Nov 1th 2013, using energy harvesters installed at Troutville weigh station).

From the two charging tests, it's found that the NiMH battery can store the energy for the energy harvesters with a small input energy. It's noticeable that the voltage on the battery pack doesn't linearly increase with the energy stored.

7.3 The Performance Degrading of the Installed Harvester at Troutville Weigh Station

Figure 168 presents the trend curves of the maximum average power measured from all energy harvesters installed at Troutville weigh station. Each of data points represents the numeric average of the maximum average power output of corresponding energy harvester in each month. The power output data of the Innowattech's harvesters is not available until January 2013 because Innowattech required to test their harvesters with same vehicle using an oscillation scope, which are not available. After reaching an

agreement that Virginia Tech will test all eight energy harvesters with their methodology, the test on the Innowattech's harvesters were performed.

According to the power output spectrums analyzed from the electric output, the energy generated (the maximum power output among the data collected) by passed vehicle from the piezoelectric energy harvesters installed at Troutville weigh station has degraded significantly. Functional failure has been identified on the Energy Harvester #2, # 4 and #5, and the Innowattech Harvester #1 during the period of data measurement. As shown in the trend curves, the power generation of all eight piezoelectric energy harvesters (six from Virginia Tech, two from Innowattech) has decreased significantly.

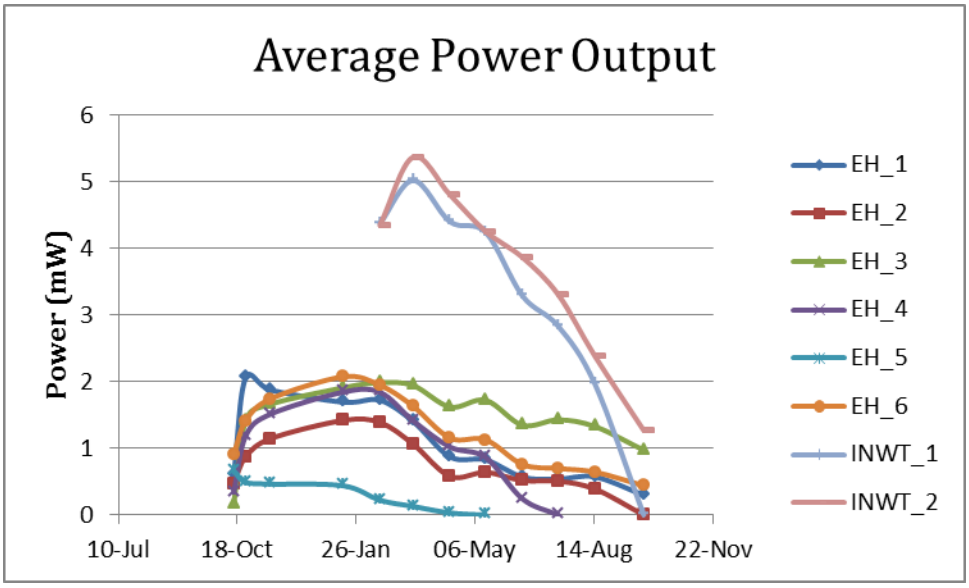

Figure 168. Chart. The trend curves of the maximum average power output analyzed from Oct 15th 2012 to Sep 25th 2013.

There are many reasons would cause the degrading of the energy output generated from each passed vehicle from one energy harvester. The actual reason will be unmasked after removing the installed harvester. Several potential factors and solutions will be discussed in this section. The piezoelectric material is the core part of the energy harvester. Any form of damage of the piezoelectric material will result in the decreasing of power output or even functional failure of the harvester. According to the previous simulation results, using piezoelectric material with circular cross section will mitigate the stress concentration but not eliminate it. Such stress concentration, which is proportional to the impact applied by vehicles, will damage the piezoelectric material with a great external impact. Piezoelectric material with larger cross-sectional area or increasing the quantity of material will reduce the damage brought by stress concentration. Few tests have been conducted to evaluate the long-term fatigue resistance of the energy harvester. It may be another reason which causes the damage on the piezoelectric material. Increasing the cross-sectional area or quantity of the material is also the solution toward this problem. Other than mechanical failure, connection of positive and negative electrodes may cause the functional failure of the harvester. After being passed by millions of vehicles, the protective package may be degraded and allows the influx of surrounding fluid. A sealant with better longevity and mechanical property will be the solution of this problem. A rapidly change of temperature will form the dew inside of the protective package. The dew will cause the short circuit of the positive and negative electrodes or erode the copper electrodes. Filling the protective package with long-term drying agent will prevent the forming of the dew.

8 Data analysis

8.1 Power Generation vs Axle Loading

To better understand the load transmitting efficiency of the energy harvester installed at Troutville weigh station, the electric data collected on October 25th 2013 was analyzed to obtain the corresponding loading condition. The back-calculated loading data is compared to the axle loading data provided by the DMV.

9 sets of axle loading configuration of the vehicles passed Troutville weigh station on Oct 25th 2012 are selected from the traffic data provided by the staff of DMV. Every set of axle loading configuration has one corresponding power output data. For valid comparison, all power output data are from the installed energy harvester #1. Power output data having obvious deviation (the average power is 30% less than the maximum) are not included. The loading configuration and the corresponding electric output data are presented in Table 10. Table 11 shows the time log of the selected loading data.

Table 10. The selected axle loading configuration of the vehicles passed Troutville weigh station on Oct 25th 2013 (kN).

Axle ID	Axle 1	Axle 2	Axle 3	Axle 4	Axle 5	Total	Voltage (Axle5, V)	Power (mW)
1	48.9	80.5	82.3	45.8	45.8	303.4	298.1	2.313
2	47.6	80.5	56.0	42.7	54.7	281.6	312.1	2.451
3	40.9	76.5	78.3	70.7	69.8	336.3	453.9	2.713
4	50.7	60.5	61.8	47.2	40.5	260.7	285.7	2.381
5	53.4	71.2	73.8	75.6	75.6	349.6	459.3	2.738
6	47.2	68.1	66.3	44.9	56.0	282.5	321.2	2.154
7	48.0	63.2	61.8	26.2	36.9	236.2	203.1	2.108
8	50.3	68.9	63.6	74.7	72.1	329.6	433.4	2.921
9	52.5	76.1	72.1	81.8	77.4	359.9	485.8	3.021
10	48.5	77.4	79.6	69.4	67.6	342.5	398.4	2.232

Table 11. The time log of the selected axle loading configuration of the vehicles passed Troutville weigh station on Oct 25th 2013.

AXLE ID	YEAR	MONTH	DAY	HOUR	MINUTE	SECOND

1	12	11	30	15	5	53
2	12	11	30	15	6	32
3	12	11	30	15	16	47
4	12	11	30	15	20	19
5	12	11	30	15	21	56
6	12	11	30	15	27	39
7	12	11	30	15	28	39
8	12	11	30	15	29	54
9	12	11	30	15	31	3
10	12	11	30	15	35	37

Since all the disks are parallelly connected, the voltage on each disk should be the same. The stress applied on each disk can be calculated as:

$$\sigma = \frac{V}{g_{33} \times t}$$

Figure 169.Equation. Stress applied on piezoceramic disks

where the g_{33} is the voltage constant and t is the thickness of the disk. The g_{33} of the 850 PZT used in energy harvester #1 is 0.024 Vm/N and the thickness of the disks is 0.02m. Because the voltage is the maximum one from the data measured from all five axels, the stress on each disk are compared to the axle with the maximum weight. The total loading taken by all 9 disks in one energy harvester can be calculated as:

$$\mathrm{F}_d = \sigma \times \pi r^2 \times 9$$

Figure 170.Equation.Total loading.

Where r is the radius of the disks. The back-calculated total loading of the disks and the corresponding axel loading are listed in the Table 12. From the calculated data, average 14.43% of the axle loading are distributed onto the disks. An axle/voltage ratio is

calculated and the differences of the axle/voltage ratios should be attributed to vehicle wandering.

Table 12. The correlation of the total loading on all disks back-calculated from the measured voltage and the actual loading applied by passing vehicles.

Axle ID	Axle 5 (kN)	Actual loading taken (kN)	Transmission percentage	Voltage (max, V)	Axle/voltage ratio (kN/V)
1	45.8	7.0	15.32%	298.1	0.15
2	54.7	7.3	13.43%	312.1	0.18
3	69.8	10.7	15.31%	453.9	0.15
4	40.5	6.7	16.62%	285.7	0.14
5	75.6	10.8	14.30%	459.3	0.16
6	56.0	7.6	13.50%	321.2	0.17
7	36.9	4.8	12.95%	203.1	0.18
8	72.1	10.2	14.16%	433.4	0.17
9	77.4	11.4	14.78%	485.8	0.16
10	67.6	9.4	13.88%	398.4	0.17
Average	-	-	14.43%	-	0.163

10 Optimization and potential applications.

10.1 Optimization of the Energy Harvester

To further improve the energy harvester, the arrangement and the shape of the piezoceramic material is redesigned. From the electrical performance data measured from the energy harvesters, the voltage output is too high (over 1000 V when connected six of them together) and the current is low. A high output voltage may damage the measuring system and increase the energy wasted by the interfacial circuit. To balance the voltage and current, a three-disk stack of piezoceramic disks will replace the previous one-piece disk. Three 0.3-inch-thick piezoceramic disks with 0.8 inch of diameter will be stacked together. The stacking arrangement is shown in the figure below.

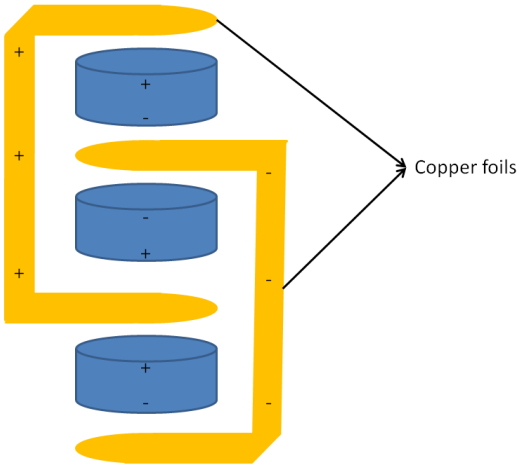

Figure 171. Chart. The arrangement of the new stacking design of piezoceramic disks.

The two ends of copper electrodes will be inserted into the stack to connect three negative and three positive poles. Under this arrangement, more charges will be generated from the piezoceramic disks because it has larger surface area (three surfaces) connected in the circuit. The voltage will be reduced correspondingly. The surface area of single disk is also increased by using a disk with longer diameter. Therefore the internal resistance will decrease due to the increase of the cross-sectional area. Then the current will be increased.

During fabrication, a potential risk is found that the two electrodes are too close to each other. The connection of two electrodes will result in zero power output. To prevent such accident, the inner sides of the electrodes are covered with insulating tape as shown in the following figure.

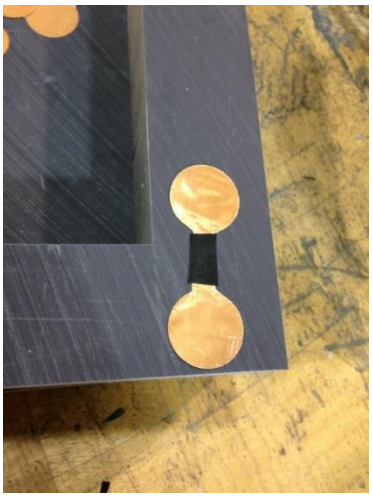

Figure 172. Chart. The electrodes partially covered by the insulating tape

10.1.1 Simples Tests

Two fabricated energy harvesters with different configurations of piezoelectric material have been tested using the Model Mobile Loading Simulator. The test was performed under constant wheel speed and loading to compare the electric performance of the two kinds of energy harvesters. A 1mega-ohm resistor was used as an electric loading. Figure 173 shows the setup of the testing frame containing two energy harvesters.

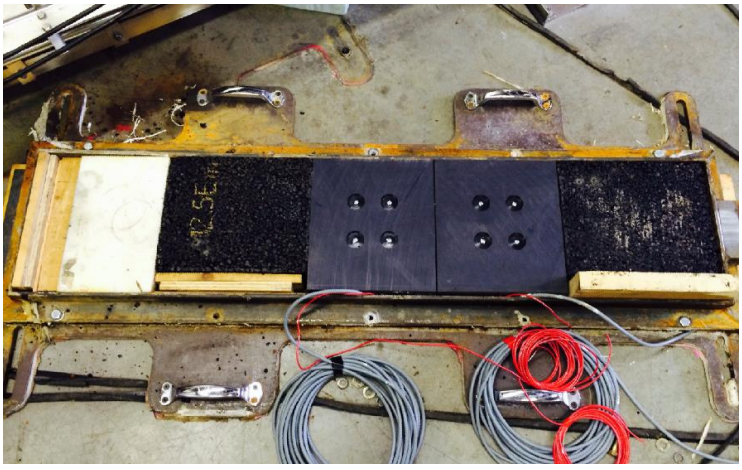

Figure 173. Photo. The setup of the testing frame of MMLS.

Figures 174 and 175 are the voltage waveforms measured from the energy harvesters with regular piezoceramic disks and disk stacks. A total of 30 sets of voltage spectrum were measured on each energy harvester and the one with maximum voltage output are selected for data analysis.

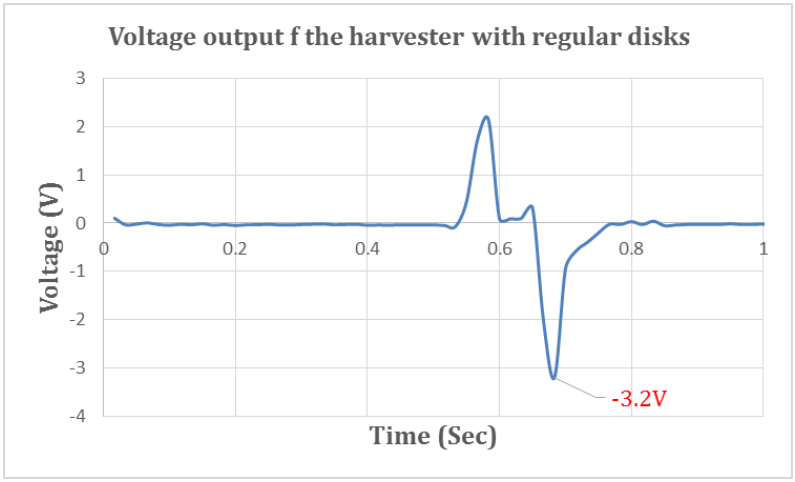

Figure 174. Chart. The power spectrum of the energy harvester containing regular piezoceramic disks measured with 1mega ohm resistor.

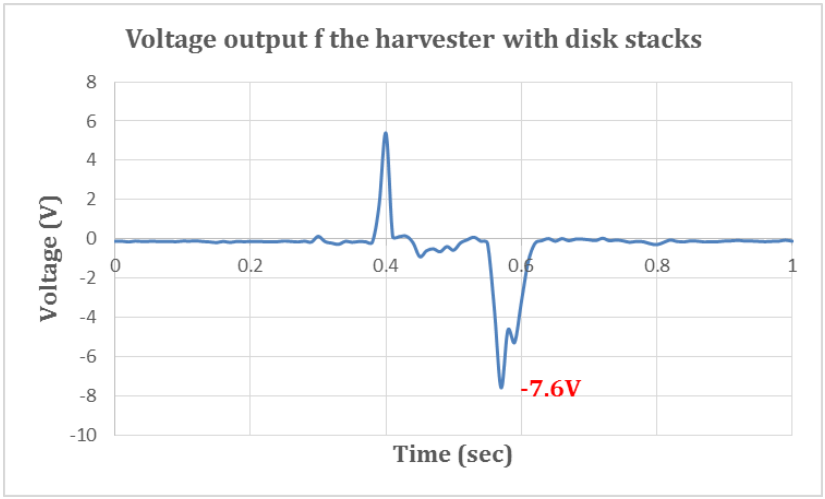

Figure 175. Chart. The power spectrum of the energy harvester containing piezoceramic disk stacks measured with 1mega ohm resistor.

Without rectifying, the output voltage spectrum has positive and negative part. Since the changing rate of stress of the releasing process is higher than the loading process, the negative part has higher absolute value of voltage. The maximum voltage generated by the harvester using regular disks is -3.2V. The maximum voltage generated by the harvester using disk stacks is -7.6V. Since the power on one resistor can be calculated as $P=V^2/R$ and the loading resistor used were the same, the power output of the harvester using disk stacks is about 4 times greater than the one using regular disks.

The overall conclusions from the all the data analysis and the comparison of the performance of harvesters indicate the piezoelectric energy harvesting is predictable using existing theories.

10.1.2 Laboratory Tests of Energy Harvester Using Parallel-Connected Piezoceramic Disks and Rods

Stacks of piezoceramic disks were used in the optimized energy harvester instead of piezoceramic rods. To verify this conclusion, both piezoelectric electric energy harvesters with piezoceramic rods and disks were tested using MMLS with constant wheel speed under same loading condition. Different resistors were used to measure the voltage output from the harvester to calculate the power output. The resistors ranges from 1.5M Ohms to 6M Ohms. The power output of two different types of harvesters are compared and a ratio of the power output was calculated. The testing results are listed in Table 13.

Table 13. The electric performance of energy harvesters using rods and stacks (evaluated by using resistors).

Resistance (Ohms)	Voltage (Rods, V)	Voltage (Stacks, V)	Power (Rods, mW)	Power (Stacks, mW)	Ratio
1500000	3.85	15.7	0.010	0.164	16.6
2000000	5	20.4	0.013	0.208	16.6
2500000	6.2	23.2	0.015	0.215	14.0
3000000	7.1	27.1	0.017	0.245	14.6
3500000	7.9	29.3	0.018	0.245	13.8
4000000	8.6	32.6	0.018	0.266	14.4
5100000	10.1	37.3	0.020	0.273	13.6
5500000	10.5	38.4	0.020	0.268	13.4
6000000	11.2	40.5	0.021	0.273	13.1

From the previous testing results, the average power output of an energy harvester is linearly proportional to its maximum power output. Thus the maximum power output of both energy harvesters were calculated for comparison. It can be concluded that, under the same condition, the power generated from the harvester using piezoceramic disks stacks is about 14 times greater than the one using piezoceramic rods.

10.1.3 Testing Results of Energy Harvesters with Different Configurations of Materials – Charging a Capacitor

To verify the fact that the power output of the optimized energy harvester is greater than the previous one, both energy harvesters were tested under the MMLS to charge a 22uF capacitor. The harvester were tested still with constant load and wheel speed. In every test the capacitor was charged for 5 minutes by the energy harvester and the voltage on the capacitor was measured in every minute. The average power output was calculated by the following equation:

$$\mathrm{P} = E/t = (\frac{1}{2}CV^2)/t$$

Figure 176. Equation. Average power output.

The comparison of the voltage and power output is listed in the following table. The ratio of the average power of both energy harvester was calculated.

Table 14. The electric performance of energy harvesters using rods and stacks (evaluated by charging a capacitor).

Time (min)	Voltage (Rods, V)	Voltage (Stacks, V)	Power (Rods, mW)	Power (Stacks, mW)	Ratio
1	3.24	12.4	0.0019	0.0282	14.6
2	4.45	16.9	0.0018	0.0262	14.4
3	5.74	20.7	0.0020	0.0262	13.0
4	6.69	24.1	0.0021	0.0266	13.0
5	7.32	26.9	0.0020	0.0265	13.5

According to the results, the average power of the energy harvester with piezoceramic disks stacks is about 14 times greater than the one using rods. It is consistent to the previously obtained results.

10.2 Potential Applications

10.2.1 Traffic Signaling

One of the potential application is to utilize the energy harvester as both an energy supply and a trigger of a traffic signal. The traffic signal will be powered by the harvester and will be only functioning when there are vehicles in a certain range. Figure 177 is a conceptual layout of such application.

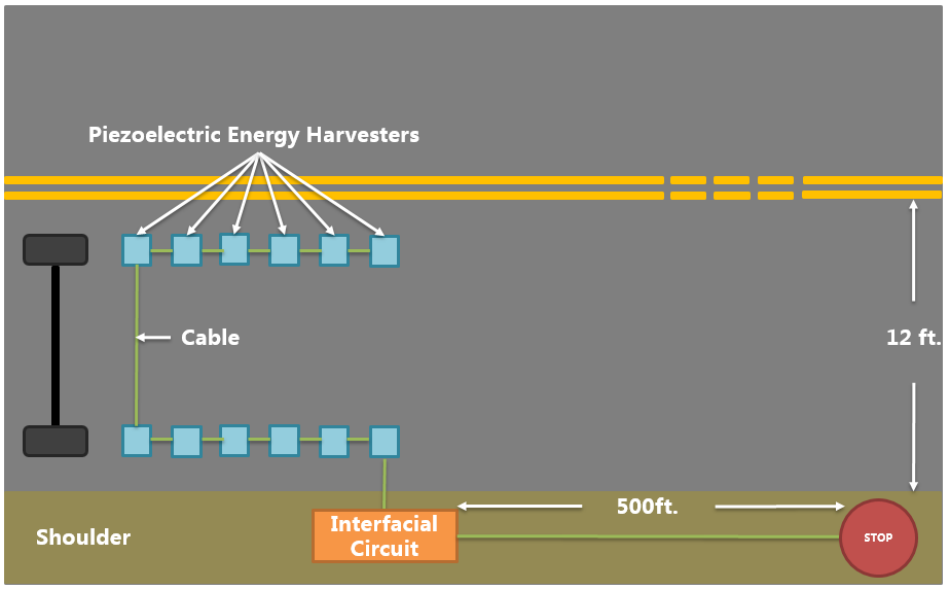

Figure 177. Chart. Conceptual layout of traffic signaling application.

A specially designed controlling circuit is required to provide the function which triggers certain attached electronics and keeps it activated for a certain time duration. For example, in a traffic signal application, the piezoelectric energy harvest will serve as a power supply and also a triggering unit. The power output from one energy harvester will be processed by a signal processing unit to send triggering signal to a switching unit. Once the triggering signal reaches the switching unit, the circuit consisting of the digital signal electronic and its power supply (maybe an energy storage charged by energy harvesters) will be closed. Then, a delaying unit will keep the circuit closed for a desired time duration. As a result, when a vehicle have passed the energy harvester, a digital-displayed stop sign will be activated 1 km ahead of the vehicle for 30 seconds, which is enough for that vehicle to pass it. Figure 178 shows a conceptual sketch of the controlling circuit.

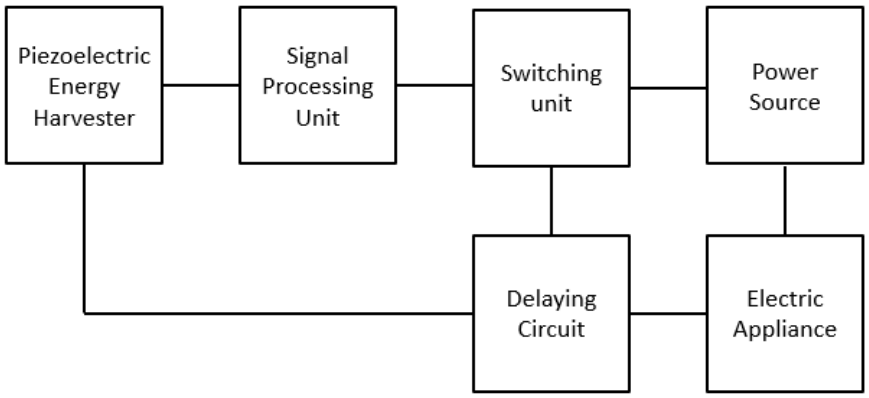

Figure 178. Chart. Conceptual sketch of a controlling circuit for future application

A testing circuit is built with two 1.5V-AA batteries serving as the pre-stored energy source, a 9-V battery served as a reference voltage, a LM-555 microprocessor for comparing the input voltage from the harvester to the reference voltage to filter the generated noise, a microprocessor generating specific signal to trigger the releasing of pre-stored energy source by a triode. The time duration of the releasing time was controlled by a 100k-ohms resistor and different capacitors. A LED bulb was used to test the whole circuit as an electric appliance. Figure 179 is the diagram of the testing circuit.

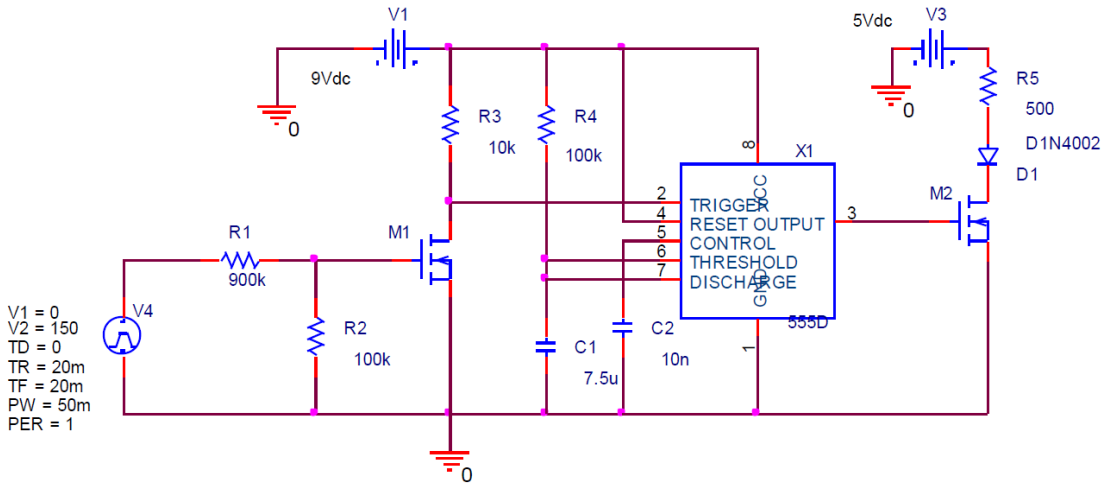

Figure 179. Chart. Circuit diagram of the controlling circuit.

The figure below is the actual circuit built on a testing board connected with the energy harvester.

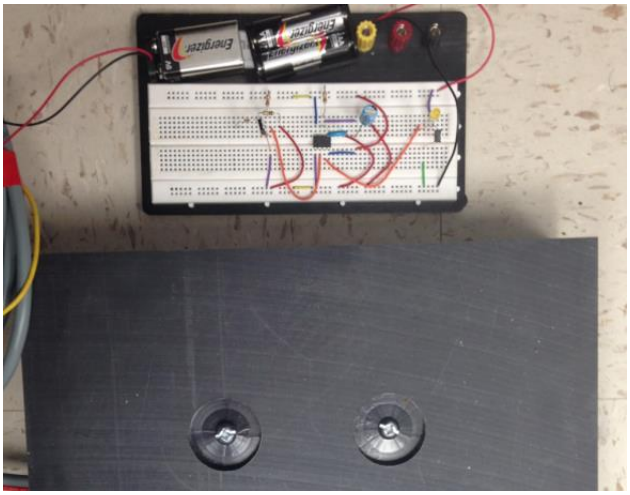

Figure 180. Photo. The actual controlling circuit built on a testing board connected with a piezoelectric energy harvester.

The voltage output generated from energy harvester is about 25 volt by each foot step of an adult. It is certainly higher than the reference voltage (9V) and will trigger the releasing process. The test was performed by stepping on the connected piezoelectric energy harvester and measuring the time duration that the LED bulb was lit. As expected, increasing the capacitance of the capacitor in the r-c combination will increase the releasing time duration. The releasing time durations measured using different capacitor are listed in Table 15.

Table 15. The releasing time duration of the circuit using different capacitors.

Resistor	Capacitor	Releasing Time
100 kΩ	10 µF	1.6 second
100 kΩ	47 µF	6.4 second
100 kΩ	100 µF	11.6 second
100 kΩ	150 µF	17.65 second

The equation to express the relation of the capacitance and the releasing time is:

$$t_R = C \times 10910 + 1.0812$$

Figure 181. Equation. The relation of the capacitance and the releasing time.

The following figure is a photo showing a LED-signal board powered by the energy harvesters installed at Troutville weigh station. The LED board was triggered by the controlling circuit and was activated for 1.5 seconds.

Figure 182. Photo. The LED Traffic signal powered and triggered by the energy harvesters installed at Troutville Weigh Station.

10.2.2 Integrated Energy Harvester

The integrated energy harvester combines photovoltaic and piezoelectric technologies. The solar panels and piezoelectric energy harvesters will be integrated in one block serving as new pavement material. The energy generated from both part will be stored together and managed by the piezoelectric energy harvester. As illustrated in Figure 183,

solar panels are contained in a lattice made from steel. The lattice will distribute the load from the top layer around the solar panels without damaging them. The top layer is transparent to let the sunlight pass through. It also will be strong enough to hold the load from passing vehicles. A fiber-glass base layer will further transmit the load to the piezoelectric generator. The whole piece of the harvester will be weather proof to avoid any environmental interference. Figure 184 is the 3D design of the integrated energy harvester. This integrated harvester consists of the following parts:

- Transparent top layer;
- Solar panels;
- Alloy lattice;
- The piezoelectric energy harvesting unit.

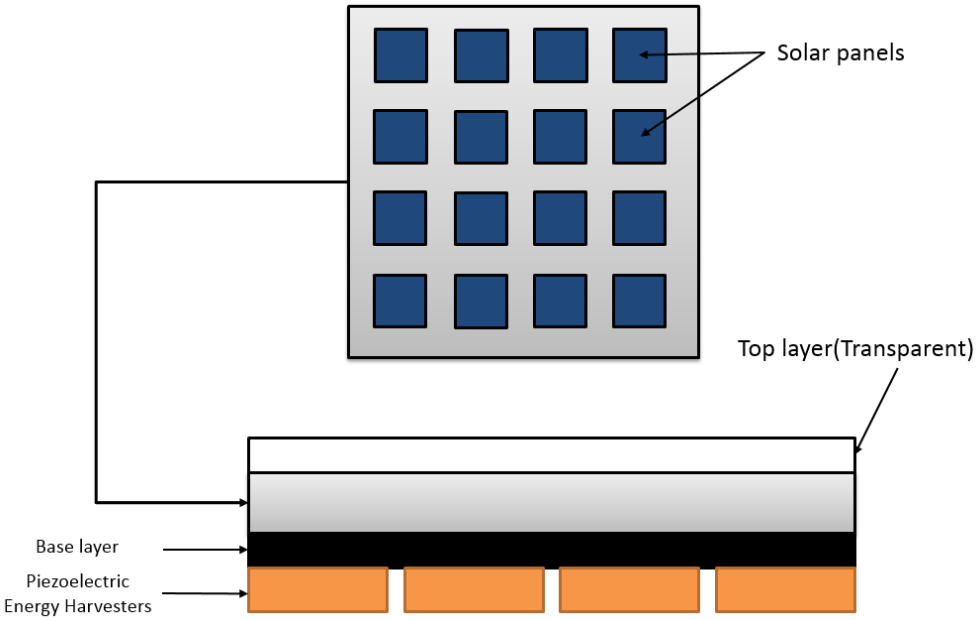

Figure 183. Chart. The conceptual sketch of the integrated energy harvester.

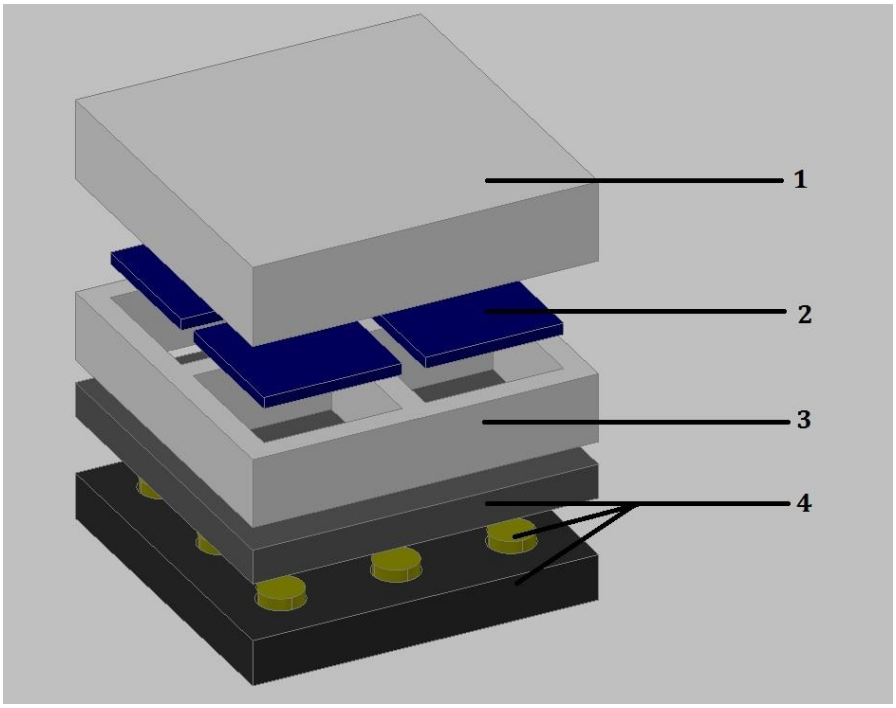

Figure 184. Chart. The 3-D sketch of the integrated energy harvester.

11 Cost-effectiveness analysis

To understand the relation between the cost and the performance of the energy harvester within its life time, an analysis of cost effectiveness is conducted.

From the power output data collected from the energy harvester installed in the weigh station, the maximum energy output of a single piezoelectric energy harvester fabricated by Virginia Tech is 7.45×10^{-7} kWh/vehicle in average. The maximum power output of a single harvester fabricated by Innowattech is 12.61×10^{-7} kWh/vehicle in average (Converted from the power output spectrum). The cost of fabricating one VT's harvester is listed below:

Table 16. The detailed cost of fabricating one optimized piezoelectric energy Table harvester.

Subject	Price (USD)
Piezoceramic disks	261.9
Cover	45
Protective wall	68
Protective board	12
7Base	35
Cable	10
Total	431.9

The cost estimation of fabricating one Innowattech's harvester is about $2000 ($1000 for piezoelectric materials, $1000 estimated for the rest).

Because of the wandering of the vehicles, not every vehicle will hit the harvester and hit it perfectly. It causes the differences on energy output. The hit percentage calculated from the installed energy harvesters is listed below. 17% of the vehicles will perfectly hit the

harvester. 45% of the vehicles will partly hit the harvester and the energy output is from 15% to 85% of the maximum output (perfectly hit).

Table 17. The classified data of vehicle wandering.

IDs of Harvesters	Off (<15%)	Partly on (>15%, <85%)	Perfect on (>85%)	Hit%
1	10	8	2	50%
2	5	7	3	67%
3	13	8	2	43%
4	10	11	5	62%
5	15	5	4	38%
6	3	13	7	87%
All Together	8	22	5	77%
Total	64	74	28	61%

In order to estimate the total energy output of a single harvester, the equivalent hit rate is calculated from the chart above as:

$$\frac{28}{64+74+28} \times 100\% + \frac{74}{64+74+28} \times \left(\frac{15\% + 85\%}{2}\right) \approx 17\% + 22.5\% = 39.5\%$$

Figure 185. Equation. Energy output estimation of a single harvester.

There are 3300 vehicles passing the Troutville weigh station every day from the report provided by VDOT. Assuming the life of the harvester is five years, the energy output estimation for VT's harvester is calculated as shown below. It's about 0.36kWh annually.

$$7.45 \times 10^{-7} kWh \times 3300(vehicles) \times 39.5\% \times 365\ days/yr \times 5yr \approx 1.8kWh$$

Figure 186. Equation. Estimation of annual energy production of VT's energy harvester.

The total energy output of Innowattech's harvester is calculated as shown below. It's about 0.6kWh annually.

$$12.61 \times 10^{-7} kWh \times 3300(vehicles) \times 39.5\% \times 365\ days/yr \times 5yr \approx 3kWh$$

Figure 187. Equation. Estimation of annual energy production of Innowattch's energy harvester.

The cost-effectiveness indicator of VT's harvester is $240/kWh. It's $666/kWh for Innowattech's device.

12 Conclusions and Recommendations

In this project, nine different 33-mode piezoelectric energy harvester have been designed step by step to overcome the encountered obstruction of applying piezoelectric energy harvesting technology into practice. Many piezoelectric energy harvesters were fabricated following the proposed design and evaluated in laboratory and on site. Different interfacial circuits were designed to optimize the electrical output of the piezoelectric energy harvester under different condition. Three installations of energy harvesters were conducted without affecting local traffic and ambient pavement. The harvesters installed at Troutville weigh station have been functioning without maintenance for over one and half year. The average power output of one energy harvester per vehicle is about 3.1 mW. The harvesters fabricated by Virginia tech cost fewer than Innowattech's harvester to

generate same amount of energy. The electrical performance of the harvester was analyzed with the axle loading data of passing vehicle. It's found that the total energy production is highly related to the total axle of the vehicle.

Parallelly connected stack of the disks is recommended for further optimization of the energy harvester. The laboratory testing results indicates that energy harvester with such configuration is more productive under the same condition.

REFERENCES

1. Ashebo, D.B., Tan, C.A., Wang, J., and Li, G. Feasibility of Energy Harvesting for Powering Wireless Sensors in Transportation Infrastructure Applications, *Proceedings of SPIE*, Vol. 6934, 2012.

2. Kim, H. Thickness-Vibration-Mode Multilayer Piezoelectric Transformer or dc-dc Convertor Application, *Journal of Integrated ferroelectrics*, Vol. 107, No. 1, 2009, pp. 12.

3. duToit, N.E., Wardle, B.L. and Kim, S.G. Design Considerations for MEMS-Scale Piezoelectric Mechanical Vibration Energy Harvesters, *Journal of Integrated ferroelectrics*, Vol. 71, No. 1, 2005, pp. 121-160.
4. Voigt, T., Ritter, H. and Schiller, J. Utilizing Solar Power in Wireless Sensor Networks, *Proceedings of the 28th Annual IEEE International Conference on Local Computer Networks*, No. 20-24, 2003, pp. 416-422.

5. Priya, S. and Innam, D., *Energy Harvesting Technologies*, Springer Science, New York, USA, 2005.

6. Lee, C.S., Joo J., Han, S., Lee, J.H. and Koh, S.K. Poly(Vinylidene Fluoride) "Transducers with Highly Conducting poly(3,4-ethylenedioxythiophene) Electrodes, *Proceedings of International Conference on Science and Technology of Synthetic Metals*, Vol. 152, 2005, pp. 49–52.
7. Roundy, S., Wright, P.K. and Rabaey, J.M. A Study of Low Level Vibrations as a Power Source for Wireless Sensor Nodes, *Computer Communications*, Vol. 26, 2003, pp.1131-1144.

8. Jeon, Y.B., Sood, R., Jeong, J.H. and Kim, S. MEMS Power Generator with Transverse Mode Thin Film PZT, *Sensors & Actuators A*, Vol.122, No.1, 2005, pp. 16-22.

9. duToit, N.E., Wardle, B.L. and Kim, S. Design Considerations for MEMS-Scale Piezoelectric Mechanical Vibration Energy Harvesters, *Journal of Integrated Ferroelectrics*, Vol.71, No.1, 2005, pp. 121-160.

10. Twiefel, J., Richter, B., Sattel, T. and Wallaschek, J. Power Output Estimation and Experimental Validation, Journal of Electroceramics, Vol. 20, No. 3-4, 2008, pp. 203-*208.*

11. Inman, D. Engineering Vibration (3rd Edition), 3rd edition, Prentice Hall, Upper Saddle River, 2010.

12. Anton, S. and Sodano, H. A Review of Power Harvesting Using Piezoelectric Materials, *Smart Materials and Structures*, Vol. 16, No.3, 2007, pp. R1-R21.

13. Priya, S. Criterion for Material Selection in Design of Bulk Piezoelectric Energy Harvesters, IEEE Transactions on Ultrasonics, Ferroelectrics, and Frequency Control, Vol. 57, No. 12, 2010, pp. 2610-2612.

14. Erturk, A. Electromechanical Modeling of Piezoelectric Energy Harvesters, Ph.D. thesis, Engineering Science and Mechanics, Virginia Tech, 2009.

15. Richards, C.D., Anderson, M.J., Bahr, D.F. and Richards, R.F. Efficiency of Energy Conversion for Devices Containing a Piezoelectric Component, Journal of Micromechanics and Microengineering, Vol. 14, No. 5, 2004, pp. 717.

16. Twiefel, J., Richter, B., Sattel, T. and Wallaschek, J. Power Output Estimation and Experimental Validation, Journal of Electroceramics, Vol. 20, No. 3-4, 2008, pp. 203-208.

17. Ottman ,G. K., Bhattt, A. C. and Hofmann, H. Adaptive Piezoelectric Energy Harvesting Circuit for Wireless, Remote Power Supply, IEEE Transactions on Power Electronics, Vol. 17, No. 5, 2002, pp. 669–676.

18. Hofmann, H., Ottman, G.K. and Lesieutre, G.A. Optimized Piezoelectric Energy Circuit Using Step-Down Converter in Discontinuous Conduction Mode, IEEE Transactions on Power Electronics, Vol. 18, No. 2, 2002, pp. 696–703.

19. Guyomar, D., Badel, A. and Lefeuvre, E. Toward Energy Harvesting Using Active Materials and Conversion Improvement by Nonlinear Processing. IEEE Transactions on Ultrasonics, Ferroelectrics, and Frequency Control, Vol. 52, No. 4, 2005, pp. 584–595.

20. Badel, A., Benayad, A., Lefeuvre, E., Leburn, L., Richard, C. and Guyomar, D. Single Crystals and Nonlinear Process for Outstanding Vibration-Powered Electrical Generators, IEEE Transactions on Ultrasonics, Ferroelectrics, and Frequency Control, Vol. 53, No. 4, 2006, pp. 673-683.

21. Lefeuvre, E., Sebald, G., Guyomar, D., Lallart, M. and Richard, C. Materials, Structures and Power Interfaces for Efficient Piezoelectric Energy Harvesting, Journal of Electroceramics, Vol. 22, No. 1-3, 2009, pp. 171-179